Università degli Studi di Genova

PhD course in Physics and Nanosciences

XXXIII Cycle

Fabrication and study of thallium based high-temperature superconductors for the beam screen of Future Circular Collider (FCC-hh)

Aisha Saba

Supervisors:

Prof. Marina Putti

Dr. Emilio Bellingeri

Table of contents

Abstract

Research and study on the Future Circle Collider (FCC, 100 km in circumference) have been initiated to create new possibilities for the science world. The conceptual design emphasises achieving centre-of-mass collision energy of 100 TeV by counter-rotating beams. The construction of such a massive accelerator comes with several complications to deal with, and beam stability is one of the essential tasks in an accelerator. It has been theoretically estimated that copper, the current conducting beam screen material, could not offer low surface resistance to cope with the instabilities in the suggested temperature scale (40-60 K) for the beam screen of FCC-hh. Moreover, the beam screen is subjected to a magnetic field of 16 T generated by the magnets that bend the beam. Only a few superconducting materials survive in these conditions.

This thesis discusses the detailed fabrication procedures and measurements carried out on thallium-based high-temperature superconductors to verify the possibility to use this material as screen for the beam.This thesis discusses the detailed fabrication procedures and measurements carried out on thallium-based high-temperature superconductors to verify the possibility to use this material as a screen for the beam.

Bulk superconductors were synthesised and optimised by a planetary ball milling system to obtain the pure and preferential phase Tl-1223 having the highest critical temperature among the thallium superconducting system. For the coatings, rapid and cost-effective electrodeposition technique was used to deposit the highly reactive precursor. The morphology and substrate coverage with superconducting material and grains' formation has improved by depositing precursor coatings at pulsed potential and annealing with unreacted bulk pellet in an oxygen atmosphere. Moreover, safety precautions have always been the priority while working with thallium.

The superconducting grains of bulk and thin-film superconductors were identified using X-ray diffraction (XRD), scanning electron microscopy (SEM), and transmission electron microscopy (TEM) studies. The critical temperature was determined using a four-probe resistivity and scanning superconductivity quantum interference device, and the field profile was mapped using Scanning Hall Probe Microscopy (SHPM) measurements.

For the vacuum analysis, the outgassing rate, the residual gas analysis (RGA), secondary electron yield (SEY), and X-ray Photoelectron Spectroscopy (XPS) measurements. All the obtained results: 5×10^{-8} mbar. l/s per cm^2 outgassing rate after 10 hours, no detection of heavy metals in RGA, and especially least obtained SEY values of 0.77 and 0.97 for amorphous carbon deposited bulk and coatings, respectively, make thallium superconductors acceptable in a vacuum.

In conclusion, the current study on Tl-based superconductors has helped to develop techniques to produce improved superconducting bulk and superconducting thin films. The results obtained from characterisation and vacuum analysis strongly believe in Tl-based superconducting coatings as a potential solution for improving the beam stability in high-energy h-h particle accelerators.

Keywords: FCC-hh, EASITrain, beam screen, high-temperature superconductors, thallium-based superconductors, thin-film coatings, substrates, vacuum compatibility, SEY, XPS.

Chapter 1: Introduction

1.1 Future Circular Collider (FCC)

Human nature is inquisitive, and it seeks to understand the unknown. Physics has aided in the discovery of a path to the unknown and is essential for human evolution. Particle physics assists in the discovery of existence's most fundamental nature. After its first proclamation in 1994, the standard model (SM) was completed on July 4, 2012, when the Higgs boson at mass 125 GeV was discovered at CERN[1]. In reality, the completeness of the standard model is another forward step to progress in science and urges us to pursuit unanswered questions, like dark matter, dark energy, matter-antimatter asymmetry, expansion of the universe, nature and understanding of Higgs boson, source of neutrino masses and the physics beyond with better precision.

Very high-energy collisions and interactions of particles are necessary to answer these concerns. And it will only be achievable with the help of a cutting-edge, high-energy collider [2]. For this, the idea of Future Circular Collider (FCC) was proposed, and a Conceptual design study (EuroCirCol) was initiated for it. For this, the idea of Future Circular Collider (FCC) was proposed, and a Conceptual design study (EuroCirCol) was initiated.

The success and experience of the Large Hadron Collider (LHC) serve as the foundation for FCC's long-term ambition. As a result, one of the most important concerns is that this high-energy machine, built over a long time, should deliver the most possibilities, learnings, and results for the least amount of money.

The FCC-hh is aimed to build about 100 km in circumference, which is three times more than the existing LHC, and will provide 100 TeV centre of mass-energy, about eight times and 10-20 ab^{-1} luminosity with the collision of two counter-rotating proton bunch beams of 50 TeV each [3], [4]. In addition, the FCC will offer proton-ion and ion-ion collisions as well [5].

Moreover, the FCC's research and development (R&D) program opens many doors for educational, technological, and institutional collaboration opportunities worldwide.

Table 1.1 comparison of the FCC-hh's and LHC's parameters [6], [7]

	LHC	FCC-hh
Circumference (km)	27	100
Energy per beam (TeV)	7	50
Current (mA)	580	500
Diapole magnetic field (T)	8	16
Photon flux (ph/ms)	1×10^{17}	1.7×10^{17}

As a powerful and efficient collider, the FCC necessitates research into advanced technologies, high-field magnets, enhanced superconducting materials, and enhanced cryosystems. Moreover, such planned performance necessitates a large magnetic field. Nb_3Sn magnets with a hopeful magnetic field of roughly 16 T (table 1.1) are the best choice compared to NbTi magnets used at

the LHC. Advanced Radiofrequency (RF) equipment, high vacuum, the HTS beam screen, and large-scale cryogenic equipment are also needed to build a massive accelerator[8].

Therefore, global FCC collaboration, hosted by CERN, instigated focused R&D programmes. The project 'European Advanced superconductivity Innovation and Training (EASITrain)' is also embedded in the FCC study along with other projects (see annexe 1).

1.2 Motivation and background to use high-temperature superconductors (HTS) for the beam screen of Future Circular Collider (FCC)

The principal means of accelerating and focusing the beams for collision in an accelerator areareareareare the electrical and magnetic fields generated by acceleration cavities and superconducting magnets[9]. For the safe operation of superconducting devices and to contain heat loads, efficient cryogenic refrigeration is essential. However, it has thermodynamic consequences and can directly impact the system's functioning and cost of operation. Synchrotron radiations, beam image RF currents, photoelectrons impingement, residual gases, or nuclear processes in response to collisions are the most common causes of heat loads. Therefore, a beam screen (BS) is viable for dumping heat loads and shielding superconducting and cooling systems.

The BS offers many benefits [9]. One of the primary goals of inserting BS in magnetic cold bores, for example, is to prevent heat loads from being transferred to low-temperature mass surfaces by absorbing them. It also aids cooling systems in maintaining their cooling efficiency. [10].

If cold mass working temperature is T_{cm}, the operating temperature of BS is T_{bs} must be chosen to minimise the total exergy loss, and it is denoted by ΔE [9],

$$\Delta E = Q_{cm}\left(\frac{T}{T_{cm}} - 1\right) + (Q_{bs} - Q_{cm})\left(\frac{T}{T_{bs}} - 1\right) \quad 1.1$$

Where T is room temperature, Qcm is the heat reaching the cold mass, and Q_{bs} is the heat falling onto the BS.

Several parameters influence the velocity of particle bunches (beams) in an accelerator, including particle energy, magnetic fields, angular frequency, and accelerator size. Moving charged beams produce several instabilities in their surroundings because they stimulate electromagnetic (EM) waves. The image currents induced by circulating charged beams on an accelerator's beam screen result in joule heating. One of the most critical requirements in an accelerator is to reduce power dissipation due to the Joule effect. In an accelerator of radius R, and vacuum chamber of radius b, the power loss can be calculated by the longitudinal coupling impedance [11];

$$Z_L = \frac{2\pi R}{2\pi b} Z_s(\Omega) \quad 1.2$$

Z_S is the impedance of the vacuum chamber material.

And the power loss,

$$P_{loss} = NI_B^2 Rr(Z_{loss}) \quad 1.3$$

Where N is the number of particle bunches, I_B is the bunch current, and Z_{loss} is the longitudinal impedance.

The oscillations of the beam can also be affected by wake-fields generated by the beam itself, leading to transversal instabilities. The transverse (Z_T) coupling impedance is [11],

$$Z_T = \frac{2\pi Rc}{\pi b^3 \omega} Z_s(\Omega m^{-1}) \quad 1.4$$

Where c is the speed of light, and ω is the frequency of wakefield. Then, it can be seen that it is inversely proportional to the pipe radius (b) to the power of three.

It can be seen from Equations A and B that both, Z_L and Z_T, depend on the surface impedance Z_s. That means a low resistive material is needed to suppress the joule heating and transverse coupling impedance [12]. A beam screen having low resistance is required to avoid the consequences of dissipation. A BS made of copper, a good conductor, at 20 K is an already used solution to absorb the radiations and shield the magnets in the LHC.

To sum up, a beam screen was introduced to reduce heat load and beam instabilities while being vacuum friendly [9]. High vacuum and beam stability are considered vital ingredients to maximise the collision and detection of outcomes. Both beam stability and high vacuum depend on several factors discussed in this chapter and the fourth chapter.

Figure 1.1. The beam screen of the Large Hadron Collider (LHC) is coated with copper

In FCC-hh, two 8 cm long beams containing 10^{11} protons will be steered in the opposite direction by the magnetic field. These beams will emit around 28 /W/m/beam synchrotron radiations and 4.8 MW power in the entire accelerator upon collision. Magnets cannot absorb this release of power at 1.9 K. It is estimated that to extract 1 W at 1.9 K, it takes 9×10^2 W of electricity and hence around 4.32 GW is required to extract 4.8 MW [13]. Indeed, the operation of a BS at 50 K would help absorb the radiations and reduce the power consumption [14]. Nevertheless, the surface resistance of copper coating (fig. 1.1)at 50 K might not offer beam stability.

To avoid all of these instabilities, a low-surface-resistance material facing the beam is required. A copper BS might not be enough with the lowest frequency line of 2 kHz for FCC[15], a copper BS might not be enough; another material, preferably HTS, is required.

As mentioned in the previous section, many systems need to be updated and advanced for an enormous FCC project. Moreover, one of the major tasks is to upgrade the design [16] and, more importantly, the beam screen material.

So, taking the FCC requirements under consideration, it was accepted to explore high-temperature superconductors (HTS) as beam screen coatings for the FCC [17](Table 1.2 shows a comparison between FCC-hh and LHC beam screen). The primary choice of material depends on its impedance, superconducting properties and vacuum compatibility. And then its production feasibility to a large scale for an accelerator.

Table 1.22. comparison of the FCC-hh's and LHC's beam screen parameters [18]

	LHC	FCC-hh
Beam current (A)	0.584	0.5
Superconducting magnet	NbTi	Nb_3Sn
Diapole coil aperture (cm)	56	40
BS diameter (cm)	4.6	3
BS temperature (K)	20	40-60
SR heat load (W/m/aperture)	0.17	28.8

1.3 The formulation for Surface resistance of superconductors in the presence of dc magnetic field

For the reasonable stipulations of BS, HTS must be improved and explored for radio frequency (RF) field, surface resistance (RS), and superconducting properties.

Many questions arise when choosing superconducting materials to utilise as BS. In terms of frequency, magnetic field, and temperature, find the most compatible superconducting system. As previously stated, BS carries image current, while HTS is a new subject in terms of image current when subjected to a strong magnetic field. When a superconductor operates in a dc magnetic field, the motion of trapped fluxons gets affected by the image currents, which directly affect its surface resistance, and similar work is present in literature [19]–[21]. An Attempt is made to understand the effect of trapped fluxons on the surface resistance of superconductors in the presence of a dc magnetic field [22].

The RF current J_{Rf} in a superconductor in the presence of a magnetic field is given by [23].

$$\overrightarrow{J_{rf}} = (\sigma_1 - i\sigma_2)\left(\overrightarrow{E_{rf}} - \vec{V} \times \overrightarrow{B_0}\right) \quad 1.5$$

where σ_1 and σ_2 are the real and imaginary parts of the conductivity, $\overrightarrow{E_{rf}}$is the electric field, $B_O = n\phi_o$ is the external field, and $\vec{v}$ is the fluxon velocity. Assuming $\overrightarrow{B_0}$ is perpendicular to $\overrightarrow{J_{rf}}$ and the fluxon oscillations motion equation,

$$m\ddot{x} + \eta\dot{x} + kx = J_{rf}\varphi_o \quad 1.6$$

The fluxon displacement x $\left(\dot{x} = V = V_0 e^{i\omega^t}\right)$ and is valid for small displacement, mass m, η viscosity and kx pinning force, and $J_{rf} = J_{rfo}e^{i\omega t}$

The fluxon mass is neglected $(m \approx 0)$ equation becomes

$$\left(\eta V_o e^{i\omega t} + k\frac{V_o e^{i\omega t}}{i\omega}\right)\varphi_o = J_{rfo}\varphi_o e^{i\omega t}$$

$$\eta\left(1 - i\frac{k}{\eta\omega}\right) = J_{rfo}\varphi_o$$

$$V_o = J_{rfo}\,\varphi_o/\eta\left(\frac{\eta\omega - ik}{\eta\omega}\right)^{-1}$$

Solving and taking $\omega_o = \frac{k}{\eta}$ (depinning frequency), solving the above equation,

$$V_0 = \frac{J_{rfo}}{\eta}\varphi_o\left(\frac{\omega^2}{\omega^2 + \omega_o^2} + i\frac{\omega\omega_o}{\omega + \omega_o^2}\right)$$

As

$$\omega_0(B_O) = 2\pi\nu_0(B_o)$$

Or

$$\nu_0(B_0) = \frac{1}{2\pi}\frac{k(B_0)}{\eta}$$

As the average pinning force,

$$k = \frac{2\pi}{d}\frac{\alpha_c \varphi_0}{B_0}$$

Where α_c is maximum Lorentz force limit for the flux tube lattice. Putting k in the equation

$$v_o(B_o) = \frac{\rho_n \sqrt{B_o} J_c(B_o)}{\sqrt{\varphi_o} B_{c2}} \qquad 1.7$$

where $J(B_0) = \frac{\alpha_C(B_0)}{B_0}$

$$\rho_{eff} = \frac{\overrightarrow{E_r}}{\overrightarrow{J_{rf}}} = \frac{1}{\sigma_1 - i\sigma_2} + \frac{\vec{v} \times \overrightarrow{B_0}}{\overrightarrow{J_{rf}}}$$

$$\rho_{eff} = \frac{1}{\sigma_1 - i\sigma_2} + \rho_n \frac{B_O}{B_{c2}}\left(\frac{\omega^2}{\omega^2 + \omega_o^2} + i\frac{\omega\omega_o}{\omega^2 + \omega_o^2}\right) \qquad 1.8$$

Where the first part of the equation is the standard complex superconductor resistivity and is denoted by ρ_s and the second part is resistivity in flux flow regime and denoted by ρ_f,

$$\rho_s = \frac{1}{\sigma_1 - i\sigma_2}$$

$$\rho_f = \rho_n \frac{B_O}{B_{c2}}\left(\frac{\omega^2}{\omega^2+\omega_o^2} + i\frac{\omega\omega_o}{\omega^2+\omega_o^2}\right) \text{; or } \rho_f = \rho_n \frac{B_O}{B_{c2}}\left(\alpha(\omega) + i\beta(\omega)\right)$$

The surface impedance,

$$z_{sf} = (1+i)\sqrt{\frac{\mu_{o\omega}}{2}\left(\frac{\sigma_1}{\sigma_2^2} + i\frac{1}{\sigma_2} + \rho_n \frac{B_O}{B_{c2}}\left(\alpha(\omega) + i\beta(\omega)\right)\right)} \qquad 1.9$$

$$z_{sf} = (1+i)R_n\sqrt{(a+ib)}$$

With

$$R_n = \sqrt{\frac{\mu_{o\omega}}{2}\rho_n}$$

$$a = \frac{\frac{\sigma_1}{\sigma_2}}{\left(\frac{\sigma_2}{\sigma_n}\right)} + \frac{B_O}{B_{c2}}\alpha(\omega), \textbf{ and } b = \frac{1}{\left(\frac{\sigma_2}{\sigma_n}\right)} + \frac{B_O}{B_{c2}}\beta(\omega) \qquad 1.10$$

The real and imaginary parts of surface impedance are,

$$R_{SF} = R_n\sqrt{\sqrt{a^2+b^2}-b} \qquad 1.11$$

$$I_{SF} = R_n\sqrt{\sqrt{a^2+b^2}+b} \qquad 1.12$$

Case A: High-Frequency limit (ω >> ω$_o$)

From equation 1.11,

α(ω) ≈ 1 and β(ω)≈ 0

so,

$$a = \frac{\sigma_1/\sigma_n}{(\sigma_2/\sigma_n)^2} + \frac{Bo}{B_{C2}} \textbf{ ; and } b = \frac{1}{\sigma_2/\sigma n} = \frac{2\lambda^2}{\delta_n^2}$$

I. Low fields

$$\frac{B_O}{B_{C2}} \ll \frac{1}{\frac{\sigma_2}{\sigma_n}}$$

Binomial expansion of $R_{SF} = R_n\sqrt{\sqrt{a^2+b^2}-b}$

$R_{SF} = R_n\sqrt{b + a^2/2\,b^2 - b}$

So,

$$R_{SF} = R_n \frac{a}{\sqrt{2b}} \qquad 1.13$$

And putting values of a and b in equation 13

$$R_{SF} = \frac{R_n}{\sqrt{2}}\left[\frac{\sigma_{\,1}/\sigma_n}{(\sigma_{\,2}/\sigma_n)^{3/2}} + \frac{Bo}{B_{C2}}(\sigma_{\,2}/\sigma_n)^{1/2}\right]$$

$$R_{SF} = \frac{R_n}{\sqrt{2}}\left[\frac{\sigma_{\,1}/\sigma_n}{(\sigma_{\,2}/\sigma_n)^{3/2}}\right] + \frac{R_n}{2}\left[\frac{Bo}{B_{C2}}\frac{\delta_n}{\lambda}\right] \qquad 1.14$$

The first part of the equation represents the standard surface SR of a superconductor, while the second part is SR due to oscillating fluxons in low fields.

II. High field

Taking

$$\frac{B_o}{B_{c2}} = \frac{\sigma_1/\sigma_n}{\frac{\sigma_2}{\sigma_n}^2}$$

So, a and b become,

$$a = \frac{B_o}{B_{c2}}; b = \frac{1}{\frac{\sigma_2}{\sigma_n}}$$

However, for the high-frequency regime b<<1 and high field a >> b, we can neglect b in equation A.

$$R_{SF} = R_n\sqrt{a}$$

$$R_{SF} = R_n\sqrt{\frac{B_o}{B_{C2}}} \qquad 1.15$$

Case B: Low-Frequency limit (ω << ω₀)

$\alpha(\omega) \cong \frac{\omega^2}{\omega_0^2}$and $\beta(\omega) \cong \frac{\omega}{\omega_0}$

$$a = \frac{\sigma_1/\sigma_n}{(\sigma_2/\sigma_n)^2} + \frac{Bo}{B_{C2}}\frac{\omega^2}{\omega_o^2} \quad ;$$

$$b = \frac{1}{\sigma_2/\sigma n} + \frac{B_o}{B_{c2}}\frac{\omega^2}{\omega_o^2}$$

I. Low fields

So, $\frac{B_o}{B_{c2}}\frac{\omega^2}{\omega_o^2} \ll \frac{1}{\sigma_2/\sigma_n}$ leads to a<<b, so equation 1.11 becomes

$$R_{SF} = R_n \frac{a}{\sqrt{2b}}$$

And inserting a and b in the above equation,

$$R_{SF} = \frac{R_n}{\sqrt{2}}\left[\frac{\sigma_1/\sigma_n}{(\sigma_2/\sigma_n)^{3/2}} + \frac{Bo}{B_{C2}}(\sigma_2/\sigma_n)^{1/2}\frac{\omega^2}{\omega_O^2}\right]$$

The first term represents the standard surface resistance of a superconductor in low frequency and field regimes, and the second term

$$R_{SF} = \frac{R_n}{\sqrt{2}}\left[\frac{Bo}{B_{C2}}(\sigma_2/\sigma_n)^{1/2}\frac{\omega^2}{\omega_O^2}\right]$$

It can be written as

$$R_F = \frac{R_n}{2}\left[\frac{Bo}{B_{C2}}\frac{\delta_n}{\lambda}\frac{\omega^2}{\omega_O^2}\right]$$

Or

$$R_F = \frac{\rho_n}{2\lambda}\left[\frac{Bo}{B_{C2}}\frac{\omega^2}{\omega_O^2}\right] \qquad 1.16$$

II. High fields

$$a \approx \frac{Bo}{B_{C2}}\frac{\omega^2}{\omega_o^2}$$

$$b \approx \frac{B_o}{B_{c2}}\frac{\omega}{\omega^2}$$

And for a<<b

$$R_{SF} = R_n \frac{a}{\sqrt{2b}}$$

$$R_{SF} = R_n \sqrt{\frac{B_o}{2B_{c2}}} \left(\frac{\omega}{\omega_o}\right)^{3/2} \qquad 1.17$$

And for the imaginary part

$$I_{SF} = R_n \sqrt{\sqrt{a^2 + b^2} + b}$$

a<<b

$$I_{SF} = R_n \sqrt{\sqrt{b^2} + b}$$

$$I_{SF} = R_n \sqrt{b + b} \qquad I_{SF} = R_n \sqrt{2b}$$

$$I_F = \sqrt{2} R_n \left(\frac{B_o}{B_{c2}} \frac{\omega}{\omega_o}\right)^{1/2} \qquad 1.18$$

These equations help estimate the surface impedance of the superconductors in different frequency and magnetic field regimes. Moreover, temperature-independent SR somehow guarantee the thermal stability of HTS[22].

1.4 Selection of high-temperature superconductors (HTS) for testing the operative criterion of beam screen

The BS of about 3 cm in diameter [24]should be coated with the HTS layer of thickness around 1 µm. The beam bunches will induce a 25 A peak current in the coating. So, it is stated that the critical current density J_c coated HTS should be around 2.5×10^4 Acm^{-2} at 50 K and 16T for a safe operation.

Hence, based on the FCC's conditions and evaluations, the required HTS should be coated on a conductive tubular metal surface should have [17]:

1. Upper critical field larger than 70 T at 50 K.
2. The critical current density J_c should be around 2.5×10^4 A cm^{-2} at 50 K and 16T.

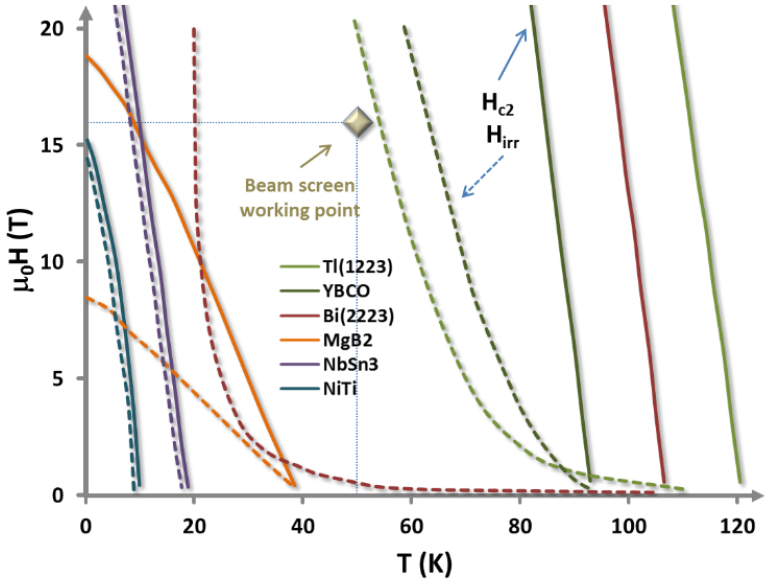

Figure 1.2. Estimation of Irreversibility lines of high-temperature superconductors close to the beam screen working point (T=60 K and 16 T)

Unfortunately, at this time, no HTS material has such outstanding performance. There are mainly three HTS: RE—Ba—Cu—O, Bi—(Ca, Sr)—Cu—O, and Tl—Ca—Sr—Cu—O superconductors. However, all of these cuprate families come with some drawbacks. Although YBCO-123 superconductors have a high upper critical field and critical current density, even minor grain misalignment can cause significant Jc deterioration, making deposition in the inner surface of a tube-like shape complex [25].BSCCO cuprate, instead of having high T_C and the ability to be deposited on the surface of the substrate, have high anisotropy. Thallium based superconductors, specifically Tl-1223, have a high critical temperature (120 K). Two chosen candidates are:

1. Thallium based high-temperature superconducting coatings
2. Commercially available YBCO tapes

The research on Industrially developed YBCO tapes, competitors to Tl-1223, is investigating replacing copper. The surface resistances and depinning frequencies of $REBa_2Cu_3O_x$ in different magnetic fields and temperature regime is evaluated using the rigid fluxon model mentioned in the previous section [26]. Since REBCO coated conductors are already industrially available, FCC vacuum requirements are also calculated[27]–[29].

However, high-temperature YBCO superconducting tapes need to solder on the metal structure, and this could induce a high transversal thermal causing instability[30]However, high-temperature YBCO superconducting tapes need to solder on the metal structure, and this could induce a high transversal thermal causing instability[30]However, high-temperature YBCO superconducting tapes need to solder on the metal structure, and this could induce a high transversal thermal causing instability[30]However, high-temperature YBCO superconducting tapes need to solder on

the metal structure, and this could induce a high transversal thermal causing instability[30]However, high-temperature YBCO superconducting tapes need to solder on the metal structure, which could induce a high transversal thermal causing instability[30]. In addition, the reduction of J_c due to minor grain misalignment limits its deposition on cylindrical configurations.

On the other hand, Thallium-based high-temperature superconductors offer many advantages, i.e. deposition on curved surfaces, high T_c, and high reversibility line. Comparatively, low anisotropy holds a high probability to be deposited as BS coatings[13]. It has been reported in the literature [31] reported that thallium J_c can reach ~ 10^5 A cm^{-2} at77 K.

Because of their qualities, capacities, and benefits, thallium-based superconducting cuprates have been the subject of intensive research in the field of superconductivity since their discovery in 1988[32]–[34]. However, due to toxicity concerns, there is a 15-year hiatus in the hunt for thallium-based superconductors. In 2017 [13], the possibility of resuming research on thallium-based superconductors to investigate their potential for the BS of FCC was discussed and decided. Unlike YBCO, thallium-based superconductors are studied from the ground up, starting with manufacture, enhancement, and finally characterisation.

Tl-1223 thin-film precursor coatings can be deposited using various processes, including electrodeposition pulsed laser deposition, spray pyrolysis, liquid gas solidification, the sol-gel method, and spin coating. Furthermore, in the thallous atmosphere, the treatment of post-deposited precursors needs to be improved. Furthermore, thallium-based superconductors can easily be doped [35]–[37] with other elements, which can help to increase superconductivity properties.

The following chapters are merely devoted to fabricating and examining Tl-1223 temperature thallium-based superconductors for the BS of the FCC.

1.5 Introduction to thallium based high-temperature superconductors

With their Nobel Prize-winning discovery of superconductivity at 30 K in $(La, Ba)_2CuO_4$, Bednorz and Muller directed new research of HTS superconductivity in 1986 [38]. Following this work, HTS cuprates $YBa_2Cu_3O_7$ (Y-123)[39], Tl-Ba-Cu -O [40], Bi-(Ca, Sr)-Cu-O [41], and eventually Tl-Ca-Ba-Cu -O were discovered.

This family turned out to be so promising that researchers began to study thoroughly despite being based on thallium, a highly toxic element. Several groups worked on these cuprates [42]–[44], discovering the existence of two series collectively represented by the formula $Tl_mBa_2Ca_{n-1}Cu_nO_{2+m+2n}$ (or the abbreviation m:2:n-1:n), where m refers to TlO layers separated by n-1 (when n>1) calcium layers (separation layers), and n refers to the adjacent CuO_2 layers (conducting layers). The layer sequence of these materials is $-(TlO)_m-(BaO)-(CuO_2)-Ca-(CuO_2)-\ldots-Ca-(CuO_2)-(BaO)-(TlO)_m-$. Between the TlO layers of a series of these cuprates, there is the existence of two-

dimensional CuO_2 layers. An octahedral CuO_6 block exists for the n=1 compound, two pyramidal CuO_5 blocks exist in the n=2 compound, and two pyramidal and one square CuO_2 blocks exist.

The single-layer (m=1) thallium cuprates are one-of-a-kind. In contrast, the double-layer (m=2) cuprates are structurally similar to bismuth cuprates, with thallium (Tl) replacing bismuth (Bi) and barium (Ba) replacing strontium (Sr). Tl-cuprates have a more symmetrical structure, while a lack of structural modulation is found in Bi cuprates [45].

Thallium-based compounds are hole carriers, so-called p-type superconductors. Typically, holes are placed into the octahedral and pyramidal CuO_2 layers, which appear to contribute to superconductivity.

$Tl_2Ba_2Ca_2Cu_3O_{10}$, a thallium member with m=2 and n=3, has the highest T_c of 125 K[46]. $Tl_2Ba_2CuO_6$ (m=2 and n=1) is the most perplexing cuprate, with Tc ranging from 0 to 90 K [47].

To make novel superconductors, many researchers were inducing many changes in $Tl_mBa_2Ca_{n-1}Cu_nO_{2+m+2n}$ by substitutions to improve the structural stability, T_C, Production of pure phase, and hole doping to enhance the superconducting properties. However, some of them turned out to be non-superconducting. Moreover, it said entirely dependent on substitutions and synthesis methods. Substitutions are usually done for the reasons given below:

- Thallium, lead, bismuth, and chromium are anticipated to increase copper oxide planes' overall concentration.
- Substituting strontium for barium reduces the cell, reducing the D distance between two consecutive CuO_5 or CuO_6 blocks and facilitating charge transfer.
- When multiple rare earths partially occupy this Cu2+ site, the latter is more efficient.

In double layers ($Tl_2Ba_2Ca_1Cu_2O_8$), importantly, strontium can be substituted for Ba, although the T_c is low (44 K) [48]. However, Sr substitution is feasible in single Tl layers, but this series can only be stabilised by partially replacing Tl with Pb ($Tl_{0.5}Pb_{0.5}$ $Sr_2Ca_{n-1}Cu_nO_{3+2n}$ (n=1,2, 3). For n=3, the cuprate formulation $Tl_{0.5}$ $Pb_{0.5}$ $Sr_2Ca_2Cu_3O_9$ (Tl-1223) has a critical temperature (T_c) of 122 K [[49]. T_c are 95 and 120 K, respectively, for the cuprates (Tl, Bi) $Sr_2Ca_2Cu_3O_9$ (Tl-1223) and (Tl, Bi) $Sr_2Ca_2Cu_3O_9$ (Tl-1212) with Bi in Sr replaced [50], [51].

$TlBa_2CuO_5$ [TBCO-1201] and $TlSr_2CuO_5$ [TSCO-1201] are generally non-superconducting for the members m=1 and n=1 unless the appropriate oxygen stoichiometry is used [52].

1.5.1 The importance of Tl-1223 and Tl-1212 phases

As described in the previous paragraph, among the other thallium phases Tl-1223 phase is the first choice in search of FCC-hh beam screen material due to numerous reasons to warrant special attention to this phase: a critical temperature as high as 130 K and irreversibility line comparable to Y-123, and endless substitution possibilities to improve pinning centres.

The preparation of pure Tl-1223 bulk samples with other minor phases is described in detail in this section. However, the preparation of thin films with pure Tl-1223 is difficult without the presence of other phases such as Tl-1212, Tl-1201, CuO, and $BaCuO_2$ (discussed in chapter 3). Thus, making Tl-1212 more of interest along with the Tl-1223 phase. Moreover, only Tl-1212 (m=1,n=2) and Tl-1223 (m=1,n=3) exhibit refined structures in the single-layer series $TlBa_2Ca_{n-1}Cu_nO_{3+2n}$[53], [54]. These compounds' unit cells are tetragonal and belong to the P4/mmm group. The single-layered TlO is flat, and there is no body-centred symmetry.

The single-layered $TlBa_2CaCu_2O_7$ (Tl-1212) is substantially comparable to the reference superconductor Y-123 for transportation measurements. Tl-1212 can also be examined for various substitutions to improve the T_C and its pinning properties. The crystal structure and data for Tl-1212 are present in fig. 4 and table 1.3, respectively.

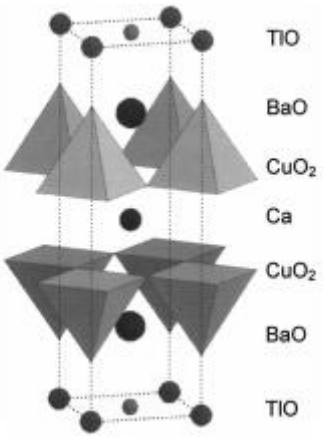

Figure 1.4. Crystal structure of Tl-1212

Table 1.3. Crystallographic data of $Tl_{1.13}Ba_2Ca_{0.87}Cu_2O_7$ (a=3.8472, and c=12.721 Å) [55]

Atom	Site	X	Y	Z
Tl	4(l)	0.0877	0	0
Ba	2(h)	0.5	0.5	0.2155
Cu	2(g)	0	0	0.374
Ca	1(d)	0.5	0.5	0.5
O(1)	1(c)	0.5	0.5	0
O(2)	2(g)	0	0	0.1582
O(3)	4(i)	0	0.5	0.3797

Parkin et al. [44] first identified $TlBa_2Ca_2Cu_3O$ (Tl-1223 with T_c=110 K) with crystal structure belonging to the P4/mmm group having a=3.8429 Å and c=15.871 Å. The crystal structure of Tl-

1223 (Fig. 1.5, and site data in table 1.4) contains two pyramidal blocks of CuO_5 and one square block of CuO_4.

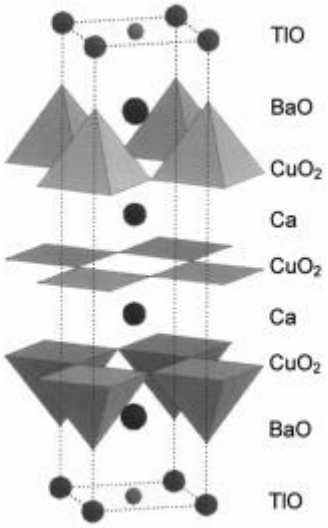

Figure 1.5. Crystal structure of Tl-1223

Table 1.4. Crystallographic data $Tl_{0.56}Pb_{0.56}Sr_2Ca_{1.88}Cu_3O_9$ (with a=3.808, and c=15.232 Å) [53]

Atom	Site	X	Y	z
Tl	4(l)	0.067	0	0
Sr	2(h)	0.5	0.5	0.1709
Cu(1)	2(g)	0	0	0.2868
Ca	1(h)	0.5	0.5	0.3928
Cu(2)	1(b)	0	0	0.5
O(1)	4(n)	0.4	0.5	0
O(2) O(3) O(4)	2(g) 4(i) 2(e)	0 0 0	0 0.5 0.5	0.1582 0.3797 0.5

It has been demonstrated that in the Tl-1223 phase, more effective pinning exists due to a thinner insulating layer, analogous to the case of single-layer YBCO [56]. Figure 1.6 shows irreversibility lines for some of the most available high-temperature superconductors. This graph shows two particular superconductors at an exceptional concentration at liquid nitrogen temperatures (77 K) in various magnetic fields: Y-123 and Tl-1223 superconductors. In the case of fully oxygenated Y-123, finding a manufacturing procedure capable of producing long continuous wires and tapes free of inter-grain weak links and capable of transporting high currents in magnetic fields is extremely difficult.

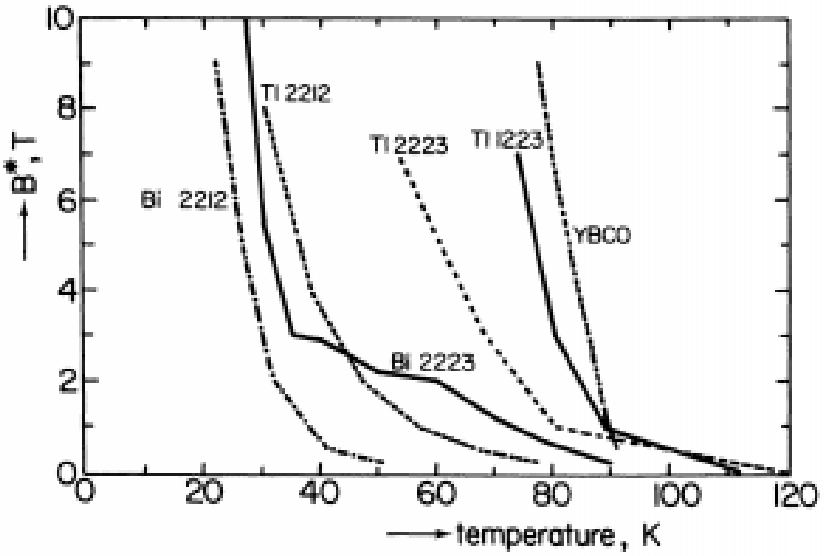

Figure 1.6. The irreversibility lines of various high-temperature superconductors in the magnetic field.

Single-layer Tl-1223 and double layer Tl-2223, particularly near Y-123, have much higher irreversibility lines than double atomic blocking layer compounds Bi-2212, Bi-2223, and Tl-2212. The Tl-1223's promising flux pinning characterisation is due to increased C-axis coupling between superconducting copper oxide layers [17]. As a result, thallium material development is of interest in high-current magnetic field applications.

Although the exact cause of pinning centres in the material is unknown, it is suspected that defects such as vacancies, dislocations, stacking faults, or impurity particles, in addition to the increased axis coupling between the superconducting copper oxide planes [57], may play a role [58].

Various types of structural substitution have been gradually applied to stabilise the 1223 phase and optimise the weak links and pinning property properties of the two basic compounds, the best known of which are those with Tl sites partially replaced by Pb or Bi or both, and the Sr site substituted by Ba [58], [59].

High strontium (Sr) amounts are commonly used because Ba must form the substituted Tl-1223 phases [48]. Moreover, it has been discovered that samples with high Sr concentration affect material's microstructure, resulting in a reduction in the insulator layer's thickness, which leads to an increase in Josephson coupling between adjacent CuO_2 layers and a shift in the irreversibility line towards higher temperatures [60]. The reduction of the Cu-O spacing in the (a,b) plane, and therefore the crystal grows in this direction, is a significant secondary action of Sr on the barium sites. Liu et al [61], [62] fabricated vacuum annealed substituted Tl-1223, $(Tl_{0.5}Pb_{0.5})$ $(Sr_{1.6}Ba_{0.4})$ $Ca_2Cu_3O_9$ (Tl-1223), with the T_c of 130 k and transport current J_c= 1.24×10^5 $A.cm^{-2}$ at 77 K and 1 T field.

Considering all the advantages of substitutions, this research concentrated on synthesising (Tl, Pb, Bi)-1223 with a T_c of roughly 120 K to take advantage of the elements' substitution.

1.5.2 Thallium oxides

Among four thallium oxides-Tl_2O, TlO_2, Tl_2O_3, Tl_4O_3 [63], and some compounds, $Tl_2O_3.Tl_2O$ and 3 $Tl_2O.Tl_2O_3$ Tl_2O_3 has usually been used for the synthesis and thallination of the process. Tl_2O_3 has a rare earth oxide structure, and Tl(III) lies on an octahedral coordinate, and this oxide transforms into the corundum structure under high pressure [63]. These two structures exist in black and show low resistivity (10^{-3} to $10^{-4}\Omega$ cm) at room temperature.

Also, a range of melting points has been noted for these compounds. For example, the melting point of Tl_2O_3 has been noted at 717 to 725 ˚C[64], 750-775 ˚C [16,17][65], or at 834 ˚C[66] whereas Tl_2O said to melt comparatively low temperatures around 300 C [10] or 579 ˚C[63]. These variances have been ascribed to liquid-solid thallium oxide solutions with multiple valences of thallium cations [67], and the liquidus temperature varies with oxygen partial pressure. For frequently used Tl_2O_3, the melting point in air is 717-725 ˚C[64], in flowing oxygen is greater than 750˚C[65], and > 1 atm oxygen is 825˚C [64]. However, Tl_2O_3 is unstable at high temperatures and decomposes to Tl_2O,

$$Tl_2O_3(s) \rightarrow Tl_2O(g) + O_2(g)$$

So, the decomposition of Tl_2O_3 results in the high pressure of Tl_2O, while synthesising the thallium-based superconductors in oxygen flow results in a significant amount of thallium loss. Several researchers have noticed that by annealing a mixture of oxides (e.g., BaO_2, CaO, and CuO), including Tl_2O_3 in an open system, it lacks an excessive source of Tl_2O and superconducting phase forms simultaneously with thallium volatilisation. It was noticed [68], [69] that the long heat treatment (>150 minutes) of starting Tl-2223 composition resulted in the formation of single layer composition. Moreover, the 1223 and 1212 compositions' annealing for 2 hours resulted in non-superconducting phases: $BaCuO_2$, CaO, and CuO.

So, the superconducting phases improve by reducing the reaction time and reacting Tl_2O_3 with already reacted Ba-Ca-Cu-O[70]–[72].

`

Chapter 2: Fabrication and preliminary characterisation of thallium based bulk superconductors

2.1 Synthesis of $Tl_{0.7}Bi_{0.2}Pb_{0.2}Sr_{1.6}Ba_{0.}4Ca_{1.9}Cu_3O_{9+x}$ (Tl, Pb, Bi-1223) superconducting phase

The fabrication techniques and characterisations of thallium-based bulk material are detailed in this chapter. Despite the need for coatings for the BS, the preparation of sintered and non-sintered bulk material fabrication started concurrently with thin-film coating for two main motives:

- Preliminary characterisations of Tl-1223 pellets to understand the potential of this phase for FCC-hh's BS requirements and optimise elements' substitution and doping.
- Use as a thallination source for the deposited precursors in the final annealing (Fig.2.1).

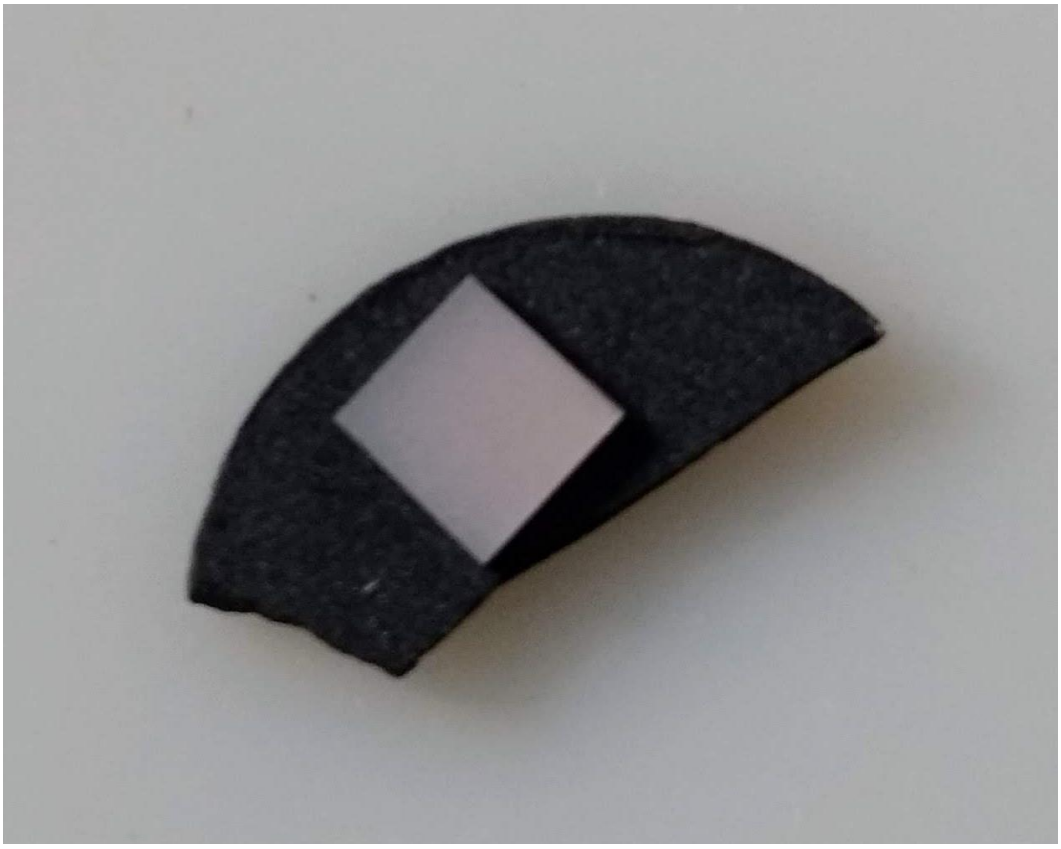

Figure 2.1. A thin film precursor deposited on $SrTiO_3$ (5×5 mm) placed upside down on a piece of already developed Tl-1223 pellet

The synthesis of the samples is done by a two-step solid reaction. Compared to the one-step method (mixing all required materials at once), the two-step method has many advantages, compositional homogeneity, reduction of powder melting. Above all, the addition of thallium oxide in the final step helps minimise thallium loss.

To achieve $Tl_{0.7}Bi_{0.2}Pb_{0.2}Sr_{1.6}Ba_{0.}4Ca_{1.9}Cu_3O_{9+x}$ (Tl, Pb, Bi-1223) phase, the synthesis started by using carbonates of Barium ($BaCO_3$), Strontium ($SrCO_3$), Calcium ($CaCO_3$), and Copper oxide (CuO) with the necessary stoichiometric ratio. The carbonates of elements are used since they have superior chemical stability, and their decomposition is slow even above 900 ˚C.

These carbonates were mixed and grounded using mortar and pestle for three hours, then mixed powder material was calcinated using a quartz boat in the furnace at 900°C for 24 hours in 1 bar of oxygen. After 24 hours, the furnace was cooled to room temperature, and the powder was again slightly grounded using a quartz mortar pestle and then treated at 980 °C in the air for 24-hours in the form of pellets. Once precursor pellets were chilled to room temperature after heating (fig.2.2)

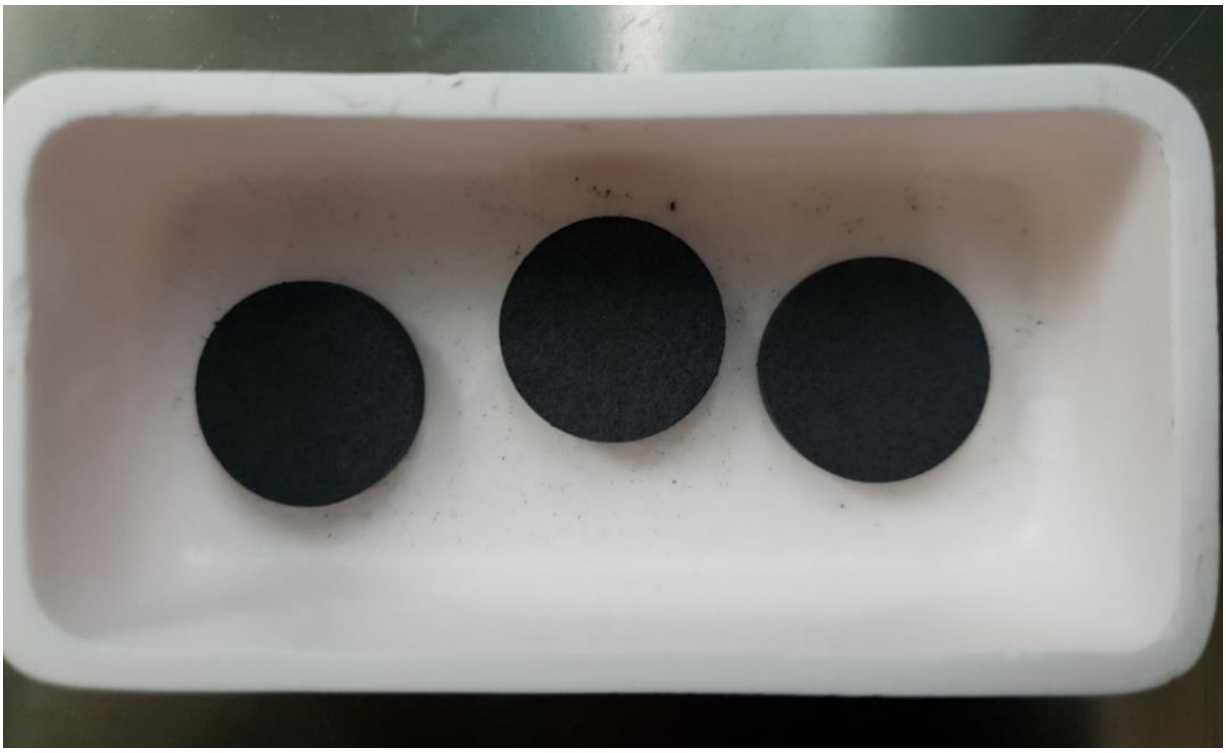

Figure 2.2. The calculated amount of Ca, Ba, Cu and Sr carbonates after two calcinations in oxygen and air in pellets' form

Then, PbO and Bi_2O_3 (fig.2.3 a,b) in the twice calcinated precursor and grounded further for three hours in mortar to mix properly. And finally, black Tl_2O_3 powder mixed with Agate mortar was added under very safe settings.

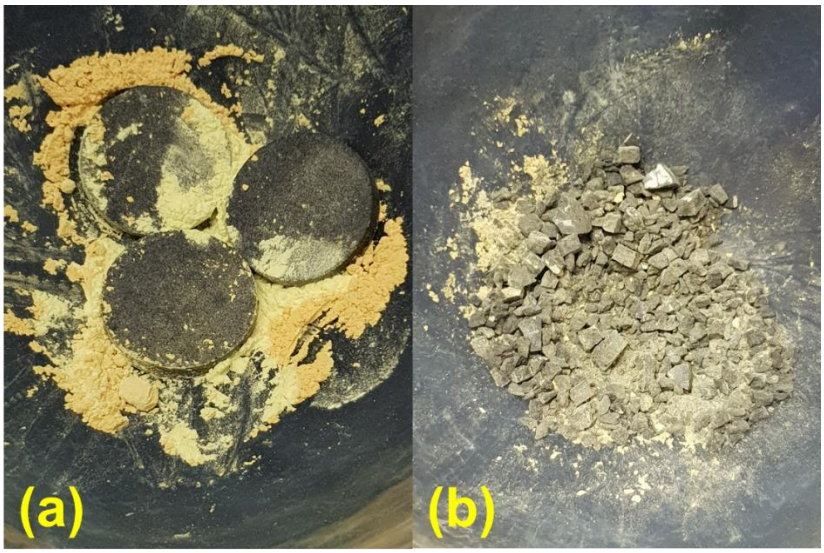

Figure 2.3. The addition and of BiO and PbO (a) in the twice calcinated pellets and manual mixing (b) them all together before mixing in pulveriser

Finally, the well-mixed powered was Pelletised with a hydraulic press into a 2 cm diameter and 2 mm thickness pellet by applying 200 bars for 10 minutes. And for final treatment, the pellet was enclosed airtight in the homemade gold capsule (fig. 2.4) to retain the volatile thallium (around 717 ˚C) and annealed at 905 °C for 3 hours in an oxygen flux to form stable Tl, Pb, Bi-1223 bulk superconductors (fig. 2.5).

Figure 2.4. A homemade packet capsule made of pure gold for the final annealing of thallium - 1223 to retain thallium.

Figure 2.5. The final treated Tl, PB, Bi-1223 bulk superconductor of 2 cm diameter

2.2 Preliminary characterisation results of Tl, Pb, Bi-1223 Bulk samples

A series of Tl, Pb, Bi-1223 pellets were prepared with a slightly different method to further increase the superconducting phase by decreasing the impurities. This chapter includes the characterisation done on three samples: Primary bulk sample, improved bulk sample, and Milled-powder bulk sample. These bulk samples are prepared with slightly different grinding techniques to enhance the superconducting phase by improving the homogeneity of the powder. The following characterisations primarily characterised post-annealing samples: X-Ray Diffraction (XRD), SEM, Electrical resistivity measurements.

2.2.1 X-Ray Diffraction (XRD)

X-ray diffraction (XRD) is a technique to recognise the crystal structure of the materials and provide information about the unit cell. The basic principle of XRD is irradiation of incident energetic X-rays (with small wavelengths around 0.01 to 10 nm) to the arranged crystals of materials that produce a regular array of scattered waves. These scattered waves interact to interfere destructively or constructively. This constructive interference leads to measuring the intensities and scattering angles of the X-rays that diffract from the material**.** Hence interferences happen, and by Bragg's law

$$2dsin\theta = n\lambda$$

where n is an integer, d is the space between two diffraction planes, θ is the incident angle, and λ is the wavelength of the incident beam. The size of atoms of the material should be comparable to the wavelength of X-rays for the diffraction pattern. It is not possible to make a good diffraction grating that can satisfy the conditions of X-rays diffraction. So, the spacing between regularly

arranged lattice atoms of crystal is almost equalled to the order of the wavelength of X-rays. As the crystal has a natural grating, which can be used for diffraction.

Polycrystalline samples Tl-1223 prepared by, mentioned in section 2.2, solid-state reaction. Almost pure Tl-1223 XRD pattern (fig. 2.6) was obtained using a PANALYTICAL X'PERT PRO diffractometer with Cu-$K_{\alpha 1}$ radiation of wavelength 1.540598 Å. Only a few impurities were found (peaks indicated by stars).

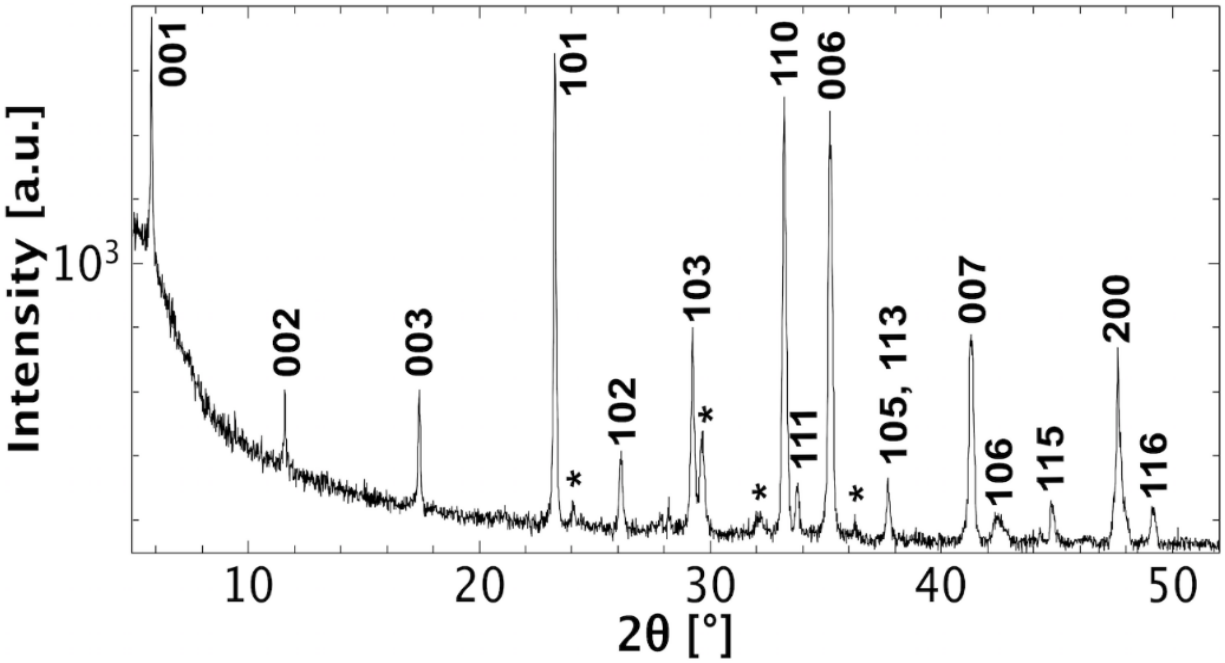

Figure 2.6. X-ray diffraction data of a precursor-pellet and indicated miller indices of pure Tl-1223 phase had been labelled at the peak positions, and the signs'*' indicates impurity peaks.

2.2.2 Scanning Electron Microscopy (SEM)

The most extensively utilised analytical technique is scanning electron microscopy (SEM). This research performed SEM measurements with a microscope Leica Cambridge S 360 equipped with an energy dispersive spectrometry (EDS) silicon drift detector Oxford X-Max 20. Moreover, the software used was Oxford aZtec. SEM has been used to observe the morphology, superconducting phases, presence and identification of non-stoichiometric impurities, and size of grains.

Scanning Electron Microscopy (SEM) has been employed to several Tl, Pb, Bi-1223 bulk samples to investigate the morphology, stoichiometry, non-stoichiometric impurities and grains. This section covers SEM analysis of the pellets named: bulk sample, improved bulk sample, and milled powder bulk sample.

Primary bulk sample

SEM is performed on one of the primary bulk samples (fig.2.7) prepared by the solid-state reaction method (mentioned in section 2.1). Table 2.1 shows the atomic per cent of elements is 1223 with a little more copper (a slight variation is expected from the surface of a bulk).

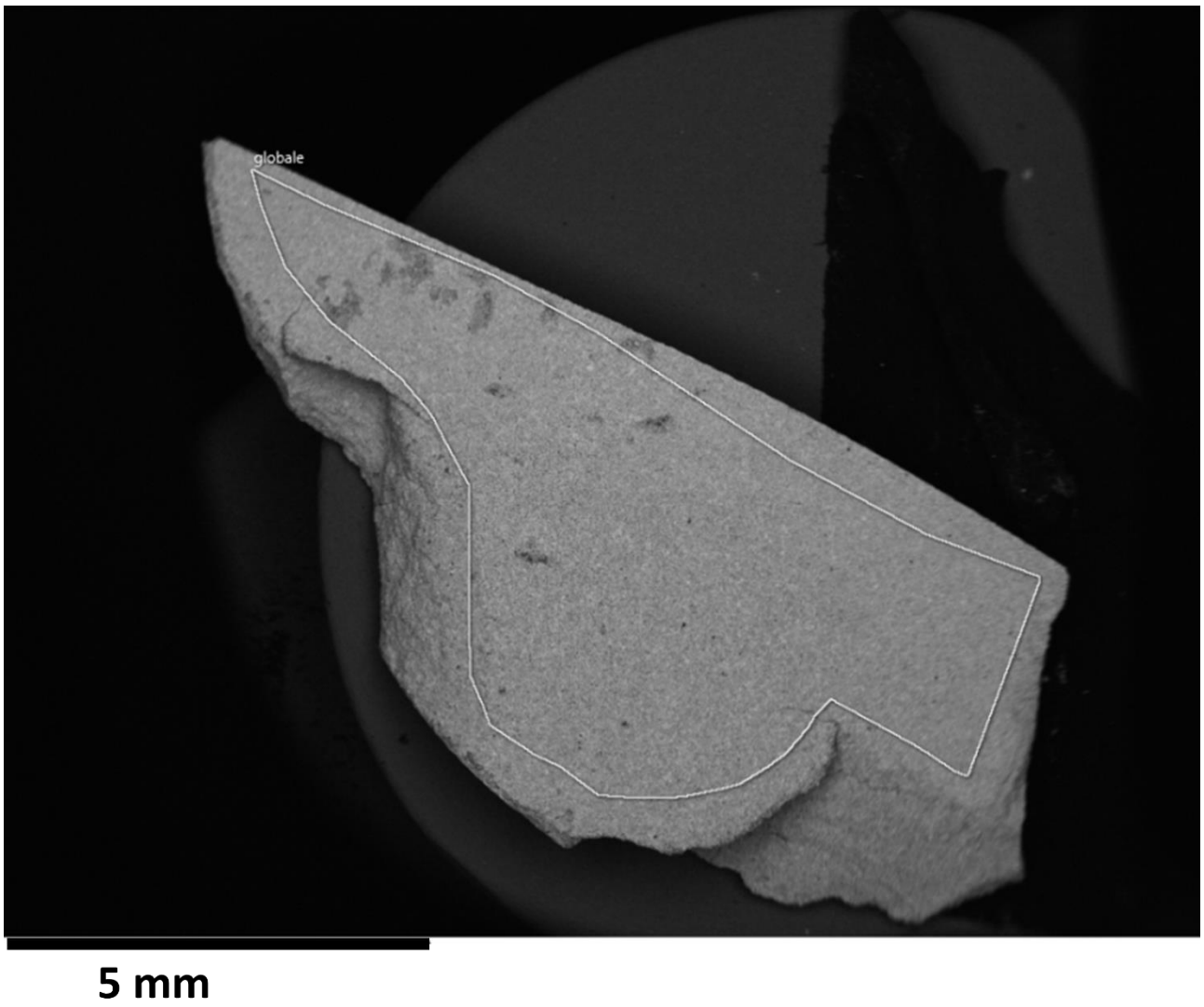

Figure 2.7. An SEM image of a piece of Tl, Pb, Si-1223 superconductor

Table 2.1. The atomic per cent of the elements of the bulk sample (fig. 13)

Element	Tl	Pb	Bi	Sr	Ba	Ca	Cu	O	Total
Global atomic %	3.35	1.33	1.02	8.48	2.48	10.61	21.34	51.39	100

The deep investigation of the bulk sample in figure 2.8 with the Scanning Electron Microscope clearly shows the formation of Tl, Pb, Bi-1223 grains and table 2.2 records the average atomic percentage of the two spectra (indicated as 264 and 266). In contrast, the other spectrum (265) indicates the CuO impurity.

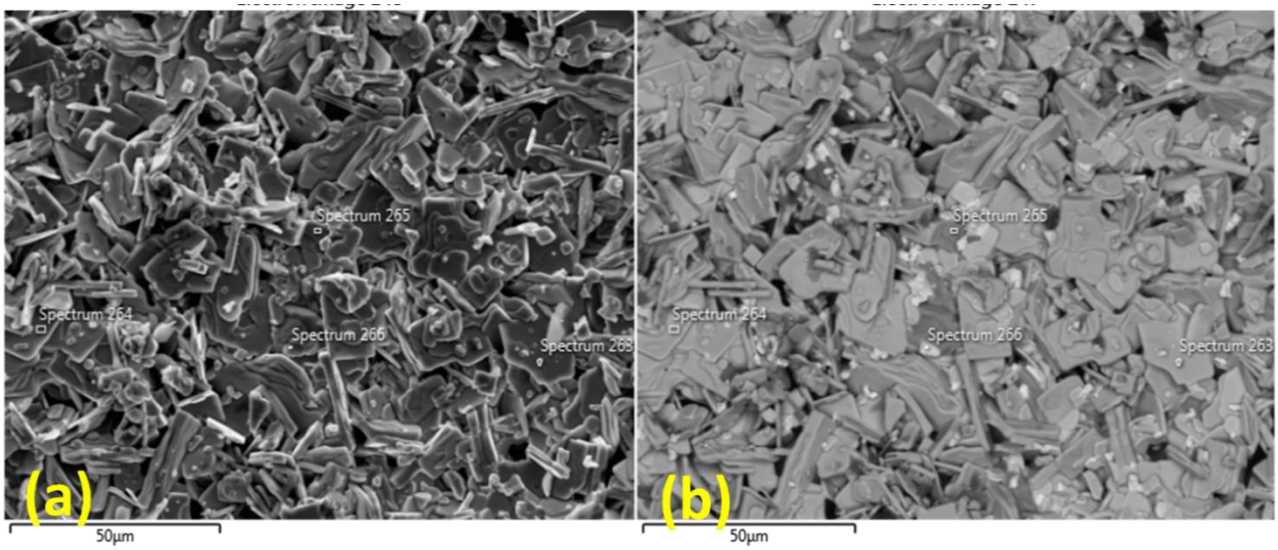

Figure 2.8. Secondary (a) and backscattered (b) Sem images of the pellet showing the formation of pure Tl-1223 phase(grey) with some non-stoichiometric oxides

Table 2.2. The average atomic per cent of the spectrum of the elements of the bulk sample (fig. 14)

Element	Tl	Pb	Bi	Sr	Ba	Ca	Cu	O	Total
average atomic %	4.37	1.36	1.09	10.1	2.90	12.695	22.28	45.195	100

Improved bulk sample

Even though the primary bulk sample shows slab like grains, it contains many CuO and Bismuth oxide impurities. So, the formulation of the bulk sample was optimised by increasing the mixing and grounding time of the precursor powders to decrease the impurities. Fig. 2.9 (corresponding

table 2.3) shows the SEM micrograph of the bulk sample, and it can be seen in the image the formation of big compact Tl, Pb, Bi-1223 grains.

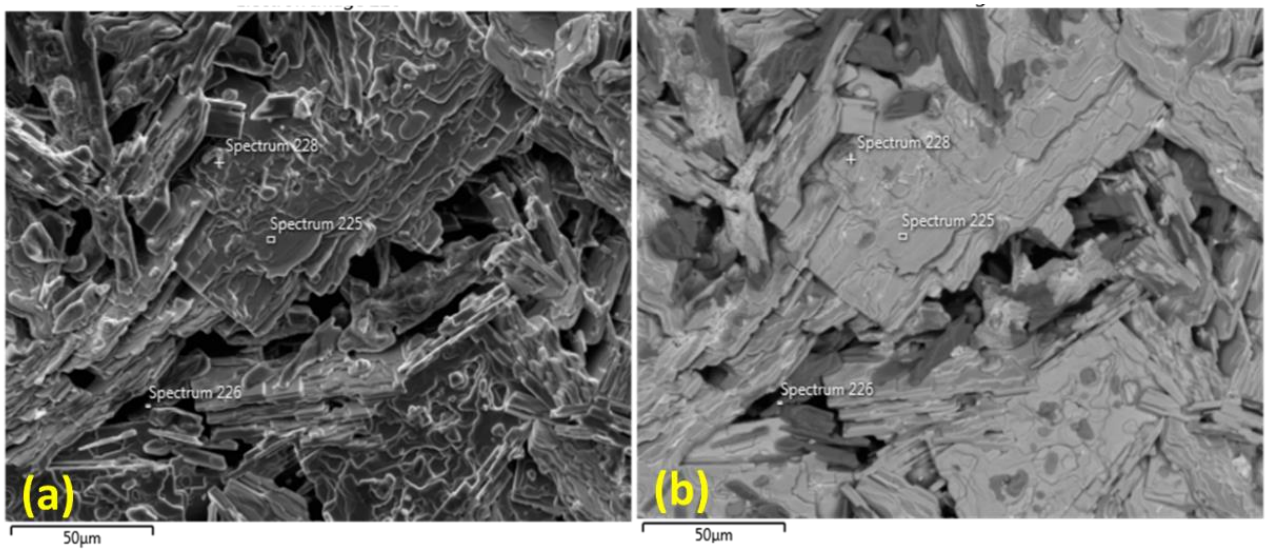

Figure 2.9. The SEM (a) secondary and (backscattered) micrographs of the improved sample. The sample has really big and dense grains of Tl, Pb, Bi-1223. The presence of some CuO impurities (dark grey) can be noticed

Table 2.3. The average element atomic percentage calculated from the spectra (fig. 2.9)

Element	Tl	Pb	Bi	Sr	Ba	Ca	Cu	O	Total
Average atomic %	2.25	1.70	2.68	6.385	2.48	10.325	13.06	59.705	100

After confirming the formation of the good phase of the bulk sample with SEM images, the resistance behaviour (fig.2.10) of the Tl, Pb, Bi-1223 sample was measured in 0-9 Tesla magnetic fields Quantum Design PPMS. The critical temperature T_c of the specimen is 118 K in the self-field. And the temperature is more than 80 K in 9 T.

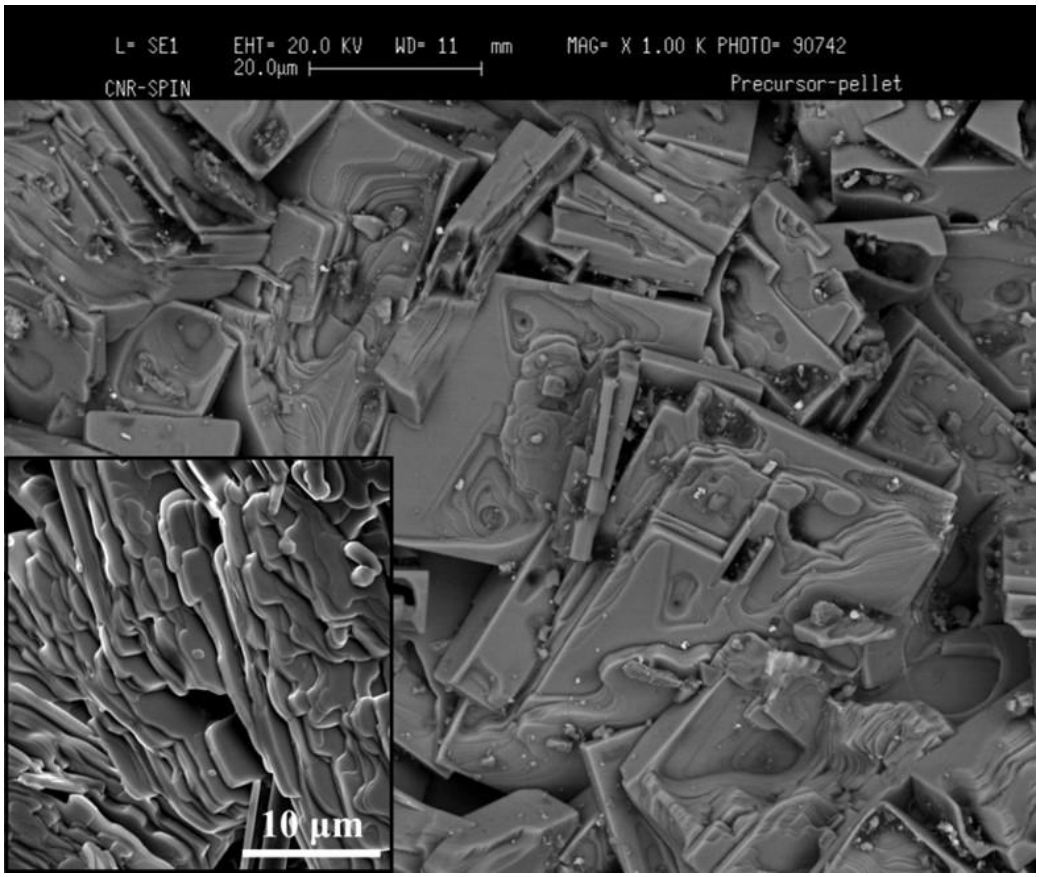

Figure 2.10. In the main image, the backscattered measurement shows homogeneity of 1223 grain in grey colour

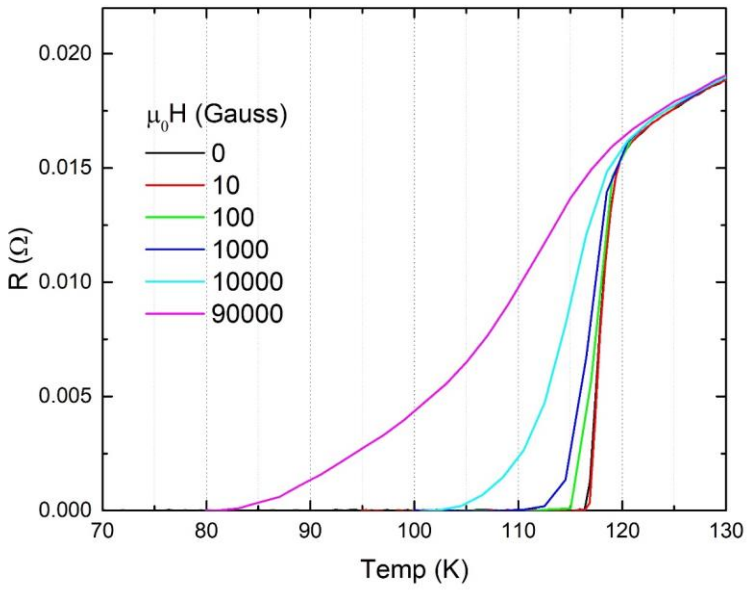

Figure 2.11. Resistance Vs temperature measurement performed on the sample at different applied magnetic fields

The shift of the zero-state caused by the applied field estimates the irreversibility and the upper critical fields, H_{irr} and H_{c2}, (fig. 2.11) adopting the 10% R_N and 90% R_N method, where R_N is the normal state resistance.

The extrapolation shows (fig 2.12) a very high H_{c2} and, more importantly, a very high H_{irr}. An estimation of the H_{irr} dependence for higher fields is inserted as a dashed line reaching up to 20 T around 70K confirming the suitability of the Tl-1223 phase for the FCC-hh environment.

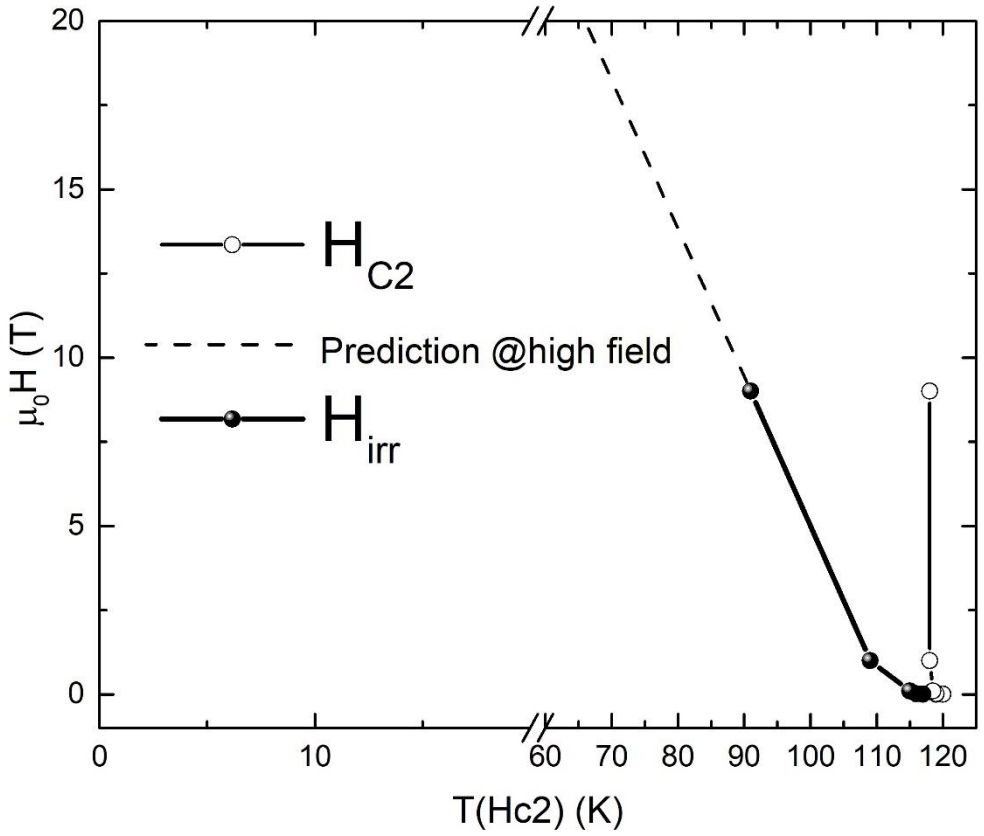

Figure 2.12. Extrapolation from the graph in figure 18 of the upper critical (rings) and irreversibility (dots) magnetic field and the extended dashed line is a prediction at high field

Bulk sample Milled powder

The synthesis of milled powder is a little bit different from other pellets. After two calcinations, PbO and Bi_2O_3 were added to the precursor powder and then subjected to 60 hours of planetary ball milling pulverisette in Argon after being pulverised in the air. And x-ray diffraction (fig. 14) was performed after different hours of milling, and it is clear that amorphisation increase with time. One of the most noticeable effects in the SEM image (fig.2.14) is the cleanness of the grains.

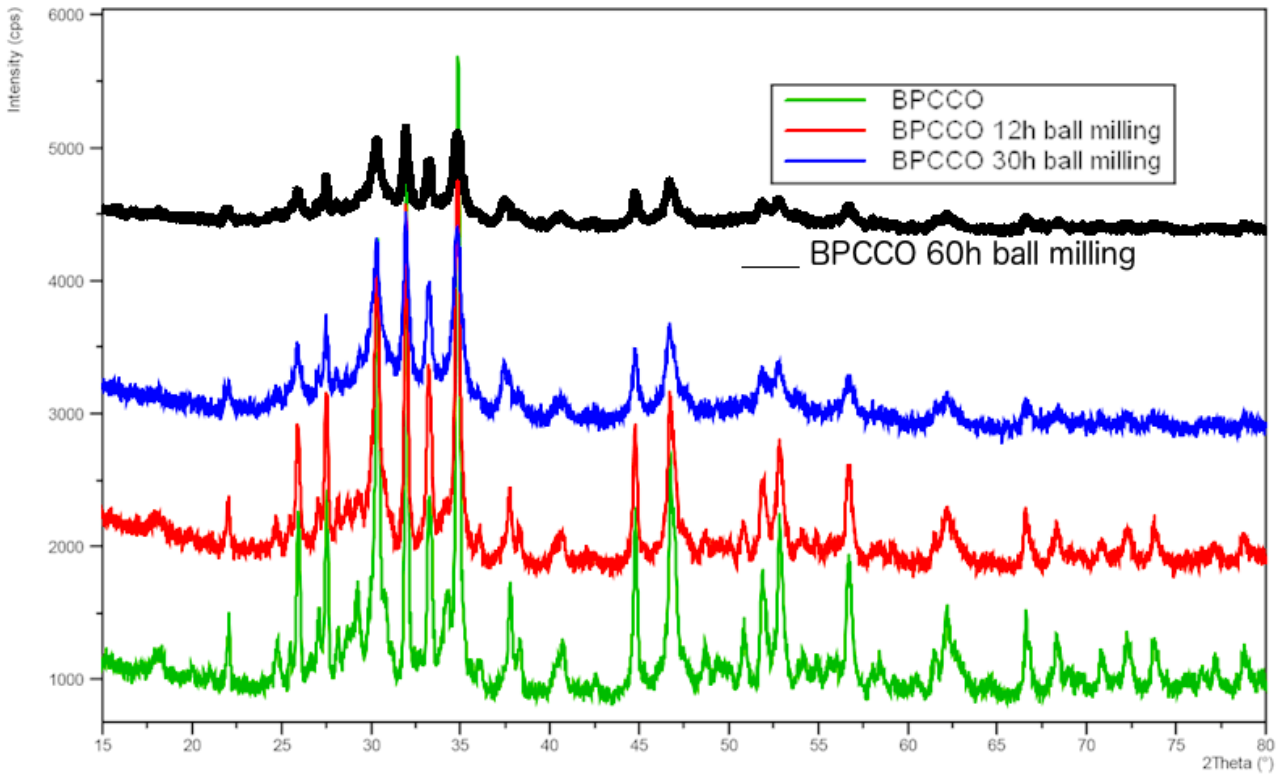

Figure 2.13. The X-ray diffraction was performed on the powders (containing all required elements except thallium) after mixing them for different hours

The pellet prepared with milled powder has grains more minor than the pellets usually prepared with the usual grinding process. The pellet sample SEM micrograph show grain sizes vary from 3 to 8 µm and the nonexistence of impurities (fig. 2.14). It can be concluded that the fine mixing and grinding for an extended period not only aids to grow tinier and refined grains but promotes pure phase.

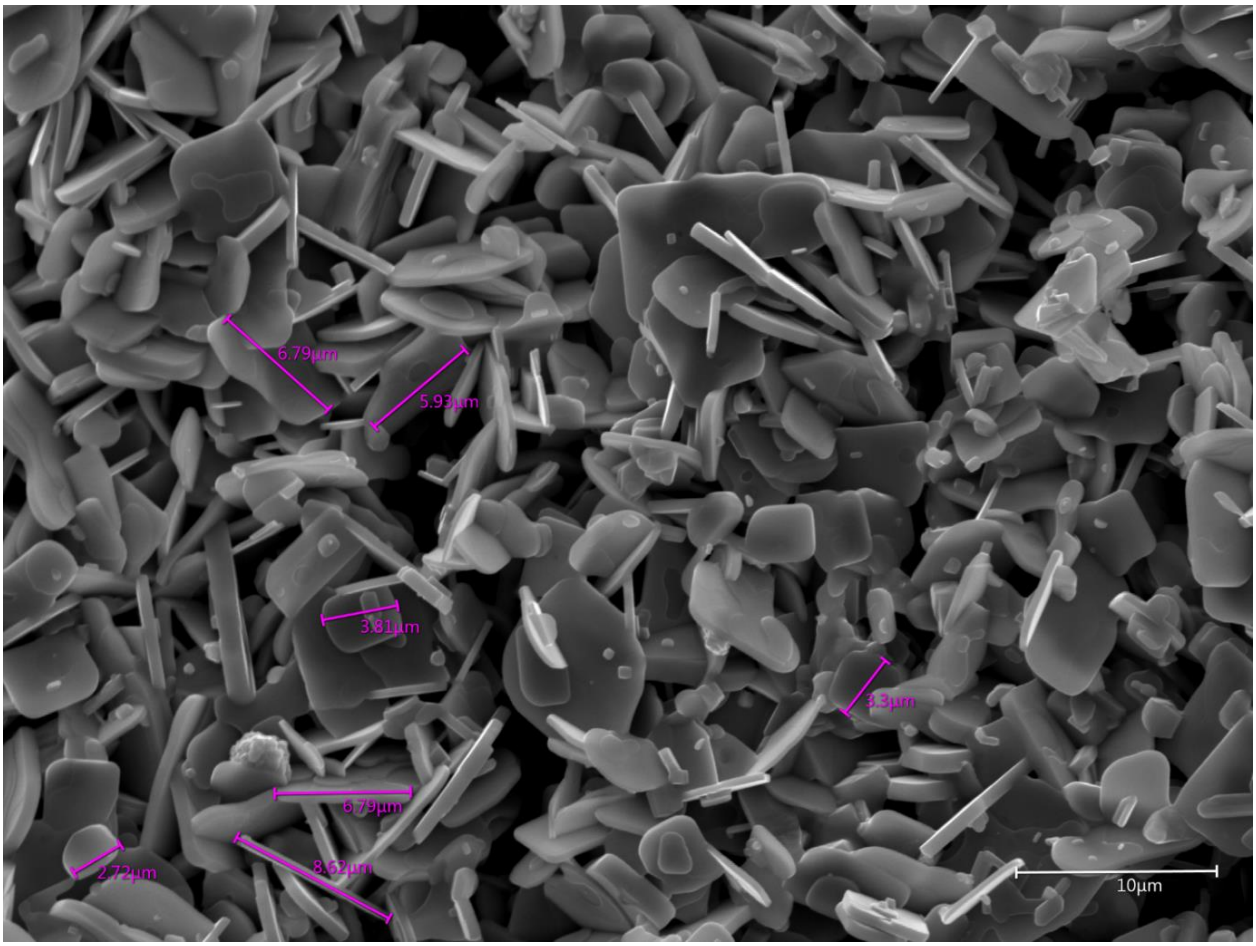

Figure 2.14. SEM image of a superconducting pellet prepared with milled powered

2.2.3 Four Probe Method for resistivity

The widely used four-probe method was used to measure the critical temperature of the Tl, Pb, Bi-1223 bulk sample. First, all four contacts with silver paste were made to the surface of the superconducting sample (10×10 mm). And then soldered with the probe stick was inserted with a liquid Helium (He) bath, and the temperature was controlled with a Cernox temperature sensor.

To perform the measurements, ten mA current was applied with Keithley current source. And resistance was measured as a function of temperature. The critical temperature T_C of the sample is calculated at 120 K of the pellet prepared with 60 hours milled powder (fig. 2.15).

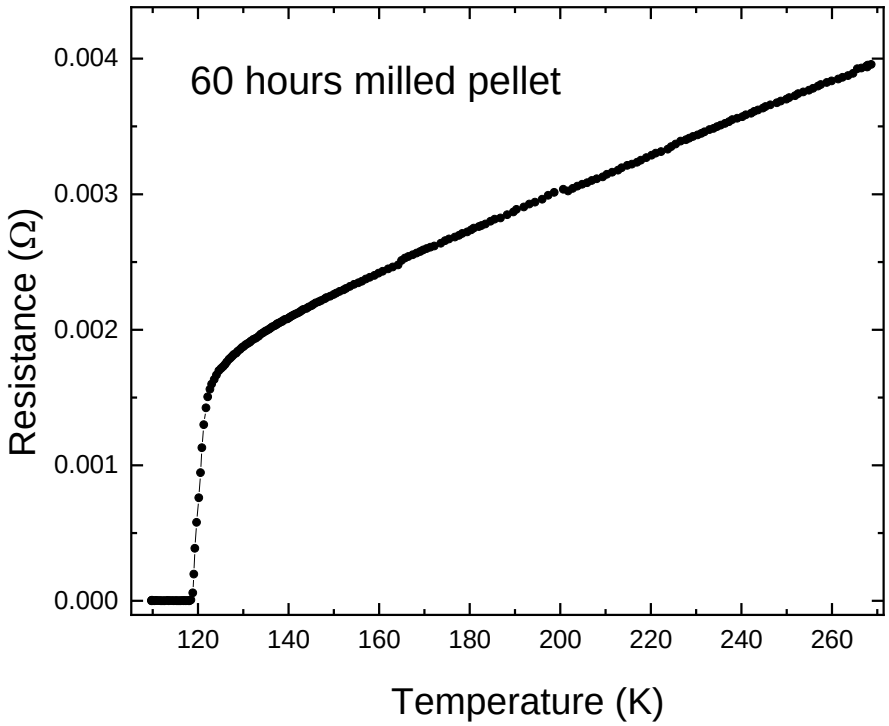

Figure 2.15. The resistance Vs temperature graph of the milled bulk sample

2.3 Conclusions

Among the other high-Tc superconducting cuprates, Tl-1223 retains exceptional superconducting properties: High critical temperature, high irreversibility field. And the superconducting properties can be further improved by substitutions. Moreover, Tl-based oxides can be prepared with a simpler and shorter process than Y-123. The problem of thallium toxicity can be managed with exhaust systems and elementary precautions.

The optimising recipes and techniques to prepare the bulk samples have been described in this chapter. The prepared thallium-based samples have shown high purity of 1223 phase and critical temperature around 118 K, while the estimated irreversibility field (20 T, 65 K) for Tl-1223 is high (even higher than the present literature). The four-probe resistivity measurements are also performed on a high-quality pellet sample prepared with ball-milled powder. And the critical temperature Tc is calculated to be 120 K.

Further characterisations: Scanning electron microscopy (SEM), tunnelling electron microscopy (TEM), scanning hall probe microscopy, and surface resistivity measurements were performed on the prepared thallium-based bulk superconductors (detailed in Chapter 4) and also Residual Gas analysis (RGA) and secondary electron yield (SEY) were performed on thallium-based bulk samples to verify their potential as a vacuum-compatible material (Chapter 5).

Chapter 3: Advancement made on Electrodeposited Tl-1223 superconducting thin films

3.1 Introduction to electrodeposition

As mentioned in the first chapter, the most practical challenge that must be satisfied to allow high-temperature superconducting coatings is to successfully fabricate low-cost and high current density coatings with suitable mechanical properties.

In this research, several techniques have been studied to fabricate and improve Tl-1223 thin films. Moreover, the electrodeposition method offers several advantages: simple, fast, cost-effective, deposit able on the nonplanar surface (that will help us to deposit on the prototype of FCC'S beam screen), and most importantly, electrodeposited thin films are highly reactive that helps to reduce the required treatment time and temperature in comparison to other superconducting powder calcination approach.

The fundamental principle of electrodeposition is based on the electrochemical process associated with deposition (scientifically called reduction) of metal ions, in the presence of an applied potential, from the electrolyte solution in the form of a metallic coating on the desired substrate[73]. A schematic cell setup, shown in Fig. 1, is used for electrochemical deposition and cyclical voltammetry. The cell consists of the working electrode (WE), the counter electrode (CE) and the reference electrode (RE) attached to the potentiostat. The working electrode carries out the electrochemical reduction, and coatings are deposited on the surface of the substrates. When a reduction occurs on the working electrode due to applied potential, current starts to flow through the electrolyte and complete the circuit; a counter electrode is used, so the current flows between the CE and WE. Since oxidation occurs at the counter electrode, an inert element such as platinum is usually chosen as CE.

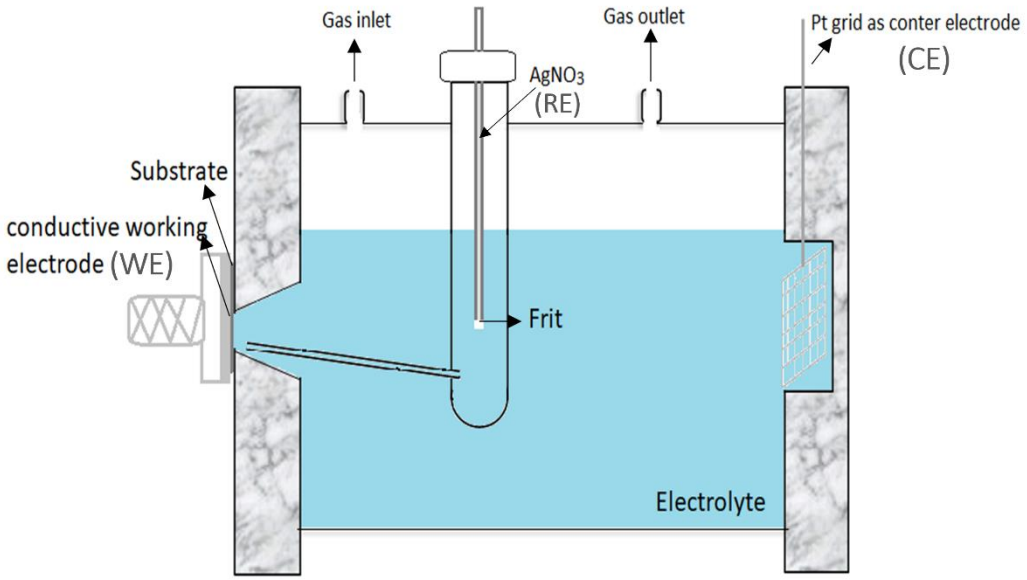

Figure 3.1. A schematic three-electrode cell

The reference electrode is used to measure the applied potential comparative to a steady reference reaction in the cell. The working, counter and reference electrodes are the chosen substrate, platinum grid, and $Ag/AgNO_3$.

3.2 Experiment Electrodeposition

3.2.1 Electrodeposition of thallium based high-temperature superconductors on silver substrates

Electrodeposition is an economical method to deposit thallium based high-temperature superconducting coatings. Bhattacharya et al. [74]–[76] have shown the capability of electrodeposition process by preparing biaxially textured thallium based thin film with J_c of 0.784 MA cm^{-2} at self-field and 77 K. furthermore, to fabricate thallium based thin-films, an electrochemical deposition procedure in a 3-electrode system on suitable substrates: silver or strontium titanate ($SrTiO_3$) was used.

Nonaqueous solution dimethyl sulfoxide (DMSO) was used because, in aqueous solutions, the water reduction is more favourable, giving rise to gas bubble formation[77]–[79] on the surface of the substrate and limiting the deposition of thallium and other elements.

Bellingeri et al. [80] successfully deposited Tl-1223 thin films on Ag tapes using electrodeposition prepared with required elements dissolved in Dimethyl Sulfoxide (DMSO). Their recipe was primarily adopted to obtain $Tl_{0.7}Pb_{0.2}Bi_{0.2}Sr_{1.6}Ba_{0.4}Ca_{1.9}Cu_3O_{9+\delta}$ (Tl-1223) precursor composition. First, many electrolyte baths with different quantities of elements were prepared, and later the modifications were implemented to achieve the reactive precursors of desired 1223 stoichiometry. First, the amount of Analar or Puratronic grade pure nitrates of the required elements, given below (Table 3.1), was added to 250 ml of DMSO (Sigma-Aldrich, 99.9%, anhydrous) electrolyte of the thin film precursors.

Table 3.2. Measured quantities of required elements dissolve in 250 ml of DMSO

Element	Weight (g)
$TlNO_3$	0.266
$Bi\ (NO_3)_3.5H_2O$	0.1623
$Pb\ (NO_3)_2$	0.188
$Sr\ (NO_3)_2$	3.8714
$Ba\ (NO_3)_2$	2.323
$CaN_2O_6.4H_2O$	1.63
$Cu\ (NO_3)_2.\ H_2O$	1.25

After adding nitrates to DMSO, the solution was stirred overnight with the help of a magnetic stirrer at 120 °C under the fume hood.

3.2.2 Preparation of Substrates

It is well known that the substrates always play a vital role in the growth of a thin film because they are, generally, the passive components. A suitable substrate itself must have a good surface quality, homogeneity, and smoothness. At the same time, it must be chemical compatibility, unreactive, suitable thermal expansion matches with the HTS material. The

regulated crystallographic orientation of the films to the substrates is required for epitaxial growth. For instance, matching the film and substrate in lattice parameters, atomic locations, crystallographic orientation, and other factors is required. The closer these parameters correlate, the much more likely high-quality epitaxial growth will occur [81].

Thallium based thin films have been deposited on various substrates, including $SrTiO_3$, $LaGaO_3$, MgO, $NdGaO_3$ and sapphire[82]–[86]. Silver (Ag) is one of the metal substrates that has received the most consideration as HTS substrate because it does not react adversely with HTS materials. Therefore, it is used to enhance the transport properties of HTS materials[87]–[90]. The research concentrated on the preparation and investigation of silver since many work efforts[86] show the suitability of silver for thallium-based superconductors.

The requirement of a metallic substrate for the deposition of precursor via electrodeposition makes silver one of the most suitable for this research. To prepare the silver substrates for the deposition, A rolling machine was used to flatten the silver rods or ingots. The thickness of the silver was reduced 20% after each pass to obtain different thicknesses, usually down to 40 µm (fig. 3.2).

Figure 3.2. Pre annealed silver substrates of thicknesses different 50 µm,100 µm, 130 µm

After getting the silver foil, annealed the rolled silver ribbons, as the melting point of the silver is around 960 °C, close to the treatment temperature (900 °C) is required to form the thallium 1223 phase. So before depositing a precursor on the silver substrate, the silver substrates are cleaned with acetone and ethanol and treated at 900 °C for 1 hour in the

oxygen to reduce the stress and stabilise it for the final treatment at high temperatures. Successively, annealed silver substrates were finally cleaned using compressed air to remove dust particles from the surface (we cannot use solvent + ultrasonic because the silver is fragile and after the heat treatment is so soft that the ultrasonic cleaning induces much bending).

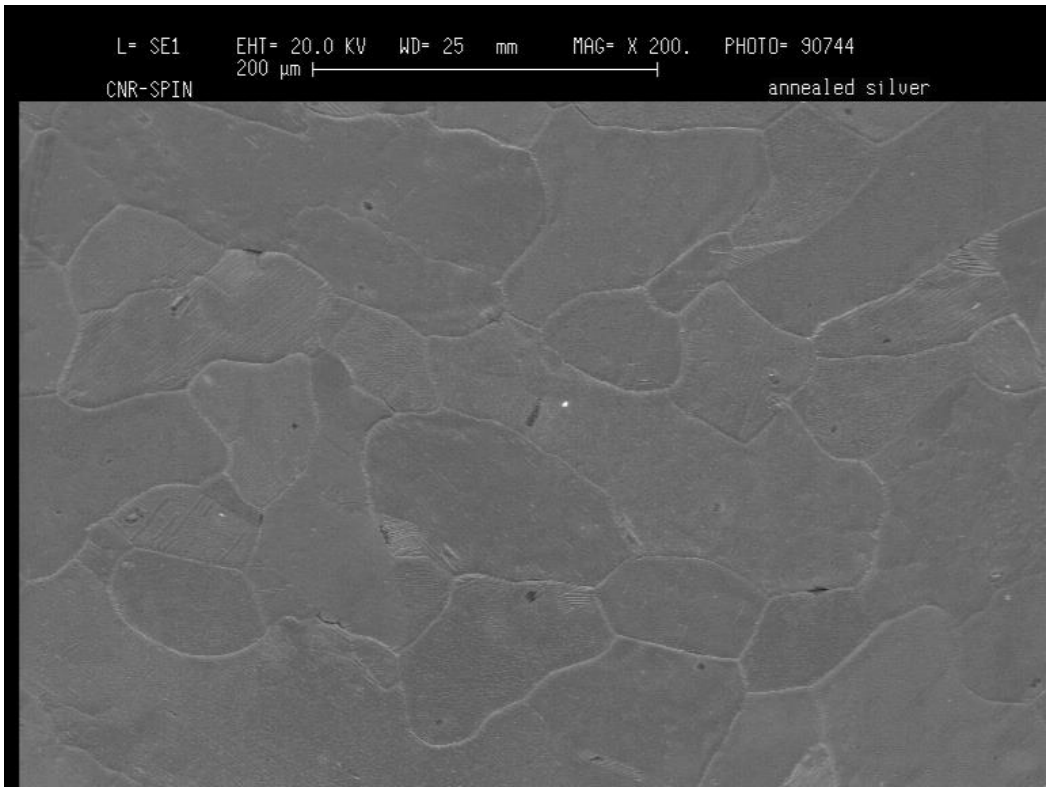

Figure 3.3. Scanning electron micrograph of a post annealed silver substrate with clear grains

The X-rays diffraction has been applied to the 50 and 80 µm (fig. 3.4). The pattern shows the improvement in the grain orientation as the thickness reduces, and the roughness of the surface of the silver substrate is calculated at about 28 nm (fig 3.5) since new rolls with the roughness of about 20 nm were used to achieve the desired thickness.

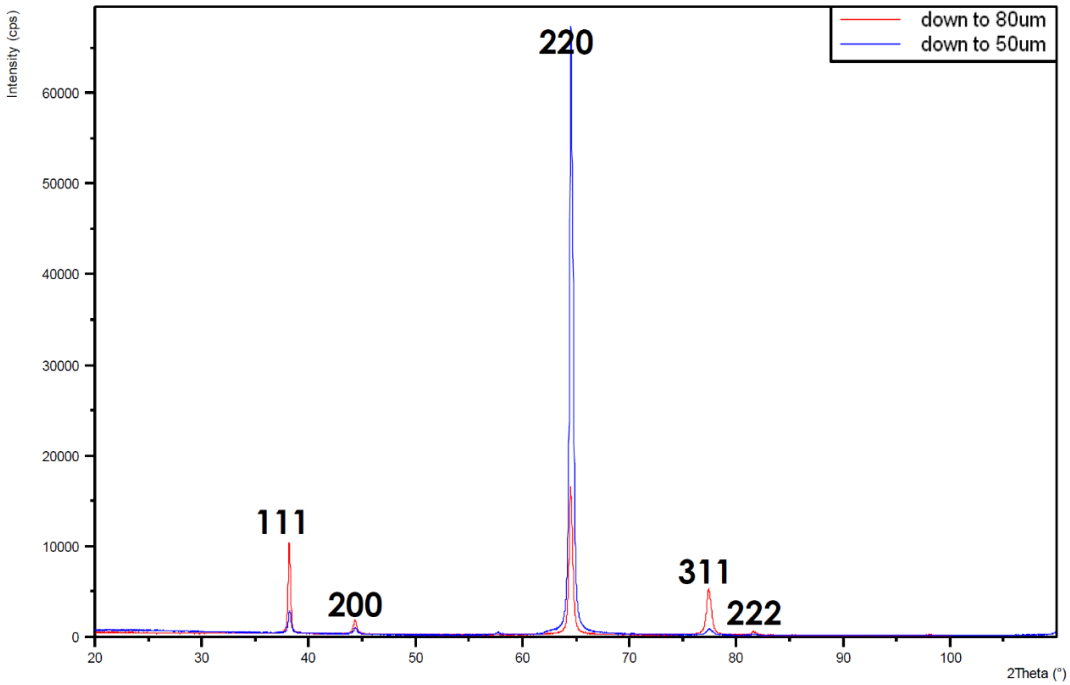

Figure 3.4. X-ray diffraction of a post annealed silver substrate with different thicknesses

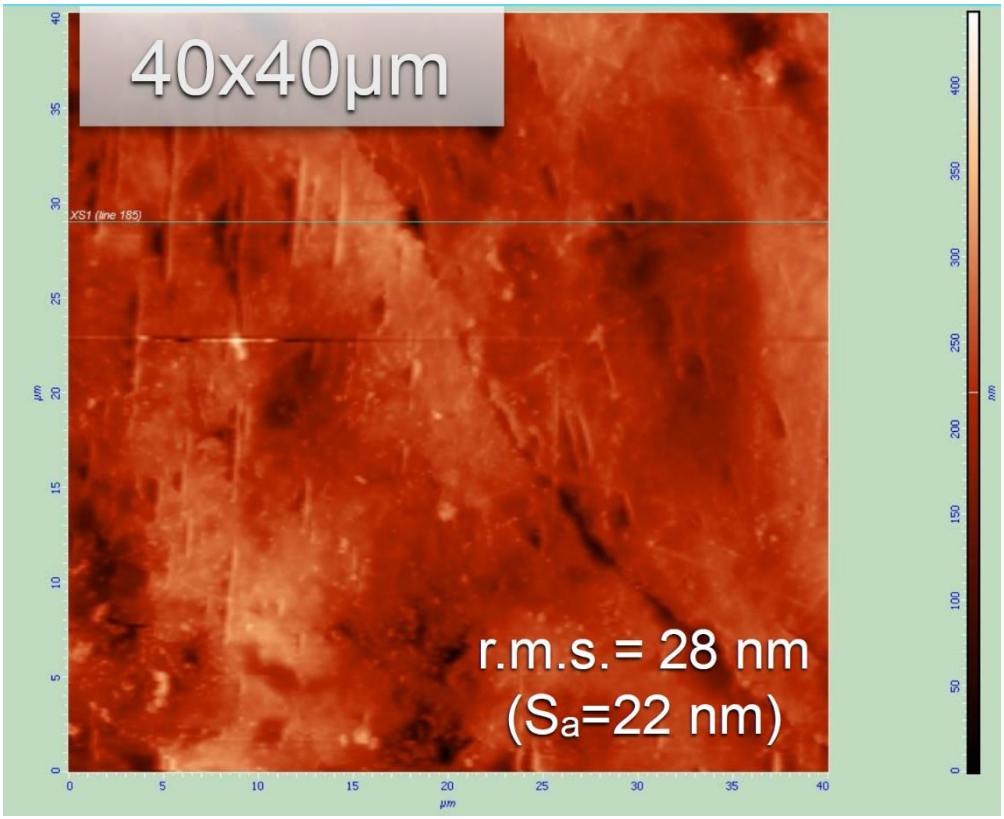

Figure 3.5. Atomic force microscopy (AFM) analysis of a silver substrate

3.2.3 Cyclical voltammetry

Cyclic voltammetry is a powerful and common electrochemical technique customarily applied to explore the oxidation and reduction processes of the elements. In the cyclic voltammetry experiment, the applied potential is swept from a starting potential to another, and the responding current is recorded. The study of cyclic voltammetry on the high-temperature superconductors [91]–[93]has shown that it facilitates adjusting the deposition parameter to obtain an expected chemical composition.

Cyclic voltammetry was performed to determine the potential for thallium-based thin-film precursor deposition (figure 4). Then, a solution was prepared by dissolving: 0.2626 g Tl(I), 0.19 g Pb (II), 0.1625 g Bi (III), 284 4.3523 g Sr (II), 2.32 g Ba (II), 1.64 g Ca (II), and 1.25 g Cu (II) nitrates in the 250 ml DMSO. And it was poured into the assembled cell that was connected to the potentiostat.

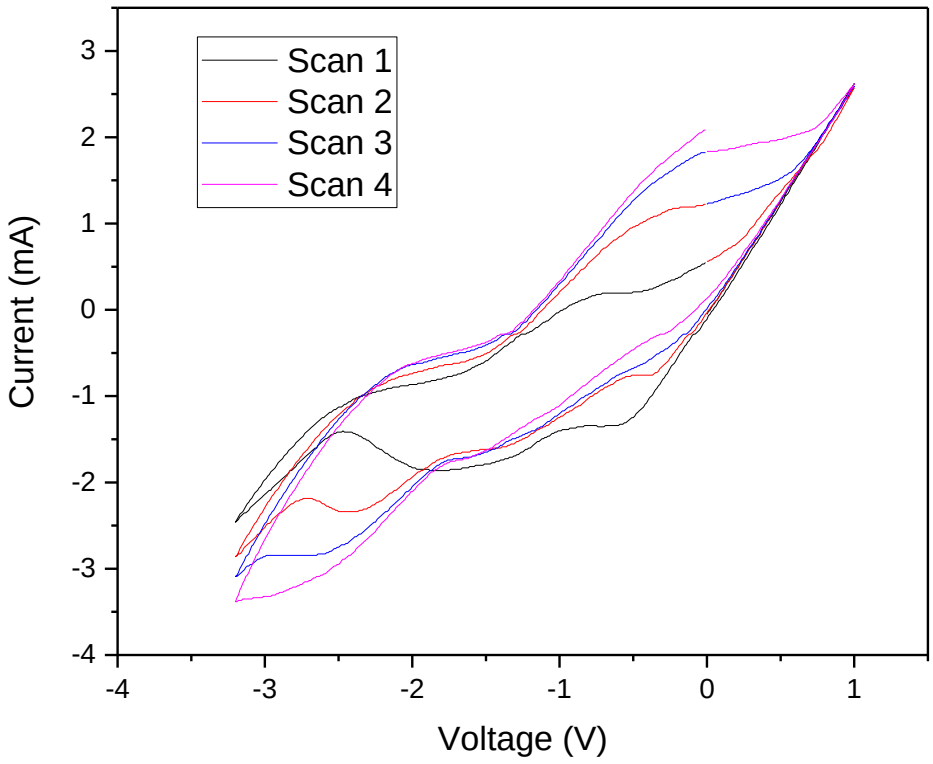

Figure 3.6. Cyclic voltammogram for a solution containing Tl, Bi, Pb, Sr, Ba, Ca, Cu dissolved in DMSO solvent. 4 consecutive scans show the shift of peaks indicating the loose change in the solution after the deposition

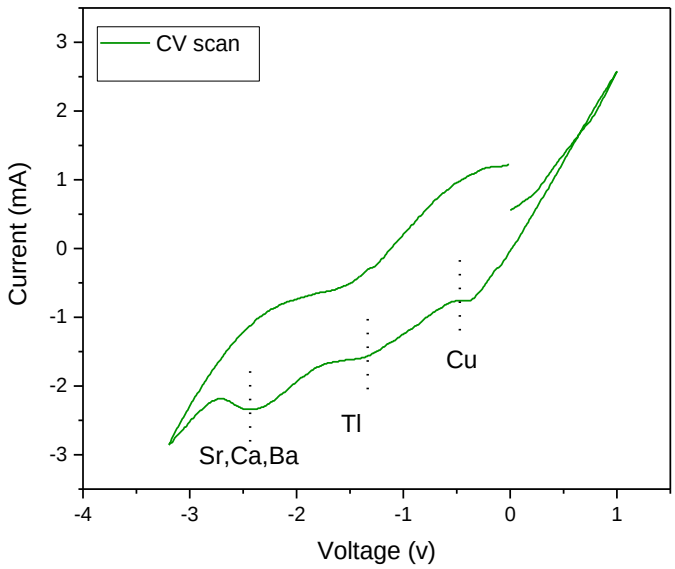

Figure 3.7. Cyclic voltammogram for a solution containing Tl, Bi, Pb, Sr, Ba, Ca, Cu dissolved in DMSO solvent.

The potential was started from zero, and the first potential vortex 1 V (the turning point of the cycle) and other -3.2 V, and the scan rate was set to 50 mV/s and continued for 10 minutes. In figure 3.7 shows a CV scan or scientifically called cyclic voltammogram of cyclical voltammetry. The voltammogram was recorded with a silver foil, and the x-axis represents the applied potential (V), whereas the y-axis is the current (I) passed during the CV. As soon as the voltage was applied, a black thin black film appeared on the surface, corroborating the deposition process. The reduction potential of Tl(I), Pb (II), Bi (III), Sr (II), Ba (II), Ca (II), and Cu(I) are reported in table 3.2.

Table 3.3. The reduction potentials of the elements with respect to $Ag/AgNO_3$

Elements	Reduction potential
$Tl^{1+} + 1e \rightarrow Tl$	-1.36
$Sr^{2+} + 2e \rightarrow Sr$	-2.89
$Ba^{2+} + 2e \rightarrow Bi$	-2.58
$Ca^{2+} + 2e \rightarrow Ca$	-2.58
$Cu^{2+} + 2e \rightarrow Cu$	-0.74

As shown in figure 3.7, several peaks correspond to each metal ion of the elements. For example, when the potential cycling started, a cathodic peak appeared for -1.3 V for Tl (I), -

0.47 for Cu (II), and followed by an overlapped peak at -2.45 V indicates the co-deposition of all Ca (II), Ba (II), Sr (II) ions.

3.2.4 Deposition of the thallium films at constant potential

The electrolyte containing cell connected to the potentiostat and the depositions were recorded using software IVIUM model no. V43214 to initiate the deposition of the precursors. Initially, the samples were deposited at constant potential -3 V and 24 °C. Then, the deposition potential was set to -3 V for ten minutes of deposition. Usually, the films deposited at constant potential are approximately 3µm, so the deposition rate is 0.3 µm per minute (figure 3.8). The graph shows a relationship between current and the time during a deposition on a silver substrate.

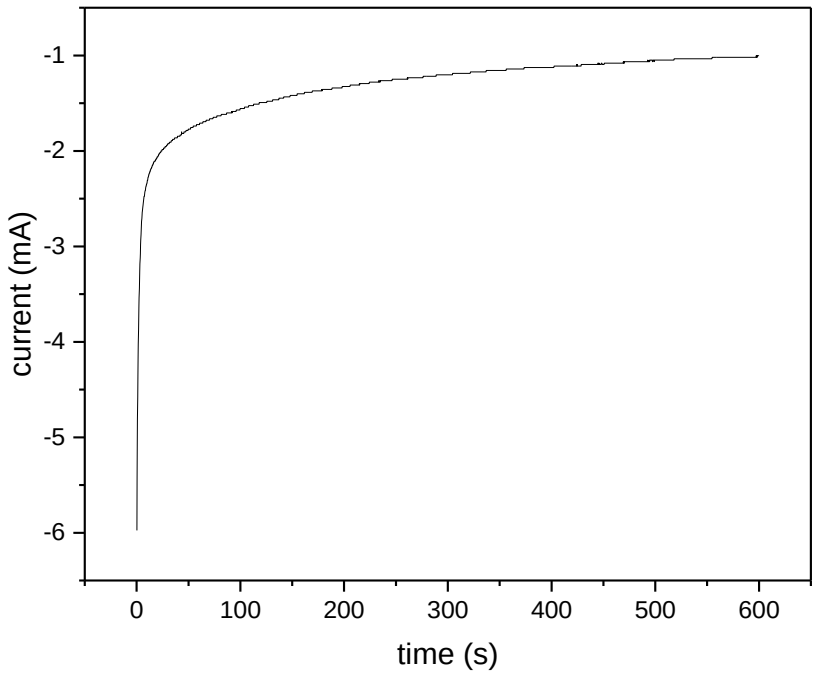

Figure 3.8. Current Vs time graph during a deposition process under a constant potential

Figure 3.9. SEM of electrochemically Tl based thin film precursor under constant potential

During the deposition, the thickness of the film increases either by depositing new material on the substrate or previously deposited material. If there is a low population of adatoms, high surface diffusion and low overpotentials, there would be build-up on old nucleation; inversely, a high population of adatom, low surface diffusion and high overpotentials create new nucleation centres [74].

Furthermore, a few films were made to increase the thickness of the precursor by increasing the time deposition because the electric conductivity of the surface remains the same. Moreover, deposited precursors were insulators, and film precursors became more insulating with increasing time, thus thickness [94].

The films deposited on a set constant potential were optimised to achieve a stoichiometry ratio but contained the traces of bubbles that made films less thick. Since the formation of a bubble is a barrier between the substrate and the ions of the elements. So, to improve the thickness and homogeneity, the pulse potential deposition or plating technique was adopted.

3.2.5 Deposition of the thallium films at pulsed potential

Pulse potential deposition improves the homogeneity and morphology of the electrodeposited materials by reducing the bubbles that form on the surface. The morphology of deposited films is crucial because it certainly affects annealed films' structure and properties.

For the pulse potential process, the same recipe of the electrolyte was used. The pulsed potential precursors of thallium based thin films were deposited on silver foil substrates. Usually, a pulse deposition setting consisted of 31 levels, and there was always a 0.2-second gap after a particular time and deposition, and a deposition lasted for 603 seconds. The sequence for the pulse deposition is mentioned below (Table 3.3),

Table 3.4. Sequence for the pulse deposition

Level no.	Voltage (V)	Time (s)
1.	-3	10
2.	0	0.2
3.	-3	20
4.	0	0.2
5.	-3	30
6.	0	0.2
7.	-3	30
8.	0	0.2
9.	-3	30
10.	0	0.2
11.	-3	30
12.	0	0.2
13.	-3	30
14.	0	0.2
15.	-3	30
16.	0	0.2
17.	-3	30
18.	0	0.2

19.	-3	30
20.	0	0.2
21.	-3	30
22.	0	0.2
23.	-3	60
24.	0	0.2
25.	-3	60
26.	0	0.2
27.	-3	60
28.	0	0.2
29.	-3	60
30.	0	0.2
31.	-3	60

Moreover, figure 3.10 shows the flowing current during a pulse deposition.

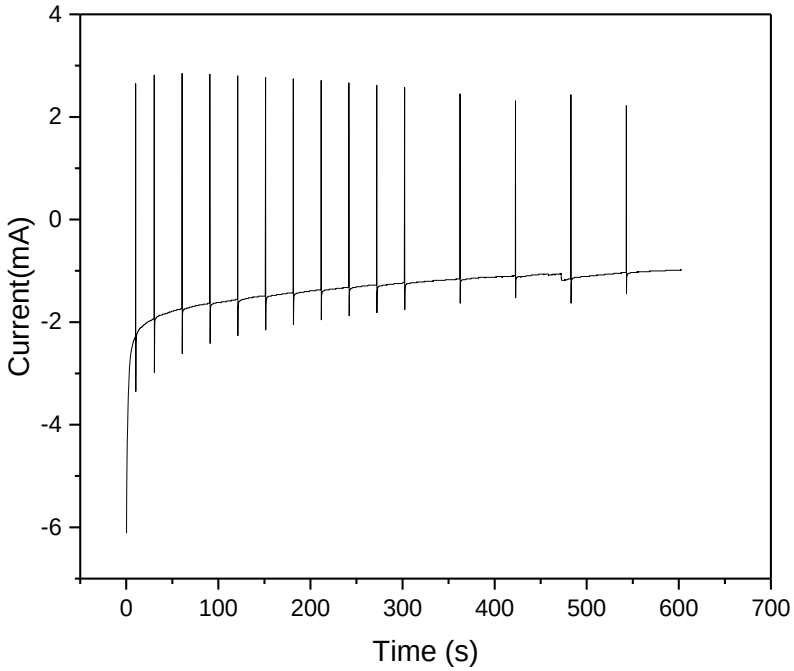

Figure 3.10. Current Vs time graph during a deposition process under a pulsed potential

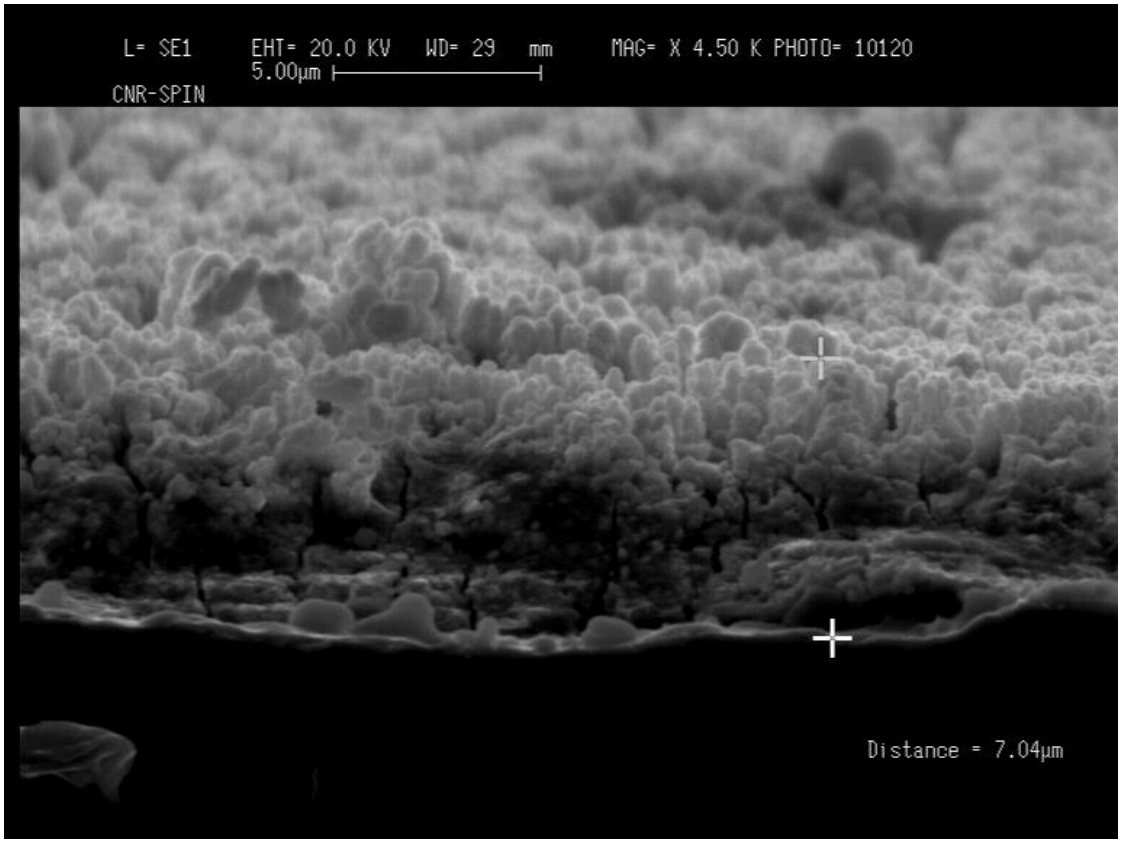

Figure 3.11. SEM of electrochemically Tl based thin film precursor under pulse potential

The SEM image of the pre-treated precursor under pulsed potential is shown in fig. 3.11. It can be seen that the reactive precursor is denser and more compact compared to the precursors deposited at constant potential (figure 3.9). Moreover, the imporous structure even helps to deposit thick material in ten minutes.

3.2.6 Heat treatment techniques for the electrochemically deposited thin films

The precursors deposited on silver substrates were usually annealed for 10-50 minutes at 885 °C in the presence of the thallium source. The final treated films are usually 1 µm thick.

After the completion of deposition time, the thin film samples are carefully removed from the electrode with the help of the tweezers. Afterwards, the films are dried in a vacuum at 120 °C for almost 1 hour.

After vacuum drying the deposited precursors, choosing the proper annealing parameters are essential to be considered. Since the quality of final annealed films directly affects its properties. In this research, plenty of time was dedicated to optimising the thin films and enhancing the phase. The growth of thallium-based thin films with the desired phase is somewhat complicated because of various uncontrollable parameters. Therefore, some areas were needed to be elucidated to improve morphology and phase grains. The first and the most critical parameter to be considered is the heat treatment time and temperature.

Literature [74], [95]–[97], [97], [98]shows that the most favourable temperature for the formation of thallium based superconducting phase is around 900 °C, and time may vary from 10 minutes to one hour, depending on the source. Therefore, a wide range of temperature and time has been explored in this research.

Another of the most challenging phenomena is achieving the right thallium amount in the thin films, which is the main element of the phase. Since thallium oxide is volatile around 710 °C (in the air), the annealing temperature is usually around 900 °C, and thallium loss is inevitable, so it is essential to avoid thallium escaping thin films. So, a primary choice is annealing a thin film inside a tightly sealed capsule made out of a heat-treated gold foil. Moreover, the use of gold capsules can be found frequently in the literature related to thallium bulk and thin-film samples[94] because it is unreactive.

As cylindrical, conical, and square or rectangular packets, many gold capsule configurations were fabricated to minimise the joints to minimise the thallium escape.

Despite three joints, a square packet gold capsule was frequently used. Moreover, after the selection of the capsule, a thallination source is essential.

Many thallination sources were tested to understand the best route to achieve better coverage and enhanced phase.

Three major thallium sources are:

1. Reacted pellet with phase Tl-1223

2. Thallium powder Tl_2O_3

3. Unreacted pellet with the predicted.

Annealing post dried precursors thin films in a right thallous atmosphere helps to promote the growth of the Tl-1223 phase. So, the placement of a thallium source in the gold foil along with a dried precursor film is critical.

Different sizes of reacted thallium-1223 superconducting pellet, recipe mentioned in the previous chapter, were primarily used to thallinate the thin films. However, final annealed thin films contained the Tl-1212 phase.

Thallium powder (Tl_2O_3) as a source was investigated in detail based on the research [99], [100]. The electrodeposited precursors are around 7-8 mm in diameter, so at the outset, 10 mg of Tl_2O_3 powder was used to understand the growth of the phase. The SEM image of the first thin film sample treated with 10 mg is shown in Figures 3.12 and 3.13.

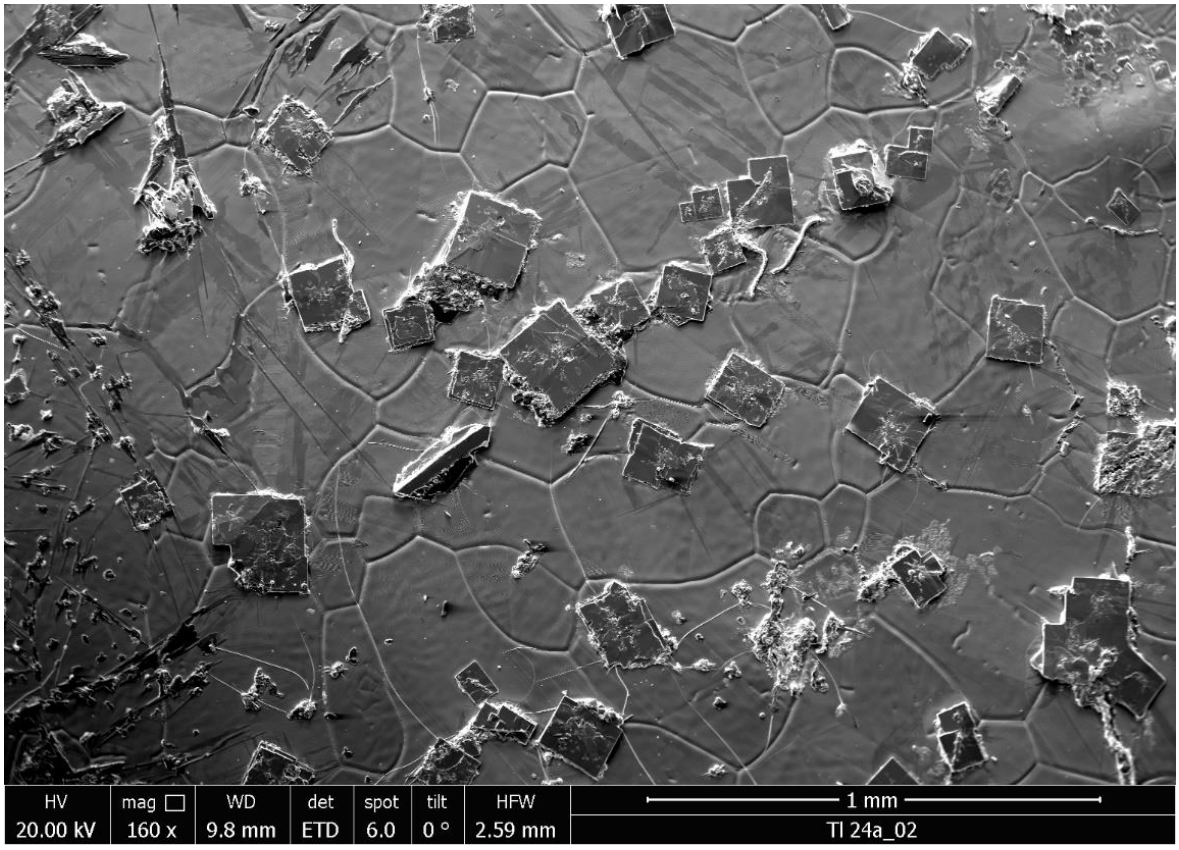

Figure 3.12. SEM of post-annealed Tl based thin film annealed with 10 mg of Tl_2O_3 powder

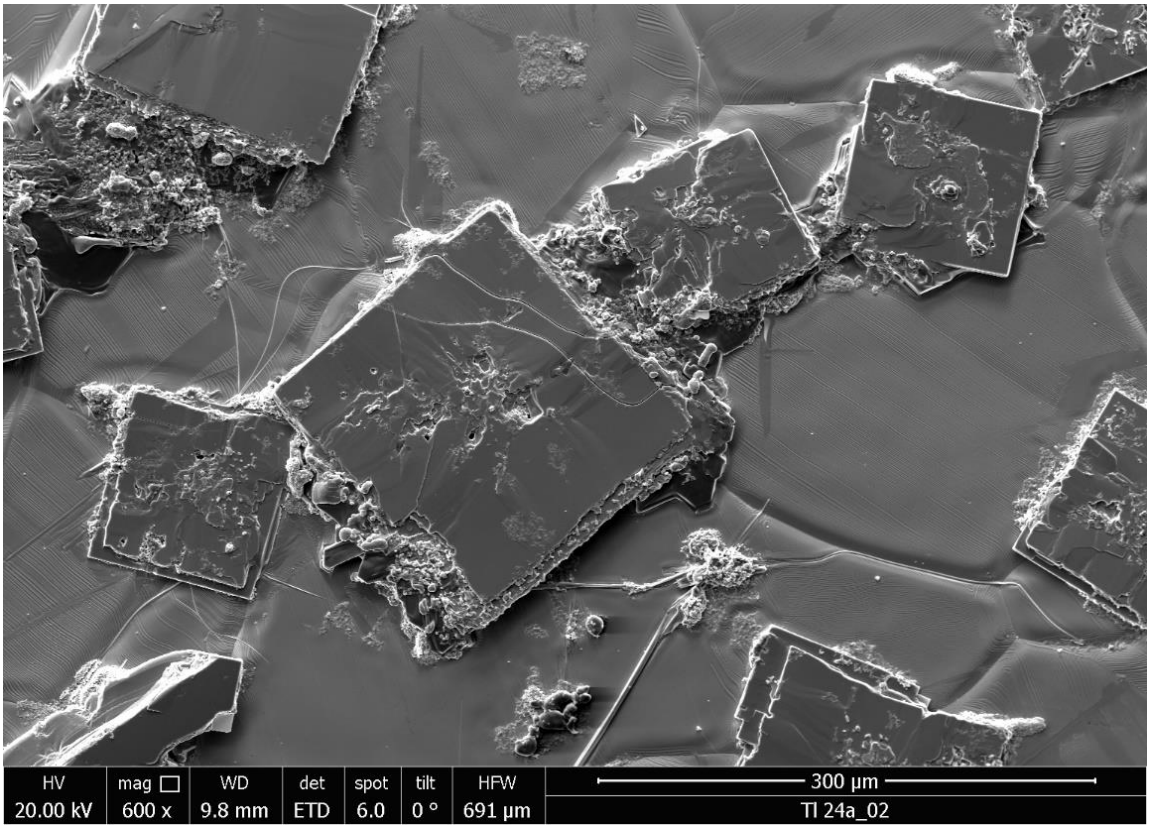

Figure 3.13. SEM of post annealed Tl based thin film shows the formation of big textured grains of about 100 µm size

The precursor of the shown (figure 3.14) film was deposited at constant potential -3 V and annealed at 885 °C for 10 minutes. The SEM images clearly show the growth of Tl-1223 grains in a particular direction along the grain boundary of the silver substrate. It can be seen that the substrate is poorly covered with the grains, and it suppress the superconducting properties to an adverse level since the electrically deposited particles accumulate to form grains, insufficient material deposited or thallium pressure to form a well-covered thin film. Figure 3.12 shows that the area covered is estimated at around 14.4 % using the software Image-Pro Insight.

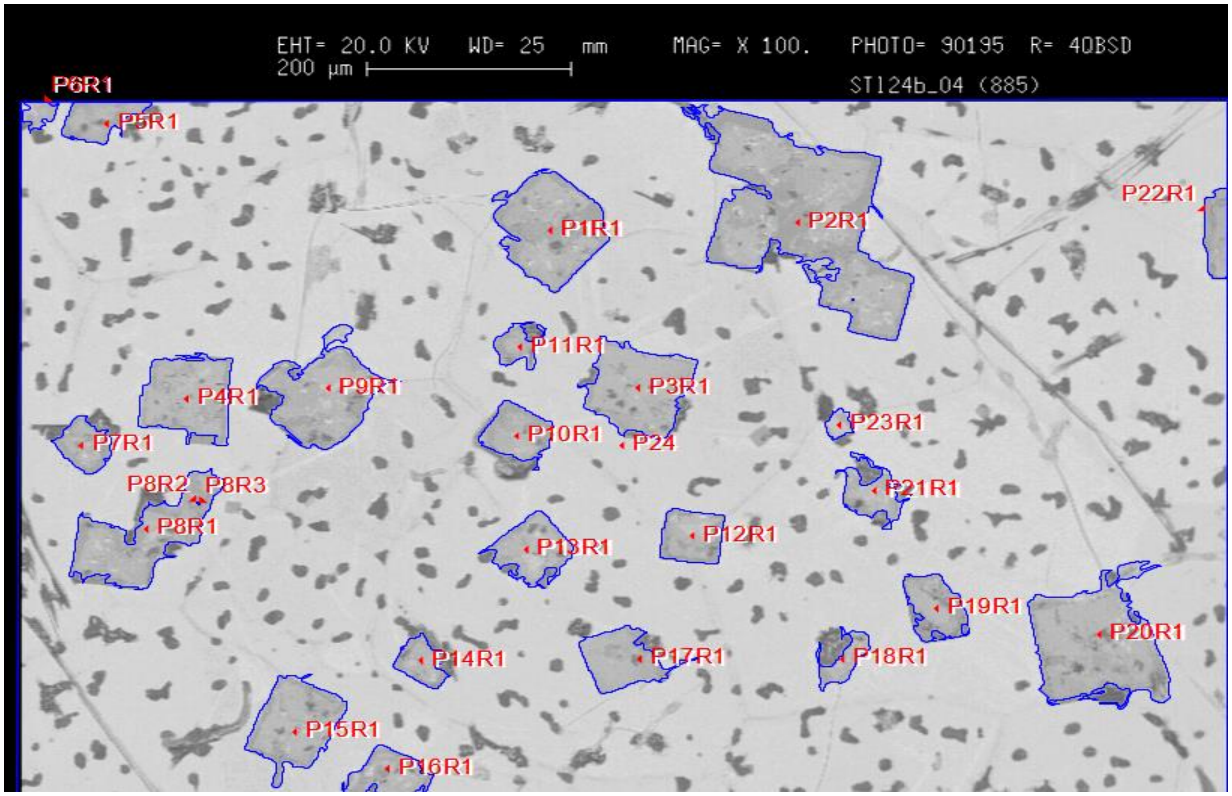

Figure 3.14. SEM of post-annealed Tl based thin film with 10 mg whereas blue lines are bordering the grains covering 14.4 % surface of the silver substrate

So, to improve the coverage, thallium pressure plays an important role hence the amount of thallium oxide. Moreover, the amount of thallium oxide powder was reduced to 8 mg from 10 mg. In the SEM image (figure 3.15, and corresponding table 3.4), it can be seen that the thickness has improved

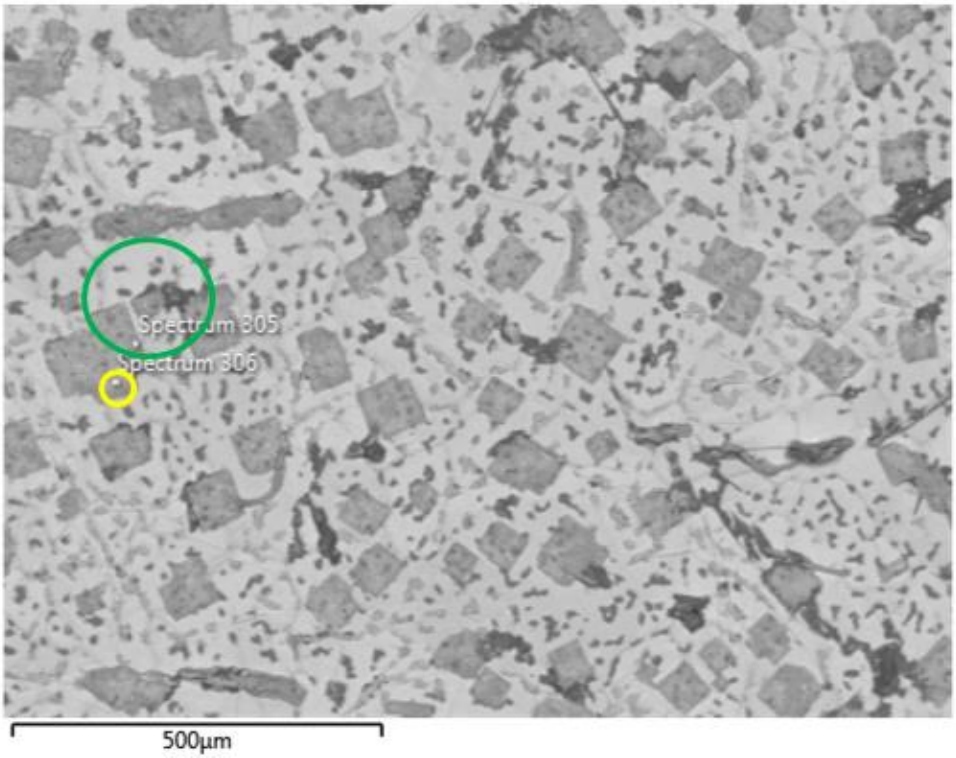

Figure 3.15. SEM of post annealed Tl based thin film annealed with 8 mg of Tl_2O_3 powder

Table 3.5. The spectra confirm the formation of 1223 and 1212 phases.

Quant Results View

Viewed Data: Multiple Spectra Result Type: Atomic %

Spectrum Label	O	Ca	Cu	Sr	Ag	Ba	Tl	Pb	Bi	Total
Spectrum 305	55.74	11.42	16.01	9.82	0.76	0.73	3.41	1.66	0.46	100.00
Spectrum 306	54.37	6.99	15.37	14.02	0.13	0.71	6.25	0.95	1.21	100.00

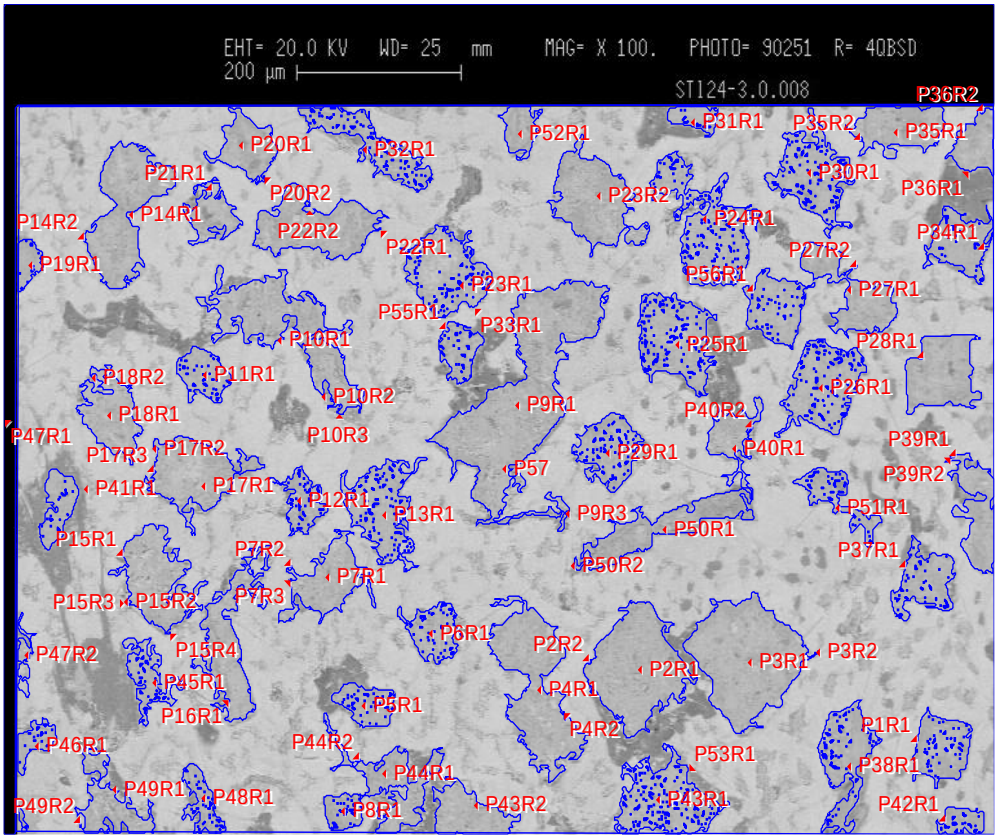

Figure 3.16. SEM of post annealed Tl based thin film with 8 mg whereas blue lines are bordering the grains covering 48% surface of the silver substrate

From figures 3.14 and 3.16, it can be shown that the covered area has drastically improved to 48 %, but Images 3.14 and 3.15 shows the formation of the Gainesboro-coloured thin layers of 1212 phase on the top of slate grey coloured 1223 phase and some oxides.

It was clear that after reducing thallium powder, the amount of covered area of superconducting grains on the substrates enhanced, so the amount of thallium oxide powder was further reduced to 5 mg.

Furthermore, SEM Image (Figure 3.17 and corresponding table 3.5) shows better coverage than before, and Figure 18 shows that the coverage has been achieved up to 80%. As the thallium oxide content was reduced, the coverage improved, but the Tl-1212 phase grew.

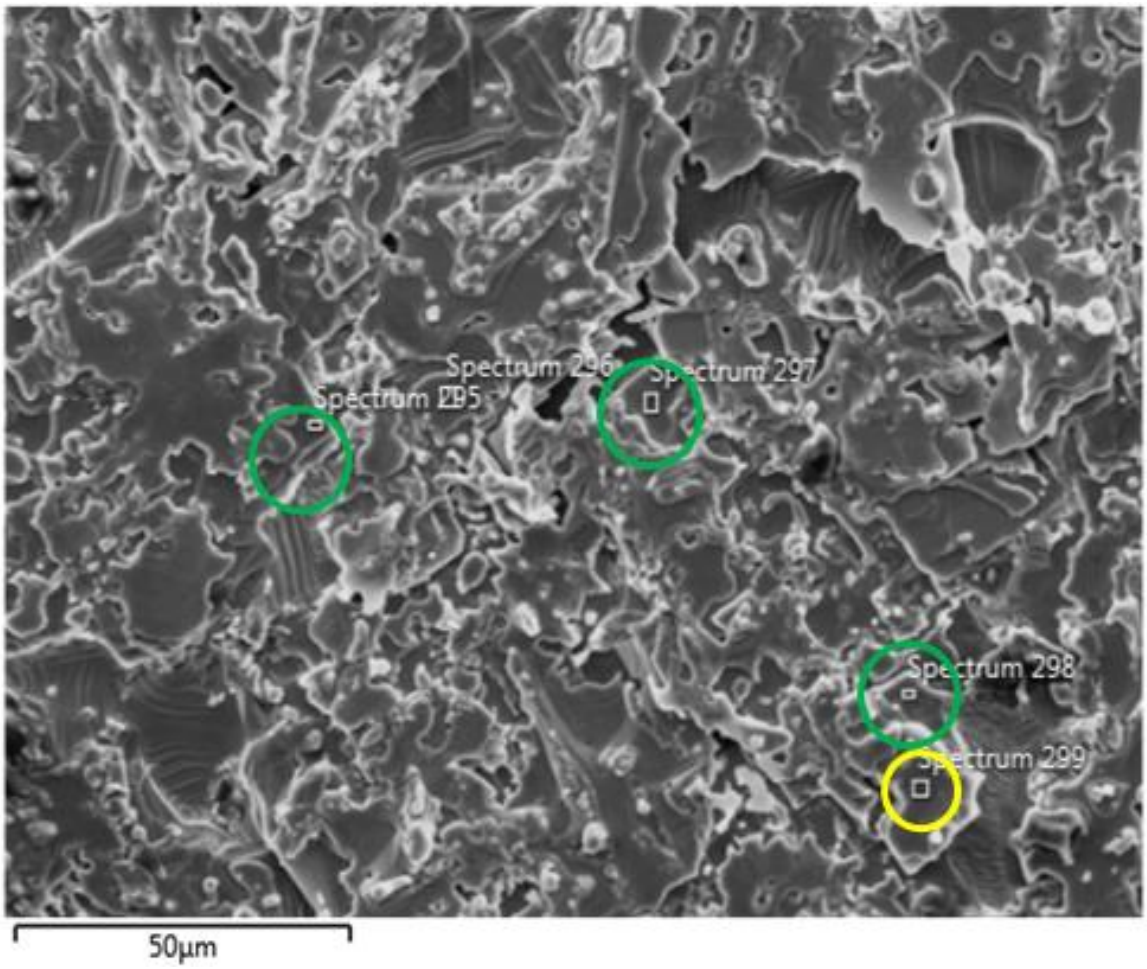

Figure 3.17. SEM image of post-annealed Tl based thin film annealed with 5 mg of Tl_2O_3 powder

Table 3.6. The spectra of the SEM image confirms the formation of 1223 grains in more than 1212 phases.

Quant Results View

Viewed Data: Multiple Spectra Result Type: Atomic %

Spectrum Label	O	Ca	Cu	Sr	Ag	Ba	Tl	Pb	Bi	Total
Spectrum 295	53.01	11.39	17.57	9.87	0.16	2.01	3.39	2.03	0.56	100.00
Spectrum 296	58.16	5.80	13.20	12.40	0.48	1.88	6.21	1.25	0.62	100.00
Spectrum 297	57.50	8.28	12.34	6.80	8.58	2.06	2.79	1.17	0.46	100.00
Spectrum 298	56.51	9.16	13.96	7.48	6.66	1.76	2.77	1.31	0.38	100.00
Spectrum 299	55.23	6.28	14.82	12.78	0.14	2.21	6.23	1.46	0.84	100.00

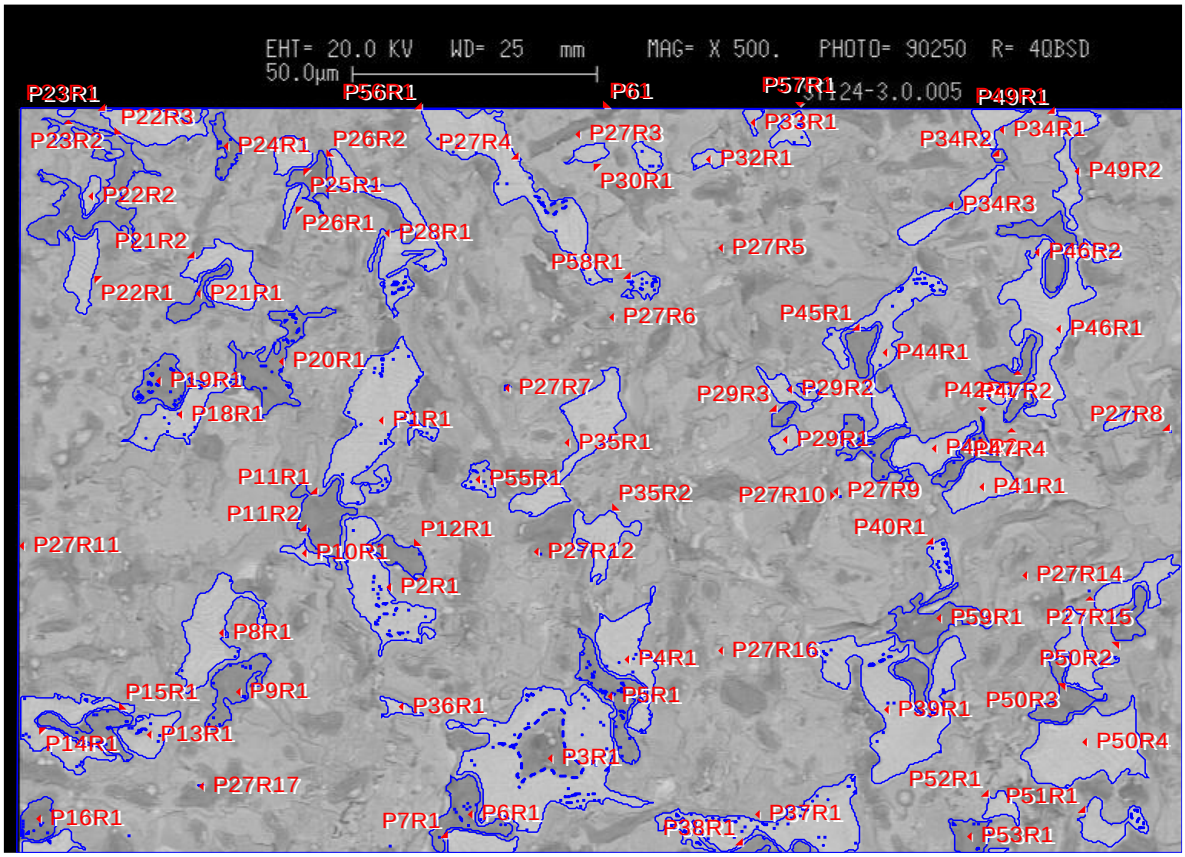

Figure 3.18. SEM of post-annealed Tl based thin film with 5 mg whereas blue line border indicating the grains covering is 80% on a silver substrate

Figure 3.19. SEM image of post-annealed Tl based thin film annealed with 3.7 mg of Tl_2O_3 powder

Table 3.6. The spectra confirm the green encircled grains of the 1223 phase.

Quant Results View

Viewed Data: Multiple Spectra Result Type: Atomic %

Spectrum Label	O	Ca	Cu	Sr	Ag	Ba	Tl	Pb	Bi	Total
Spectrum 330	53.48	11.85	16.52	11.29	0.86	0.38	3.20	1.91	0.51	100.00
Spectrum 333	53.59	11.83	16.13	10.88	0.32	0.62	3.84	1.98	0.81	100.00
Spectrum 335	50.13	12.24	18.46	11.94	0.16	0.72	3.57	2.07	0.71	100.00
Spectrum 336	52.15	12.01	18.24	11.16	0.00	0.49	3.45	1.71	0.80	100.00
Spectrum 337	49.61	8.18	17.22	14.58	0.16	0.92	6.25	2.00	1.07	100.00
Spectrum 338	45.22	43.62	1.21	0.65	5.64	0.06	3.23	0.13	0.24	100.00
Spectrum 341	52.22	10.26	17.03	11.97	0.13	1.25	4.88	1.66	0.60	100.00
Spectrum 342	53.24	8.77	13.76	8.93	9.40	1.22	2.48	1.64	0.56	100.00
Spectrum 343	54.30	7.26	15.34	13.04	0.16	1.30	6.55	1.56	0.49	100.00

Furthermore, the thallium oxide powder was reduced to 3.7 mg (Figure 3.19 and corresponding table 3.6) to understand the coverage and thallium powder quantity trend. It can be seen by the SEM that the thin film is quite covered Tl-1223 phase has improved, and Tl-1212 is reduced.

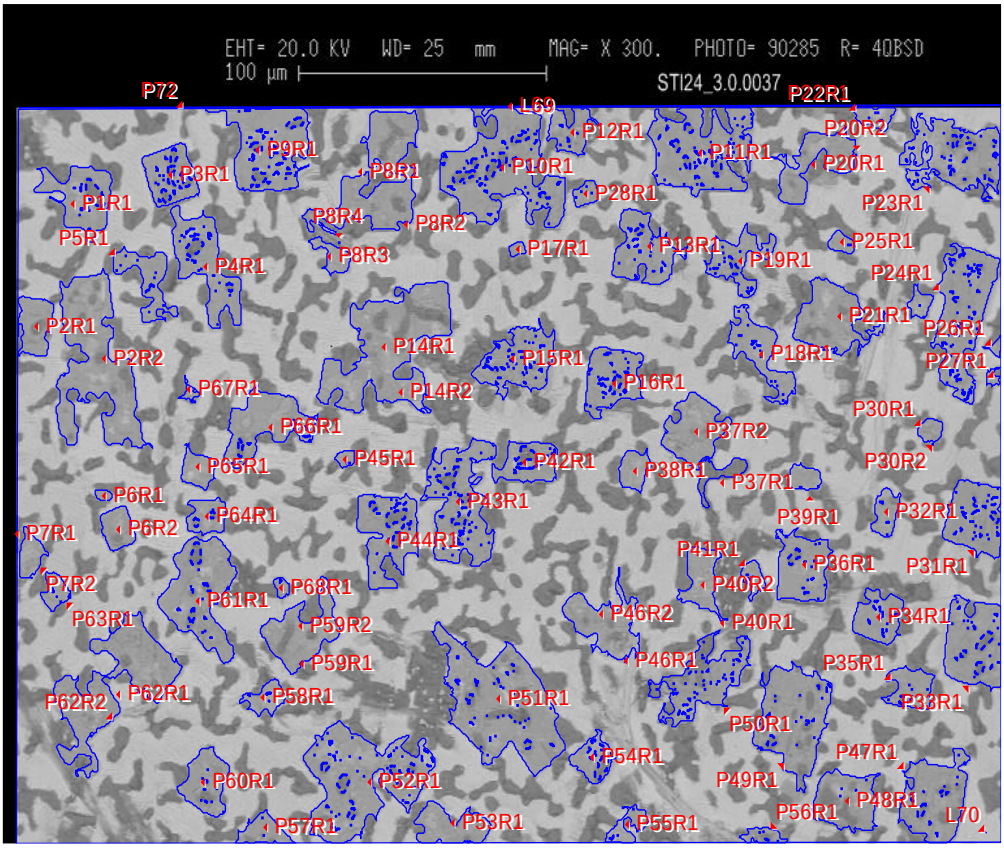

Figure 3.20. SEM of post-annealed Tl based thin film with 3.7 mg whereas blue line border indicating the grains covering is 40% on a silver substrate

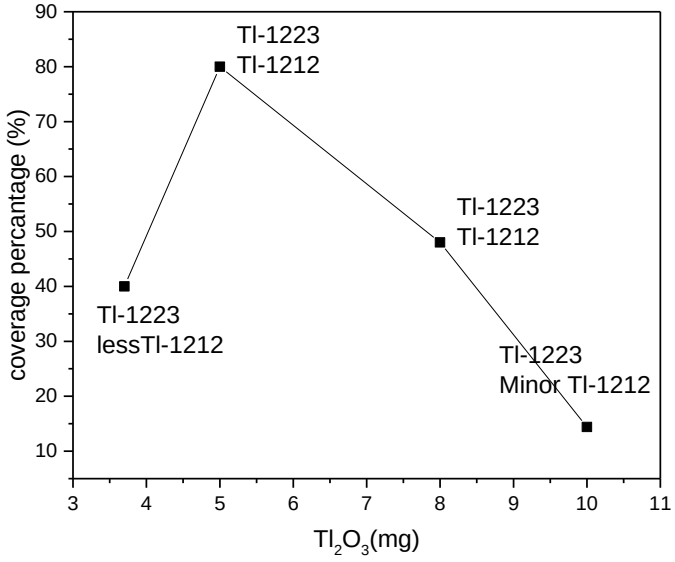

Figure 3.21. Percentage coverage of thin films related to the calculated amount of Tl_2O_3 powder

This graph (figure 3.21) shows the correlation between the thallium powder and the percentage area covered by the substrate with superconducting thin films. It is clear that complete removal for Tl-1212 is challenging, and this phase is always present, but reducing the amount of thallium oxide coverage has been improved. In the sample prepared with 5 mg of thallium powder, the film is well covered with material that somehow contains a significant amount of Tl-1212 phase. The thin films prepared with 3.7 mg have more than 40 % coverage but contain more Tl-1223 and a reduced Tl-1212 phase. Several thin films were prepared with 3.7 mg of Tl_2O_3 powder, and similar results were found. Notably, all the above-mentioned thin films were prepared with the same electrolyte, deposition potential, deposition time, annealing temperature, and time.

Moreover, the films deposited at 885 °C for 40 minutes with 3.7 mg of thallium oxide powder show the most suitable condition to grow thallium 1223 thin film. The grains grow in a particular direction, confirming the textured growth of the grains (figure 3.22).

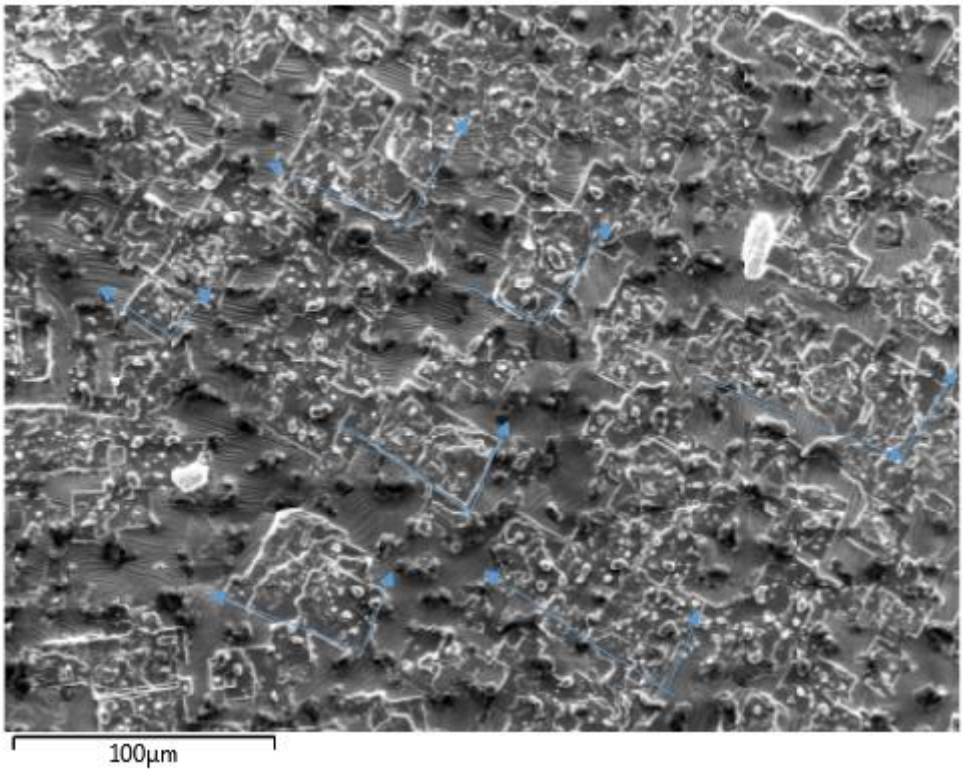

Figure 3.22. SEM image of post annealed Tl based thin film annealed with 3.7 mg of Tl_2O_3 powder shows the growth of textured 1223 grains

Later, the samples were primarily processed in a three-zone tube furnace in a partially closed system inside a gold foil crucible for 40 min at 885 °C along with Tl_2O_3 powder (3.7 mg) to help the growth of the Tl-1223 phase.

Annealing with unreacted-1223 films

As a thallination source, Thallium oxide content showed a significant improvement in the superconducting thin film samples; however, thallium pressure is challenging to control, hence reproducibility.

Another popular technique is reacting samples in the presence of unreacted-1223 superconducting pellets [101]. Unreacted-1223 pellets were also prepared and explored to create a thallium atmosphere and lock the thallium in the Tl-1223 phase. Unreacted pellets are prepared with the same synthesis techniques that are mentioned in the previous chapter. So, to prepare the unreacted pellets, 2 grams of milled powder from the glove box was taken out safely; this powder was already calcinated two times and milled for 60 hours after adding Bi_2O_3 and PbO.

Table 3.7. Amount of the elements to prepare Tl-1223 powder (2g) for thallination

Element	Weight (g)
Tl	0.519
Bi	0.151828
Pb	0.150535
Sr	0.509261
Ba	0.199541
Ca	0.276616
Cu	0.692511

Moreover, 0.52-gram Thallium powder was added to it to create proper stoichiometry for forming the Tl-1223 phase. Once the powder was prepared, unreacted-1223 pellets of different sizes and weights were prepared to help the growth of the preferred phase. An optimised electrolyte was prepared. Several thin-film precursors were deposited on the silver substrates (40 µm) at pulse potential and treated with unreacted-1223 pellets placing them on the top and tightly packed in the gold capsule. Some of the films are shown in table 3.8, and One of the most interesting things is that all the thin film samples treated at high temperatures were well covered, and a dark spot can be seen in figure 3.23.

Table 3.8. Effect of Temperature, Time and Thallium Source on Synthesis of 1223 Phase

Sample no.	Treatment temperature(°C)	Treatment time (min)	Thallination unreacted-1223 source	Phase (maximum to minimum order)
1.	885	40	A half piece of 2 cm pellet of 0.312 g	1223,1212, oxides
2.	890	50	A pellet of 2 cm diameter of 0.625 g	1212, 1223, OXIDES
3.	890	50	A previously reacted 2 cm diameter of 0.625 g	1201, oxides
4.	890	50	A half piece of 2 cm pellet of 0.312 g	1223,1212, oxides
5.	890	40	A half-reacted pellet 0.312 g	1212, oxides
6.	890	40	A half-reacted pellet 0.312 g	1201, 1212,

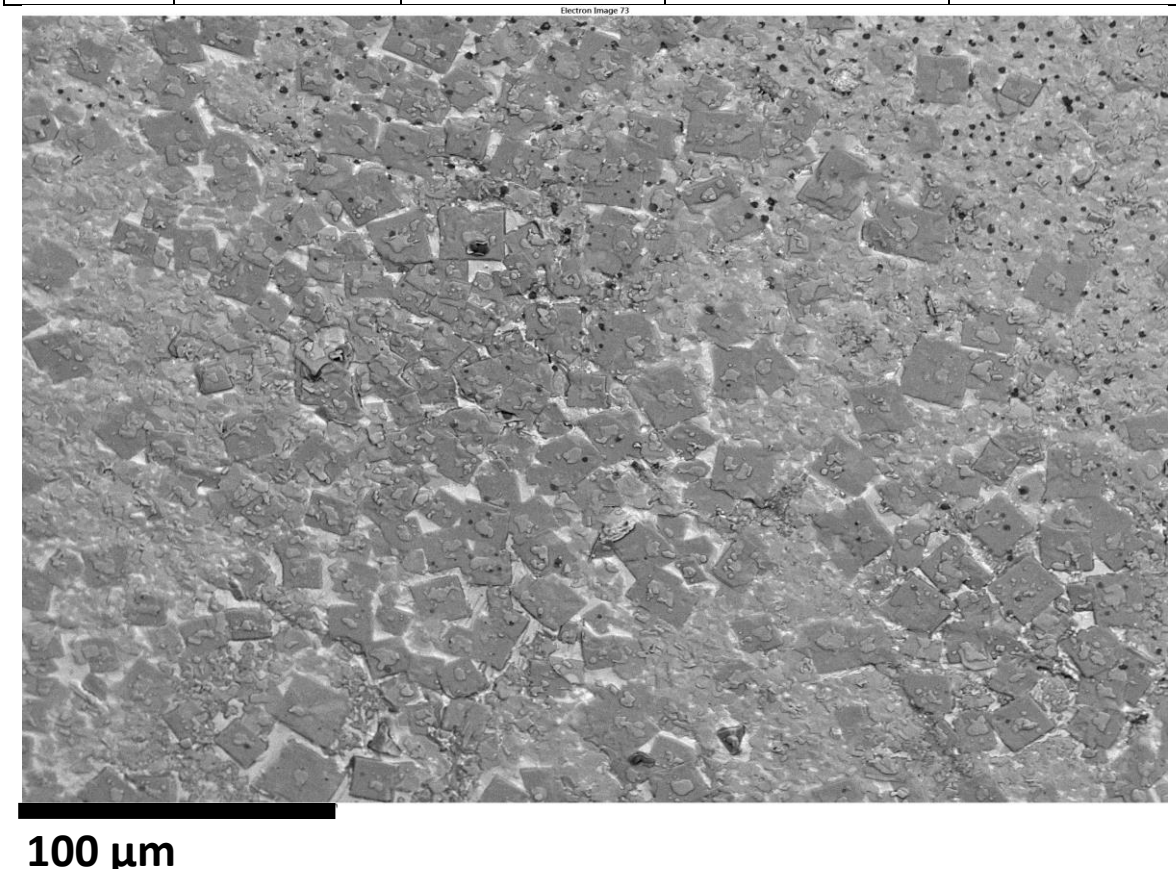

Figure 3.23. SEM image of well-covered post annealed Tl based thin film annealed with an unreacted-1223 pellet

It can be evaluated from the table that the films treated with a half (0.625 g powder was pelletised into a 2 cm circular pellet and a half piece was used) pellet of 0.312 g are more favourable to grow Tl-1223 in the majority, but a complete pellet more favourable towards Tl-12121. However, reacting with even once reacted pellet are bent to produce 1212 or 1202 phase.

Furthermore, the choice of unreacted pellet provides better coverage of the superconducting grains on the substrate and the phase formation.

3.3 Conclusions

This chapter discusses advances in thallium-based thin-film coatings. Electrocoating has been applied because of its speed, simplicity, and affordability to produce highly reactive thin-film precursors.

The electrolyte was adjusted to achieve appropriate stoichiometry (Tl, Pb, Bi: Sr, Ba: Ca: Cu-1:2:2:3) on the substrate. Still, firstly the deposition of all elements dissolved in DMSO was tested by cyclic voltammetry. Moreover, potential pulse deposition seems to improve the homogeneity, thickness and material composition compared to continuous pulsed deposition.

Cool rolled Silver has been the main choice for deposition of the superconducting thin films as conductive substrates. And, the proper amount of thallination source for annealing the precursors is another primary consideration. It is found that the amount of 3.7 mg Tl_2O_3 used for thallination of the precursor with a thickness of 3 µm and a diameter of 8 mm improves the Tl-1223 phase formation and the development of grains covering the surface of the substrate.

Chapter 4: Microstructural study and magnetic and transport characterisation of thallium-based superconductors

4.1 Introduction

Thallium-based superconductors, furthermore, require an understanding at the microstructure level as a foreseen material for the beam screen of particle accelerator. This chapter covers the microstructural and transport characterisations, including Scanning electron microscopy (SEM), transmission electron microscope (TEM), Scanning Hall Probe Microscope (SHPM), and X-ray photoelectron spectroscopy (XPS) for the surface analysis of the post annealed thallium based bulk samples (detailed in Chapter 2) and thin-film superconductors (detailed in Chapter 3).

4.2 Scanning Electron Microscope (SEM) analysis of thallium-based superconducting thin film

In this chapter, SEM measurements were performed on FEI Quanta 250 FEG-SEM microscope using Everhart- Thornley detector for secondary electrons in high vacuum at USTEM, TU in Vienna. Moreover, the system also provides energy dispersive X-ray analysis (EDX) with a Si_3N_4 window.

High contrast and resolution SEM investigation was performed on electrochemically deposited thallium based thin films to analyse the morphology, phase formation, alignment of the grains, and impurities.

The SEM image shown in figure 4.1 is a grain formed deposited with the typical electrodeposition method described in Chapter 3. In the final annealing process, 10 mg of Tl_2O_3 was used as the thallination source.

Figure 4.2 represents an SEM micrograph of the larger area of the superconducting thin film. The square-shaped superconducting grains are grown, but the silver grains' visibility proves the insufficient coverage of the substrate by the superconducting material. Anyhow, using thallium oxide powder as a thallination source is a successful approach for forming the 1223-grain. Furthermore, isolated but big grains (larger than 50 µm) and the presence of non-stoichiometric materials can also be seen in figure.

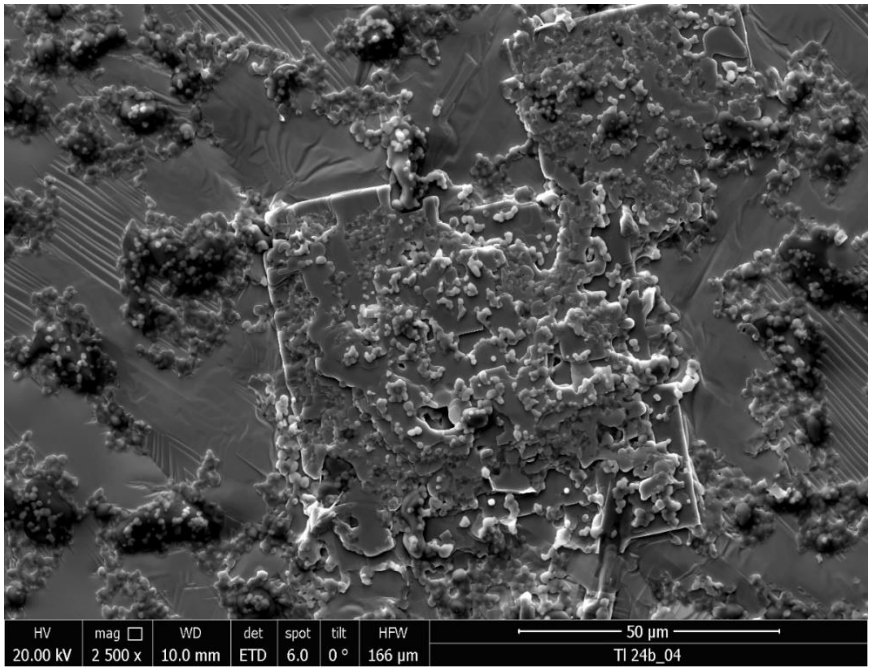

Figure 4.1. A high-resolution SEM image of a large square superconducting Tl, Pb, Bi-1223 grain surrounded and covered by other phases and impurities

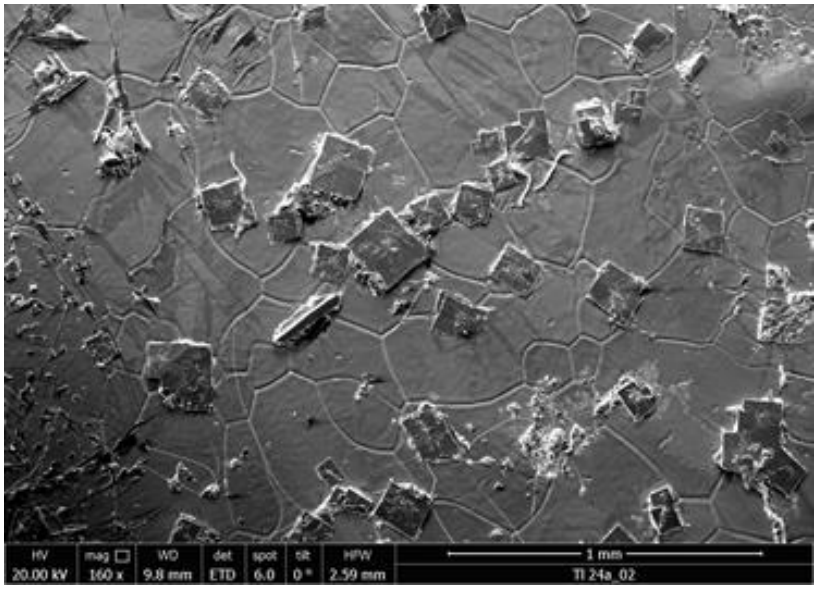

Figure 4.2. The SEM micrograph of a thin film deposited on the silver substrates shows the growth of distant superconducting grains deposited

Energy-dispersive X-ray spectroscopy (EDX) was further utilised to the thin film to locate the formation of the superconducting phase and impurities after the SEM revelation of Interestingly

formed square grains (figures 4.3 a, b). Different colours, which can be seen clearly in figure 4.3b, link to the different superconducting phases and impurities. The blue indicates the uncovered silver substrate; light green and yellow correspond to the Ca, Sr and O rich impurities. The bottom red colour corresponds to the most favourable Tl-1223 phase, but on the top of it, green coloured layer, the Tl-1212 phase grows. Thus, Tl-1223 grows more preferably on the silver, but the Tl-1212 phase grows on top.Thus, Tl-1223 grows more preferably on the silver, but the Tl-1212 phase grows on top.Thus, Tl-1223 starts growing preferably on the silver, but the Tl-1212 phase grows on top.Thus, Tl-1223 grows more preferably on the silver, but the Tl-1212 phase grows on top.

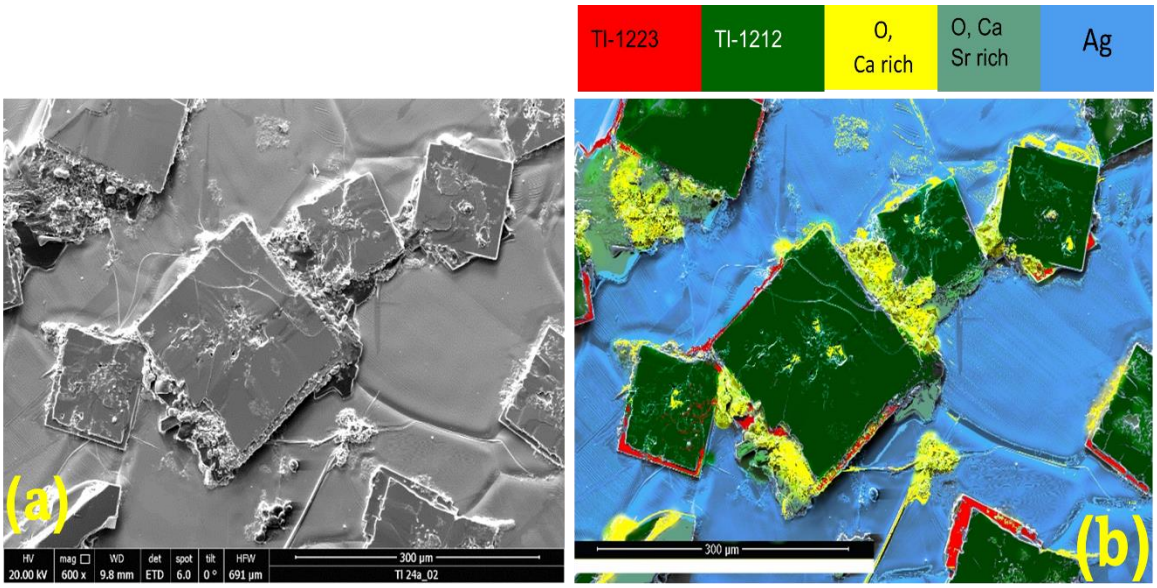

Figure 4.3. EDX analysis on the grains to distinguish the layer and non-stoichiometric formation of the superconducting grains

To maximise the substrate coverage with the thin film and enhance the growth of the Tl-1223 phase is one of the primary considerations in this research. So, the other film with almost the same parameters, as above, was prepared on an Ag substrate. The only amount of Tl_2O_3 was reduced to 8 mg from 10 mg.

The SEM image of the film treated with a reduced thallination source is illustrated in figure 4.4. The slight difference in the source has improved the coverage to a perceptible level. EDX analysis was employed to detect the formation of phases or impurities, and the results are shown in figure 4.5. The improved growth of the Tl-1223 phase grains (signalled with green colour) and suppression of the Tl-1212 phase and impurities (signalled with blue and yellow colours) can be seen. Moreover, the size of the grown grains is still significant (50-100 µm).

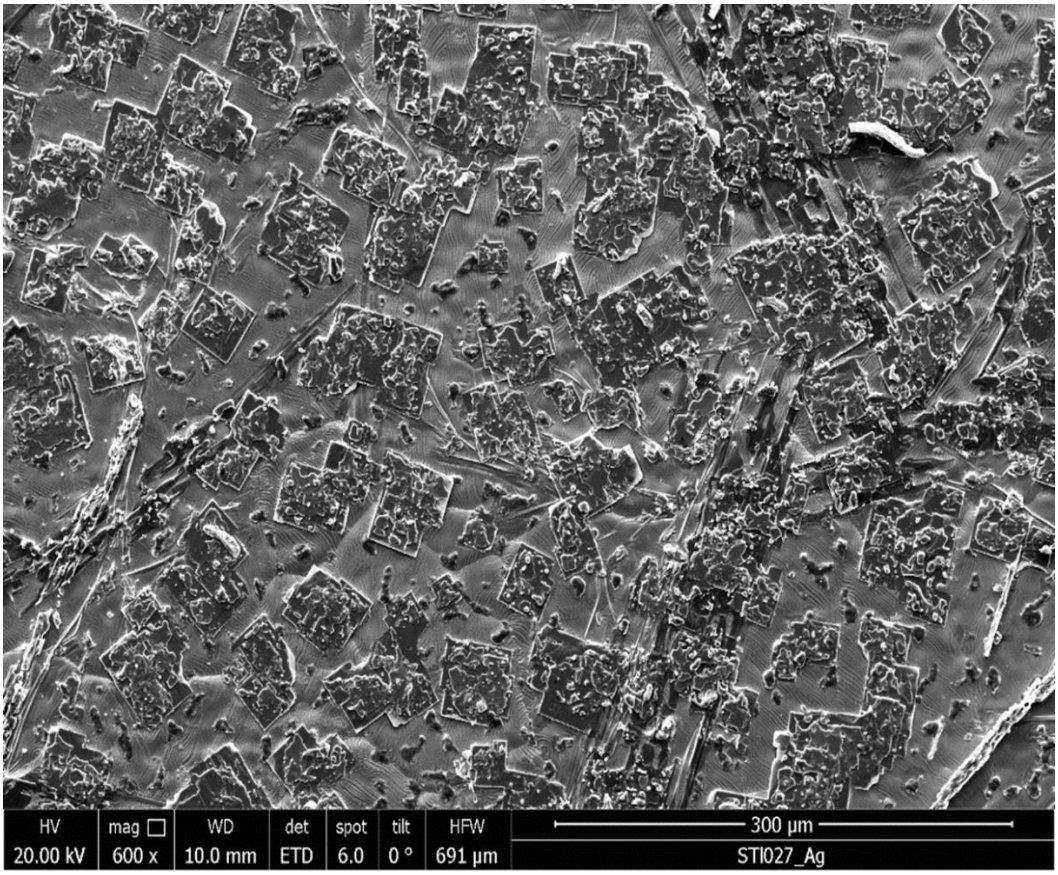

Figure 4.4. The SEM image of thin-film shows well-oriented growth of grain s on the silver substrate

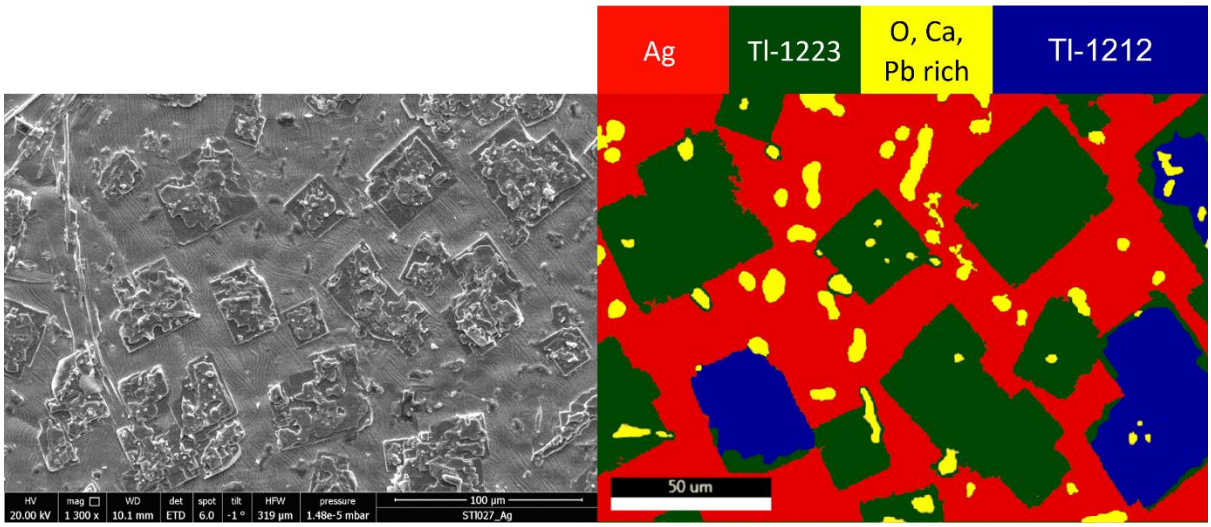

Figure 4.5. SEM and EDX analysis of the Tl-1223 formulated thin

A qualitative study counting X-rays peak intensities, EDX and coverage analysis of the most detected phases has been done in function of the thallium powder used in the high-temperature reaction (fig 4.6). The figure depicts the improvement in the Tl-1223 phase with reducing the thallium powder amount.

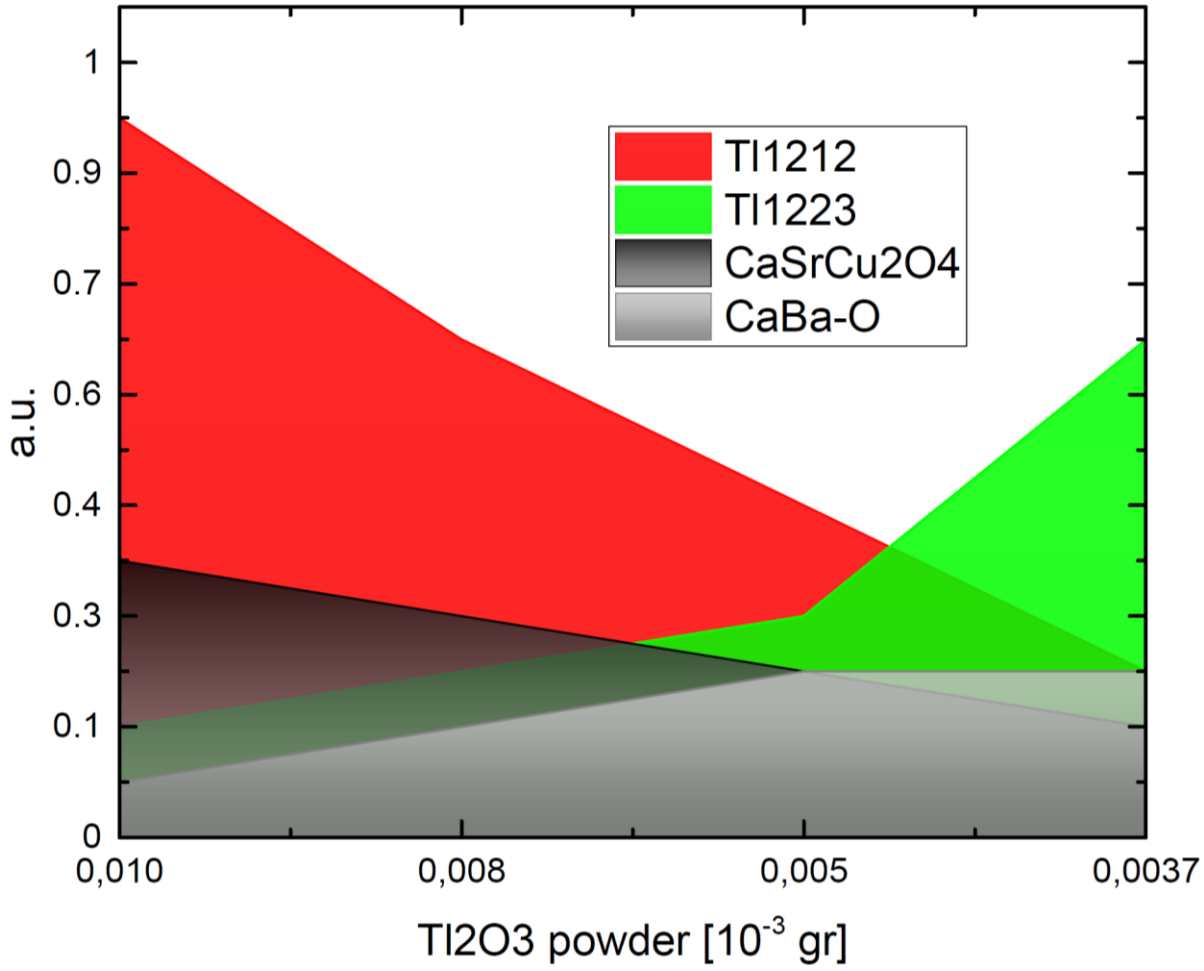

Figure 4.6. A qualitative analysis of X-rays, EDX, and coverage performed on thallium thin films thin

Reducing thallinating Tl-oxide powder to better form the Tl-1223 phase and less desired Tl-1212 is challenging to realise since the control of less than 3-3.5 mg inside the capsule for the reaction is very tricky and challenging to reproduce with reliability.

4.3 Transmission Electron Microscopy (TEM) analysis of thallium-based superconducting thin film

Transmission electron microscopy (TEM), also known as conventional transmission electron microscopy, typically uses a beam-column 2.5 meters high with a 30 cm diameter and can achieve a 2 Å resolution. In a TEM system, an electron beam passes and interacts through a sample to form an image. Furthermore, the imaged can be amplified using imaging devices, such as a fluorescent screen, a photographic film layer, or a sensor, such as a charged coupled device (CCD) camera. This technique examines the surface structures, morphologies, surface defects, crystalline atom structure, crystalline size, and sample

composition. For thallium based high-temperature superconductor, TEM measurement was performed on FEI TECNAI F20 microscope at USTEM, TU in Vienna (fig 4.7).

Figure 4.7. Transmission electron microscope (TEM) system (source USTEM-TU)

4.3.1 Focused ion beam (FIB)

In comparison to SEM, the electron column of TEM does not offer much space for the sample[102], [103]. So, the sample should be thin enough for electrons to penetrate and form an image. The Focused ion beam (FIB) is commonly employed to prepare very thin samples (100 nanometres or even small samples) for the TEM. To cut the tiny sample from the thallium superconducting film for the Quanta 200 3D DualBeam-FIB with Gallium (Ga) liquid metal ion source was used.

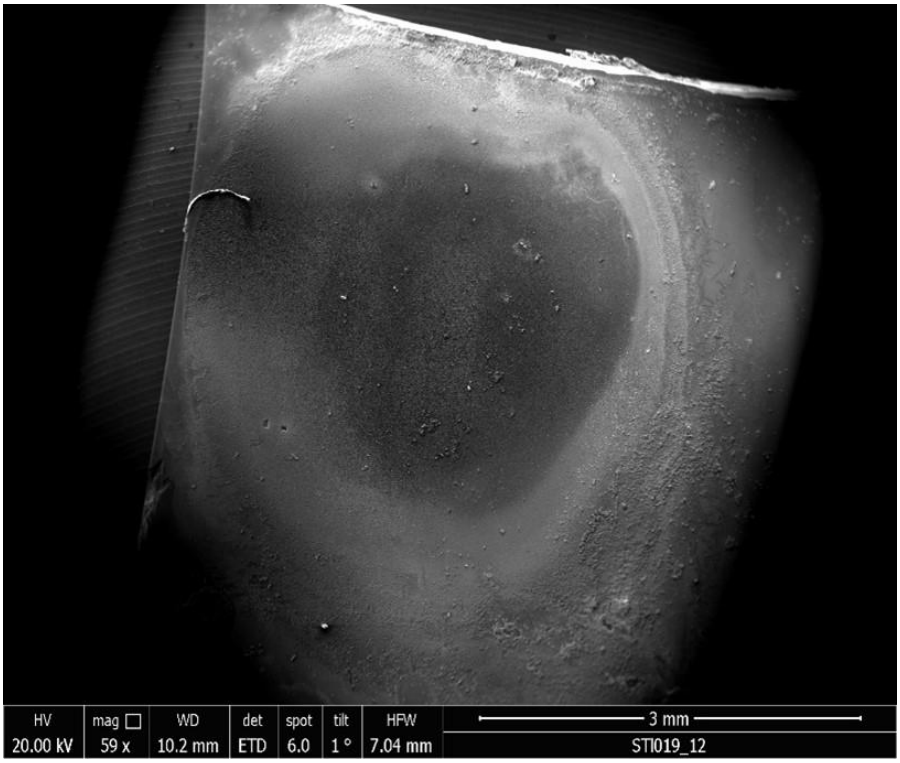

Figure 4.8. An image of the film to cut out the lamella using the focus ion beam (FIB)

An area of the thallium film (fig. 4.8), deposited on the Ag, represented the desired morphology to prepare the lamella. Next, the gallium ion beam was used to carve a square of matrix material on three sides with an aimed depth to get an isolated rectangular material, identified as the lamella. Only a side remained attached to the sample by two corners. And then, the Easy-Lift needle was brought down to one side of the lamella and connected to the lamella with platinum. Then gallium ions were again used to cut off the last attachment from the sample, which allowed the needle to move with the lamella attached (Fig. 4.9).

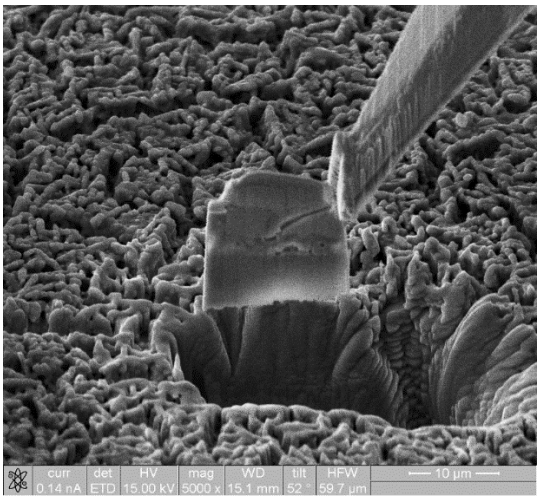

Figure 4.9. A lamella attached to the needle is being lift-out for TEM investigations of thallium based thin film

The needle was brought into contact with the TEM grid, and lamella was then welded to the TEM grid using a platinum cap. Finally, the Ga ion source was used to detach the lamella from the needle (Fig. 4.10). The obtained lamella is then removed from the FIB and brought to the TEM instrument for further analysis.

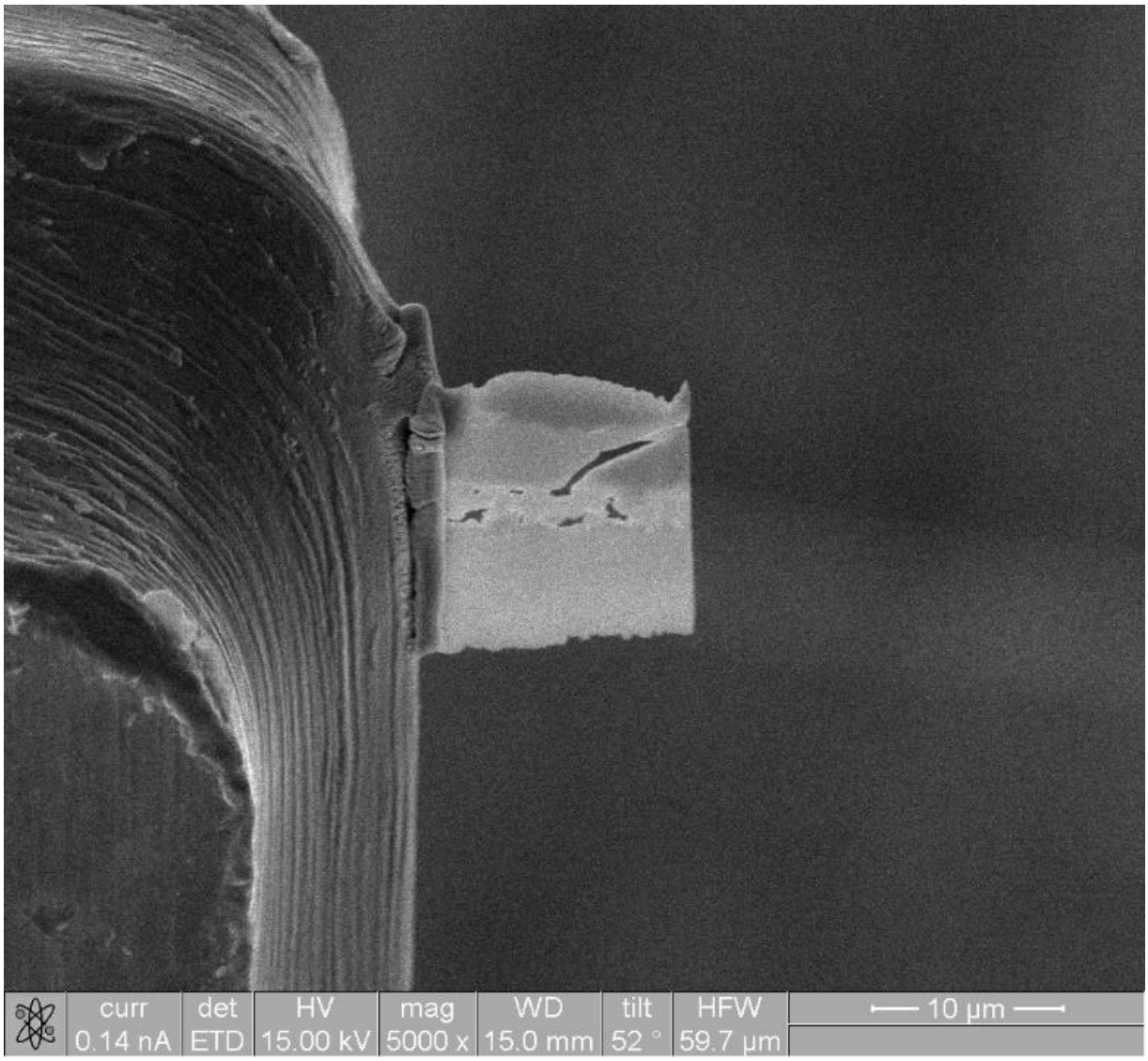

Figure 4.10. FIB-Lamella attached to the side of the TEM grid

The TEM grid was placed inside the system for thallium lamella analysis (Fig. 4.11). EDX (Fig. 4.11) obtained on this sample shows the element-rich sites and confirms the presence of electrochemically deposited sites elements.

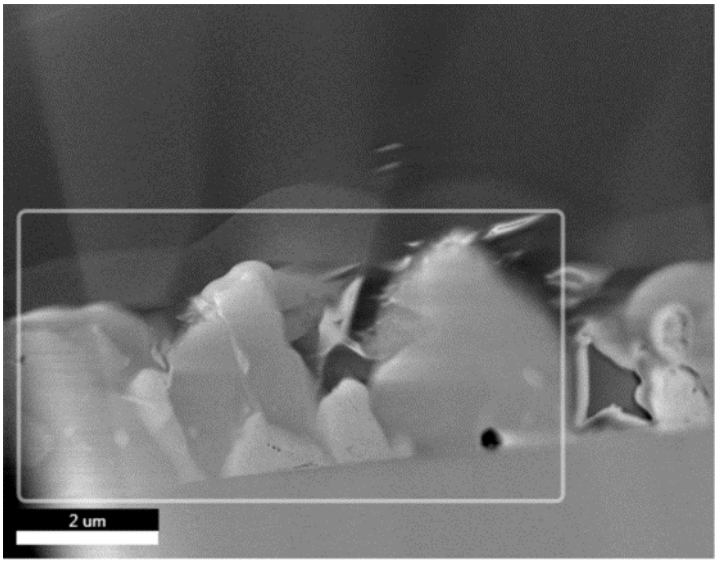

Figure 4.11. TEM analysis image of thallium FIB-lamella

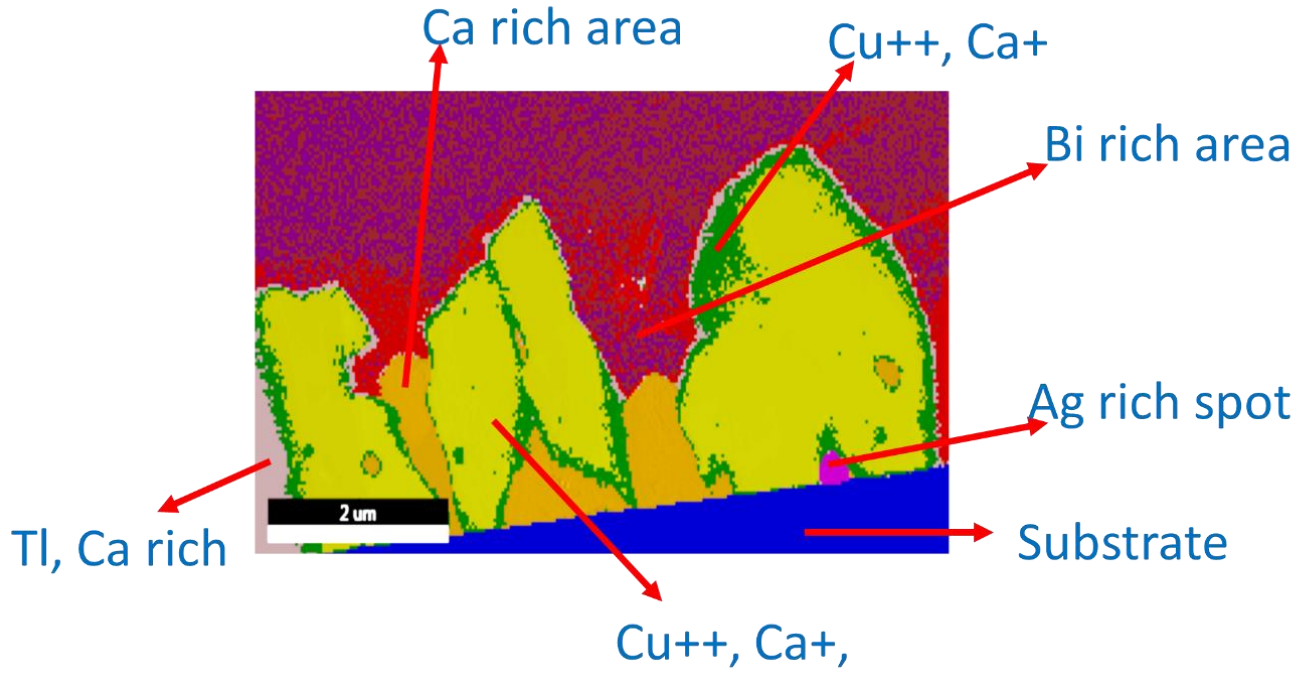

Figure 4.12. EDX-TEM analysis on the thallium lamella does not indicate the phase formation, but the existence of all electrolyte deposited elements

4.4 Scanning Hall Probe Microscopy (SHPM)

A variety of systems have been developed to examine the surface magnetic structure of materials, including magneto-optical imaging [104], scanning superconductivity quantum interference device (SQUID)[105] and magnetic force microscopy (MFM) [106], and recently, the scanning Hall probe microscope (SHPM) [107]–[110].

This technique was first developed by Chang et al.[107], Furthermore, this non-invasive technique (as the non-magnetic probe does not disturb the sample) offers high spatial resolution and a direct method for magnetic field imaging under variable magnetic field and temperature parameters. In SHPM, a Hall probe is used to measure local magnetic properties and is considered the central part of the microscope. Hall probes are based on the principle of the Hall Effect, discovered by Edwin Hall in 1879, which states the appearance of a transverse voltage (the Hall voltage V_{xy}) if a current-carrying conductor is placed in a perpendicular magnetic field.

SQUID magnetometry and Scanning Hall Probe Microscopy (SHPM) was used to characterise superconducting thallium based bulk and thin films deposited on Ag and single-crystal $SrTiO_3$ substrates. AC susceptibility measurements in a SQUID magnetometer were used to calculate the superconducting transition temperature (MPMS, Quantum Design). The measurement was performed on the bulk sample (figure 4.13), with the expectation of high T_c for the Tl-1223 phase, and the measurement shows $T_{c,\ onset}$ = 114 K

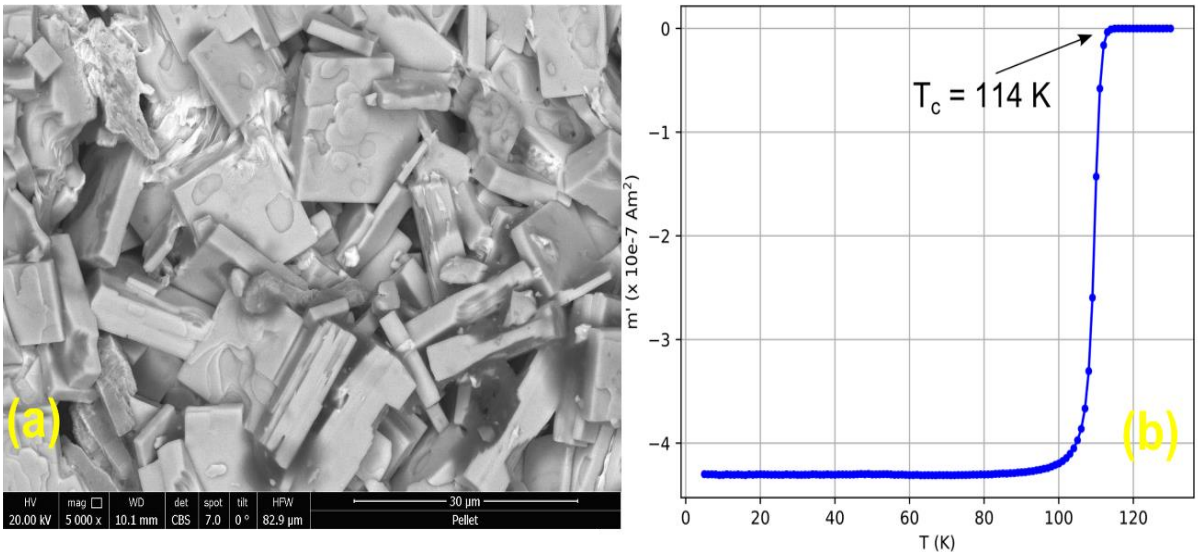

Figure 4.13. The SEM image (a) and the AC susceptibility performed on the Tl-1223 bulk pellet and $T_{c,\ onset}$ is 114 K

The remnant field profile of the superconducting bulk sample (Fig. 4.14) was imaged using a Hall scanner in an 8 Tesla cryostat apparatus with micrometre resolution was used.

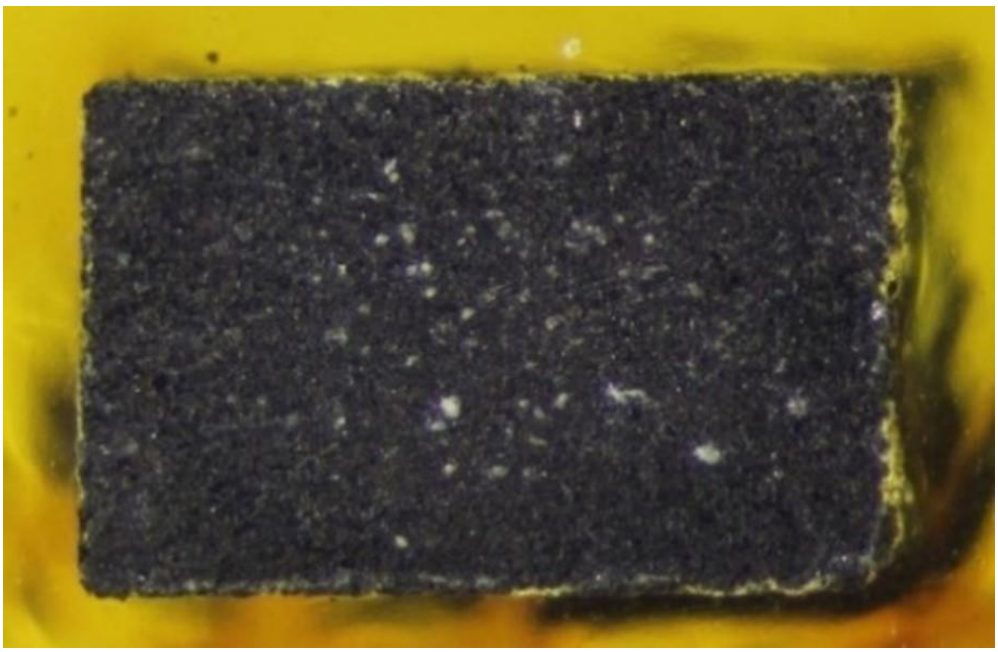

Figure 4.14. A rectangular piece of superconducting thallium bulk sample with Tc,onset=114 K

The piece of the bulk sample was cooled down up to 5 K and then magnetised. The field profile in figure 4.15 shows the well-connected grains

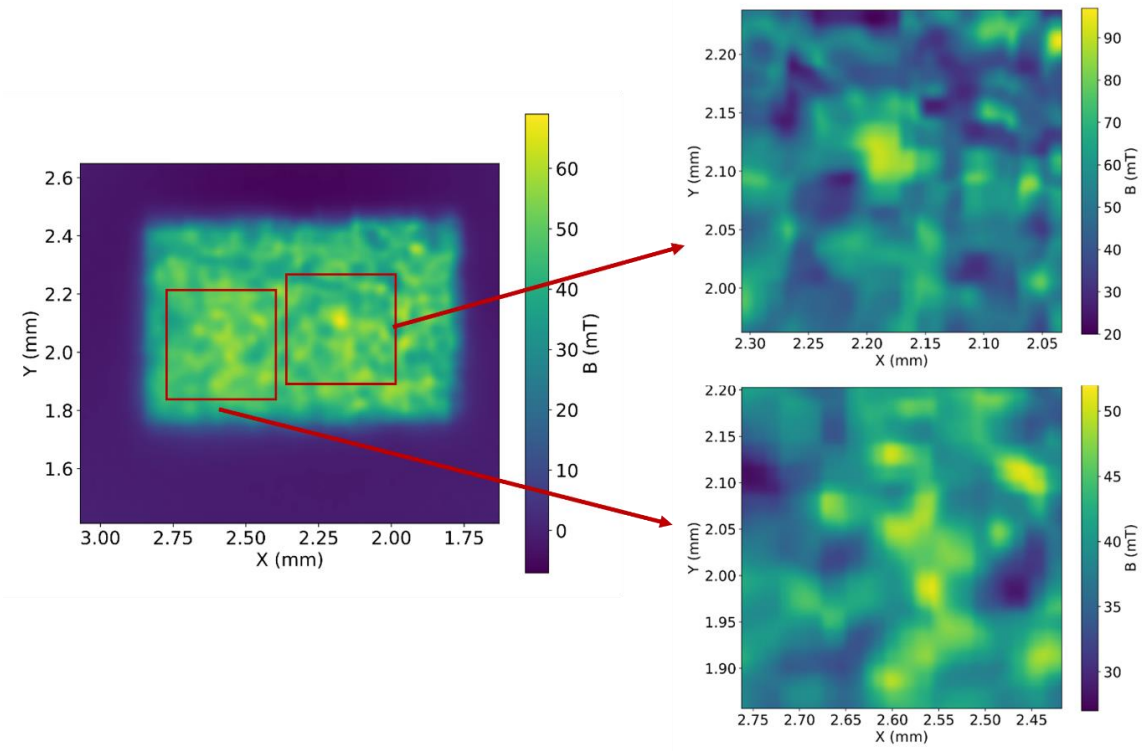

Figure 4.15. The trapped field in the grains of the bulk sample

Electrochemically deposited thin films on substrates were analysed utilising SQUID and SHPM. AC susceptibility measurements calculated the superconducting transition. The measurement performed on a thin film (Fig. 4.16 a) shows two transitions. The first, with $T_{c,\text{the onset}}$ of 107 K, is recognised to the Tl-1223 phase, whereas the second transition with $T_{c,\text{onset}}$ = 75 K, the Tl-1212 phase (Fig. 4.16 b).

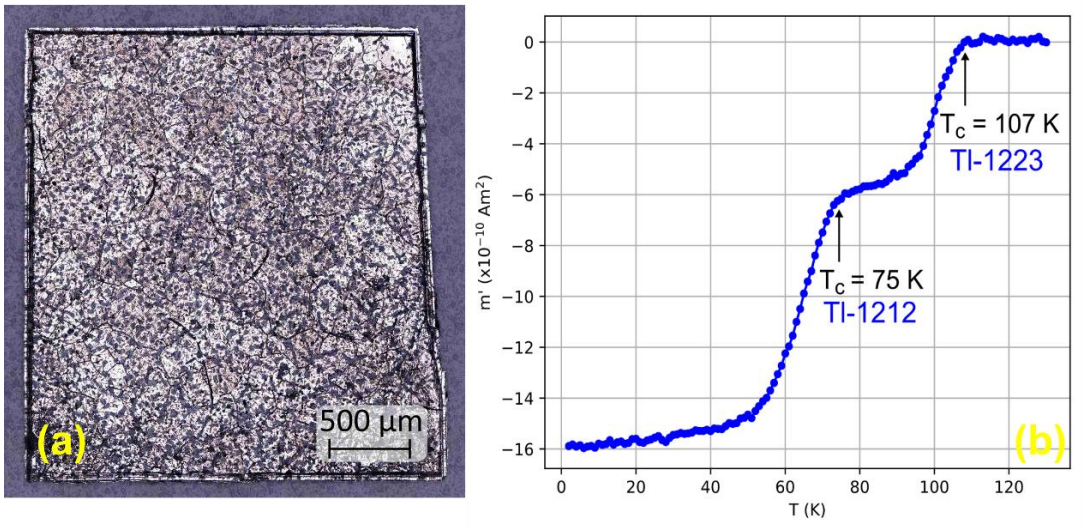

Figure 4.16. (a)AC susceptibility of thin film on Ag substrate. (b)Two transitions can be observed at approximately 107 K and 75 K, corresponding to the Tl-1223 and Tl-1212 phases.

All except a circular patch of the superconducting thin layer was etched off the silver substrate with hydrochloric acid to fit the SHPM configuration. This circular patch of grains is shown in fig. 4.17a, acquired using a digital microscope (Keyence VHX-6000). For the measurements, the circular portion of the thin film was cooled down to 5 K and then magnetised with 1.5 T, and the area scan, indicated by bright neon colour (b), showed many separate and clusters of grains with high trapped fields. The optical picture and magnetic field map may be readily compared, and comparing the two images reveals that they are in perfect agreement, seen in fig. 4.17c. High-resolution scanning of a smaller area was done to acquire a clearer sense of the currents within the individual grain and across grain borders—the trapped field of a few clusters, which equates to 60 mT, fig. 4.17d. The spatial distribution of J_c can be derived from the obtained trapped field by inverting Biot-law Savart's [111]. For the measured clusters, the white arrows in fig. 4.17e.

Depict the direction of current flow in grains and across grain boundaries. For example, at 5 K, the critical current density in these grain clusters has an average value of $J_c = 8 \times 10^{10}$ Am^{-2}.

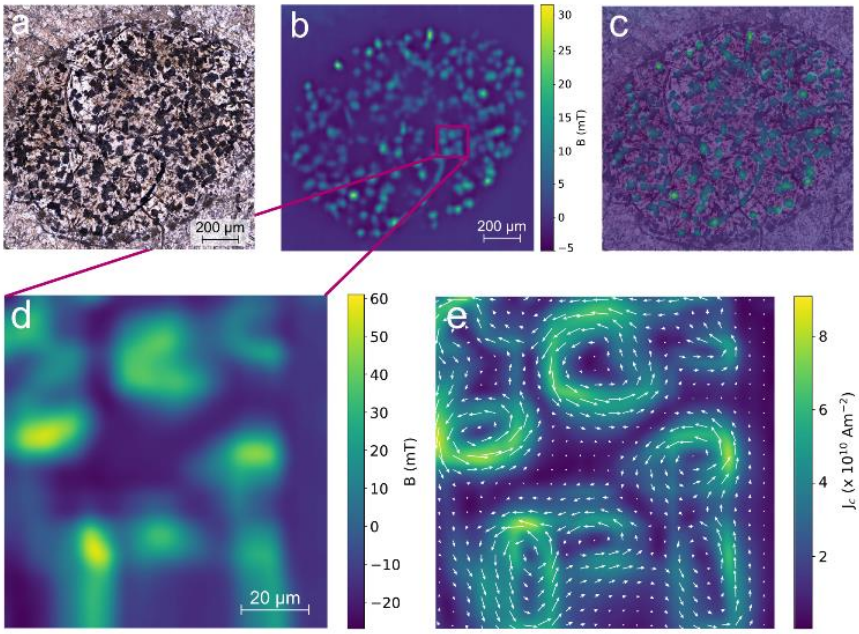

Figure 4.17. Image of superconducting grains in the circular patch on Ag substrate (a), and corresponding scan of the trapped field (b). An overlap of both images (c) shows perfect agreement between the optical image and the magnetic measurement, a high-resolution scan of a smaller area (d) and corresponding critical current density distribution (e).

Above mentioned investigations were also carried out on superconducting thin film deposited on STO substrate with a thin coating. Figure 4.18a shows a larger cluster's trapped field. At 5 K, the trapped field reaches 100 mT. Thus, the J_c distribution is calculated on a greater area than on the Ag substrate, as seen in figure 4.18b.

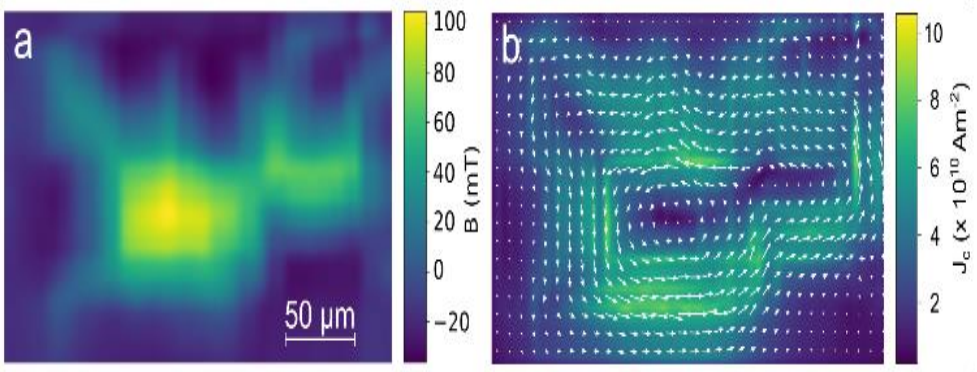

Figure 4.18. The trapped field in grain cluster of thin film on $SrTiO_3$ substrate (a) and (b) corresponding critical current density distribution.

SEM and TEM imaging were used to further explore the thin film's microstructure on the single crystal STO substrate. The places with the highest trapped fields can be determined by precisely comparing SEM pictures with magnetic maps. The overlay of a magnetic map and an SEM picture for such an area is illustrated in fig. 4.19a. This sample generated two TEM lamellae using a Focused Ion Beam (FEI Quanta 200 3D DB -FIB), one from an area with a high trapped field and another from an area without a trapped field indicated by the arrows in Fig. 4.19a and 4.19b.

A protective platinum layer is placed on the sample surface, the lamella is cut off, and the lamella's thickness is decreased to roughly 100 nm in this procedure. The figure shows that the TEM image shows a big grain thickness of 1.8 µm flat on the substrate surface in the high trapping field region. 4.19c. The following locations can be identified using EDX analysis: The Pt protective layer is on top, followed by a thin layer of SiO resulting from minor manufacturing imperfections. Finally, a big Tl-1223 grain on the STO substrate. As demonstrated in fig. 4.19d, the lamella extracted from the region without trapped field has the same composition. However, several Tl-1223 grains were found randomly aligned on the substrate surface in this situation. The misorientation of the Tl-1223 grains blocks current flow, emphasising the importance of grain orientation.

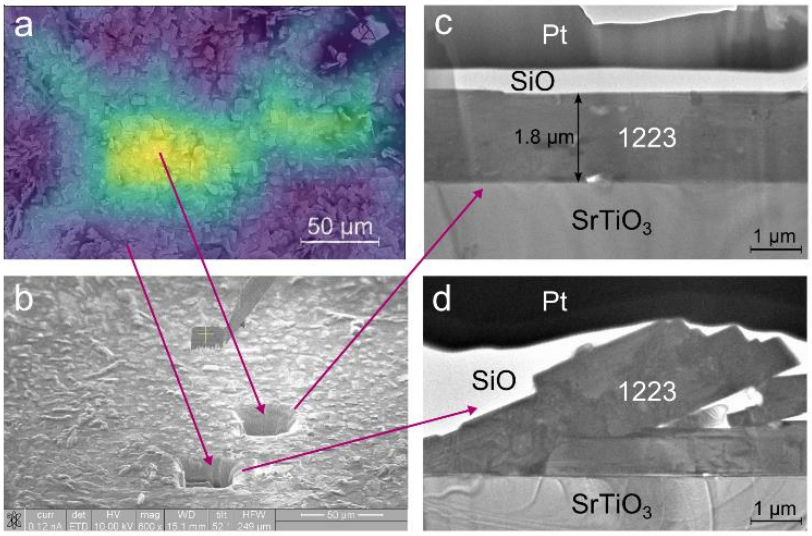

Figure 4.19. Overlay of trapped field and SEM image of a thin film on STO substrate (a), and preparation of two TEM lamellas with a Focused Ion Beam (b). TEM images of areas with high trapped field (c) and no trapped field (d) show the desired Tl-1223 phase with decent and bad grain alignment, respectively.

4.5 X-ray Photoemission Spectroscopy on thallium based bulk sample

XPS is also performed on a bare thallium-1223 pellet to investigate the chemical composition of a square bulk sample. In thallium superconductors, the main photoemission

peaks relate to Tl-4f, Bi Ca-2p, Ba-3d5, Ba-3d5, Ba-4d5, Cu-2p3, O-1s, C-1s, and Sr 3d. The complete energy spectrum at room temperature with Al Kα radiation is shown in Figure 4.20,

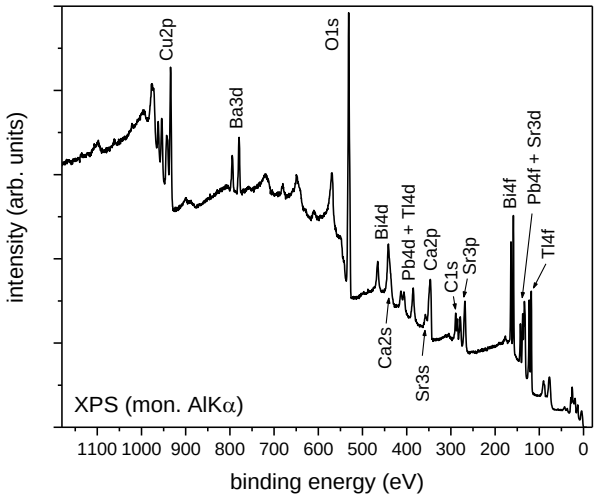

Figure 4.20. XPS performed on a thallium based superconducting bulk sample, and it validates the existence of all elements

Moreover, the composition of the XPS analysis is entered in table 4.1

Table 4.1. Atomic per cent of elements found on thallium-1223 superconducting samples using XPS

Element	**Tl**	**Pb**	**Bi**	**Sr**	**Ba**	**Ca**	**Cu**	**C**	**O**
At. %	2.5	1.1	2.6	7.4	1.2	9	9.9	15.5	50.6

It has more oxygen and less thallium; after high-temperature annealing of the sample, the thallium concentration decreases from the surface.

Tl-4f level:

Figure 4.21 shows the Tl-4f XPS spectrum of the sample. The binding energy of the Tl-$4f_{7/2}$ is around 118.2eV.

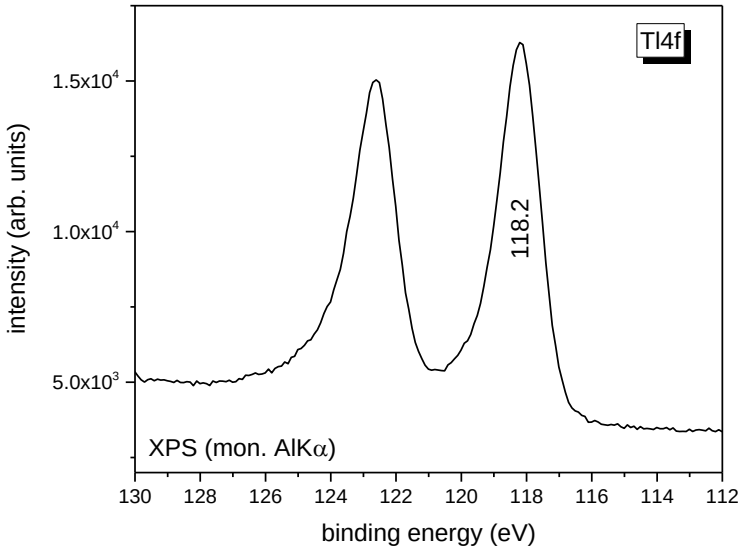

Figure 4.21. XPS Al Kα Tl-4f spectra of the bulk sample.

Bi-4f level:

The spit orbit split spectrum of the Bi-4f electrons is intense and resolved for further analysis. The spectrum of the core level of Bi-4f in figure 4.22 shows an asymmetric pattern.

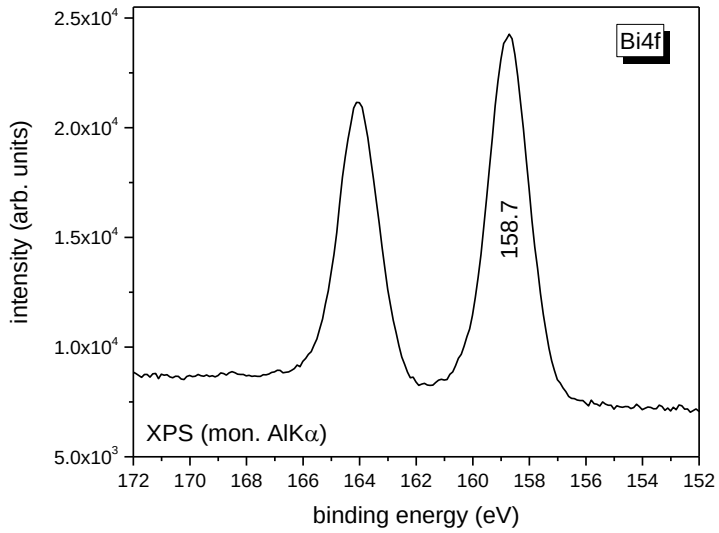

Figure 4.22. XPS Bi-4f spectrum of the bulk sample.

Cu-2p Core level:

The CuO_2 planes play an essential role in the superconductivity of the cuprate [38]. Therefore, it is vital in the study of the mechanism. The Cu- 2p3/2 level shows a peak line at

about the binding energy of 934.3 eV. Figure 4.23 shows the Cu-2p spectrum, in which there is more than one line, and literature indicates that these lines are ½ and satellite (S). The binding energy of the mainline is at 933 eV, and S is centred at about 942 eV for 2p3/2. Research shows that these binding energies are almost the same for Tl-1212, Tl-2201, and Tl-2223, indicating that most copper in superconductors is divalent.

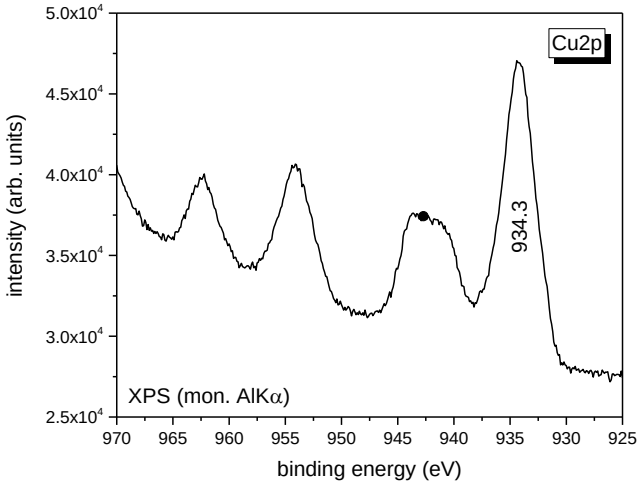

Figure 4.23. XPS Cu-2p spectra of the Tl-1223 bulk sample.

Sr-3d core level:

The Sr appears in the data. The Sr core level spectra show a mainline at about 898 eV (figure 4.24)

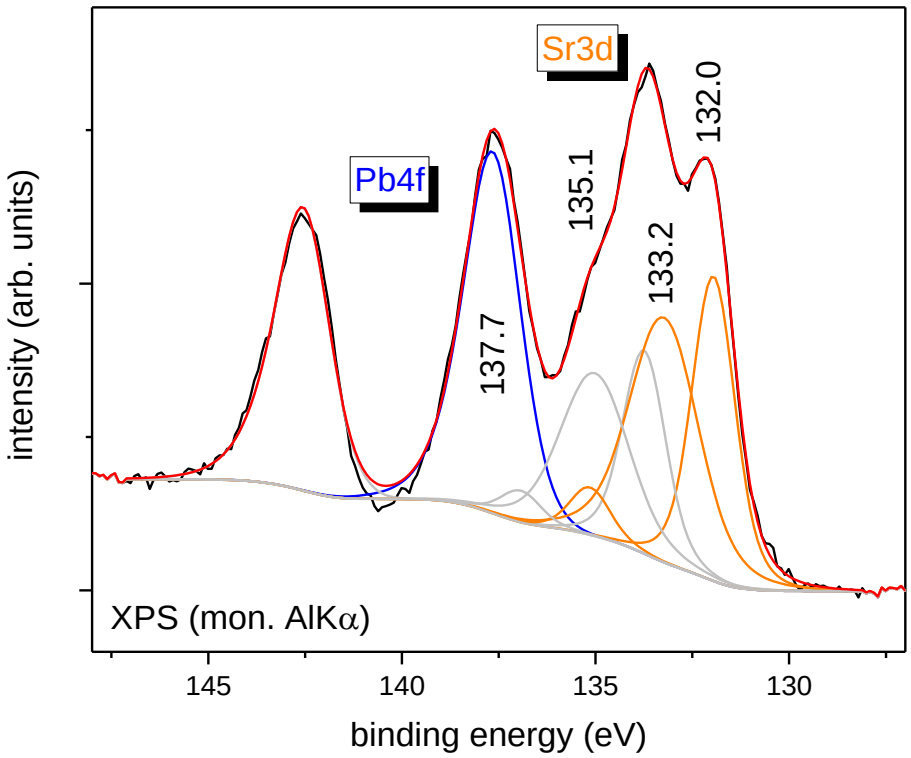

Figure 4.24. XPS Sr-3d spectra of Tl-1223 bulk sample.

O-1s core level:

The study shows that the O-1s lines are usually around 529 eV for the superconductors, and other lines around 531 eV and 533 eV are due to contaminants. For the thallium superconductor, the core level lines of O-1s are observed at about 528.7 eV. In addition, there are two lines, 531.2 eV and 533.3 eV(figure 4.25); in the O- 1s spectrum, there are signs of contaminants on the surface[112].

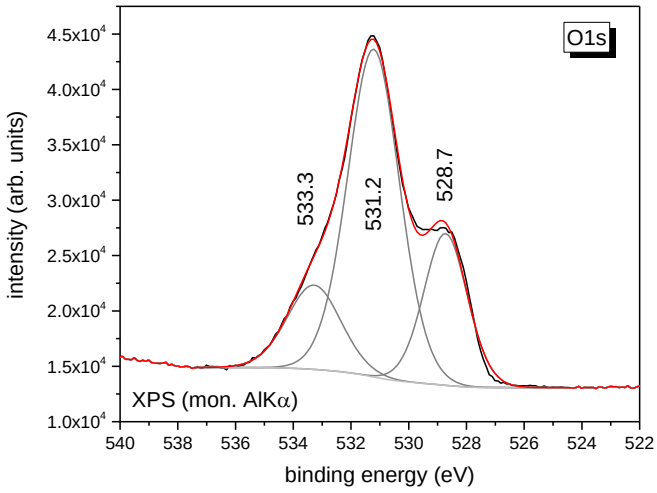

Figure 4.25. Typical XPS O-1s spectra of Tl-1223 pellet.

Ba-3d core level:

The Ba- 3d spectrum is shown in Figure 4.26 for the thallium specimen. The figure shows that the Ba-3d line has several components. Furthermore, the Ba-3d5/2 line is observed around 779.7 eV.

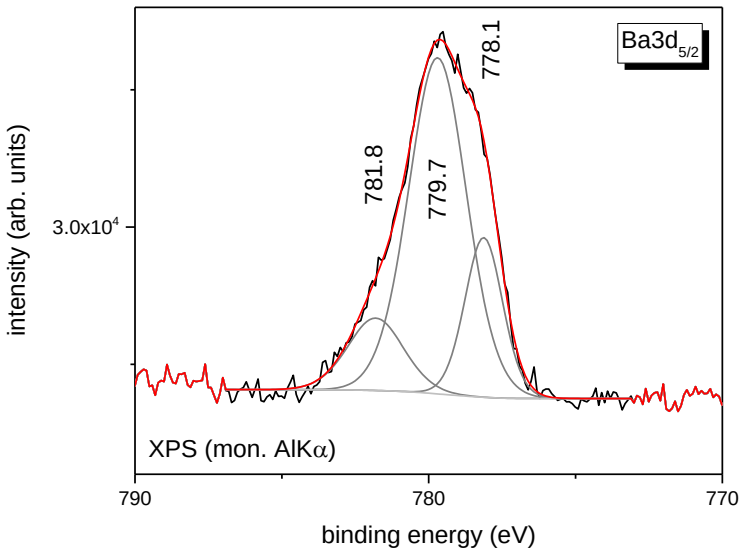

Figure 4.26. Ba-3d spectra for the a-Carbon deposited pellet.

Ca-2p core level:

Figure 4.27 shows Ca-2p spectra, and the binding energy of Ca-2p is close to 345 eV. Moreover, it can be seen that it has more than two spin-orbit pairs.

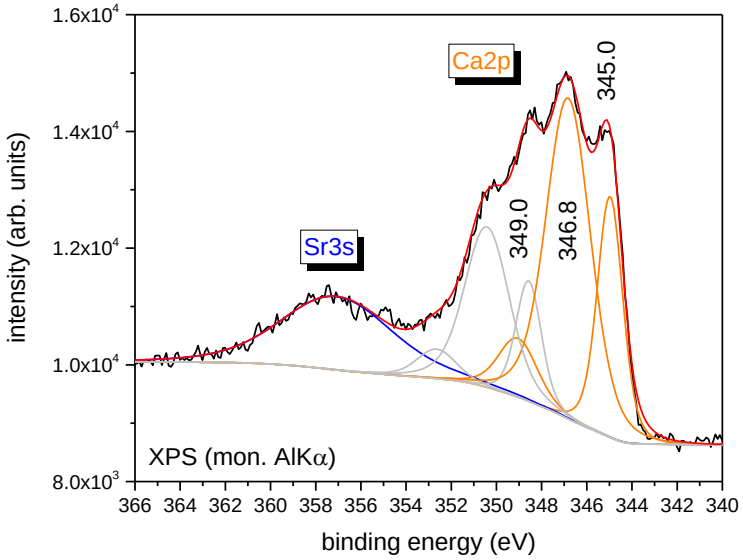

Figure 4.27. Ca-2p XPS spectra for the a-carbon deposited pellet.

The XPS analysis (so-called fingerprint of the material surface) performed on the thallium pellet confirms the existence of all the elements, including thallium. The atomic per cent of elements (table 4.1) does not make a 1:2:2:3 ratio and hence proving that exposure of the sample in the open environment leads to oxidation and contamination. The atomic per cent of elements (table 4.1) does not make a 1:2:2:3 ratio, hence proving that exposure of the sample in the open environmentenvironmentenvironmentenvironment leads to oxidation and contamination.

4.6 Preliminary High-Frequency measurements

Thallium bulk superconductors of size 1 cm^2 were fabricated by a two-step solid reaction mentioned in chapter 2 for preliminary characterisation on the surface resistance of the superconducting material in the high-frequency environment of the future circular hadron-hadron collider (FCC-hh). The measurements were done by the brass resonator non-destructive, dielectric-loaded resonator (DR) with resonant frequency ν ≈ 8 GHz based on the Hakki–Coleman geometry. The resonator is used to characterise the superconducting material at temperatures range of 5−120 K and field up to 9 T in the 25 millimetres bore of a Quantum design PPMS.

Fig. 4.28 depicts R_s of thallium based bulk superconducting sample as a function of temperature. The measurements performed on one of the primary pellets prepared clearly shows less surface resistance than copper at the FCC-hh favourable temperature range.The measurements performed on one of the primary pellets prepared shows less surface resistance than copper at the FCC-hh favourable temperature range.

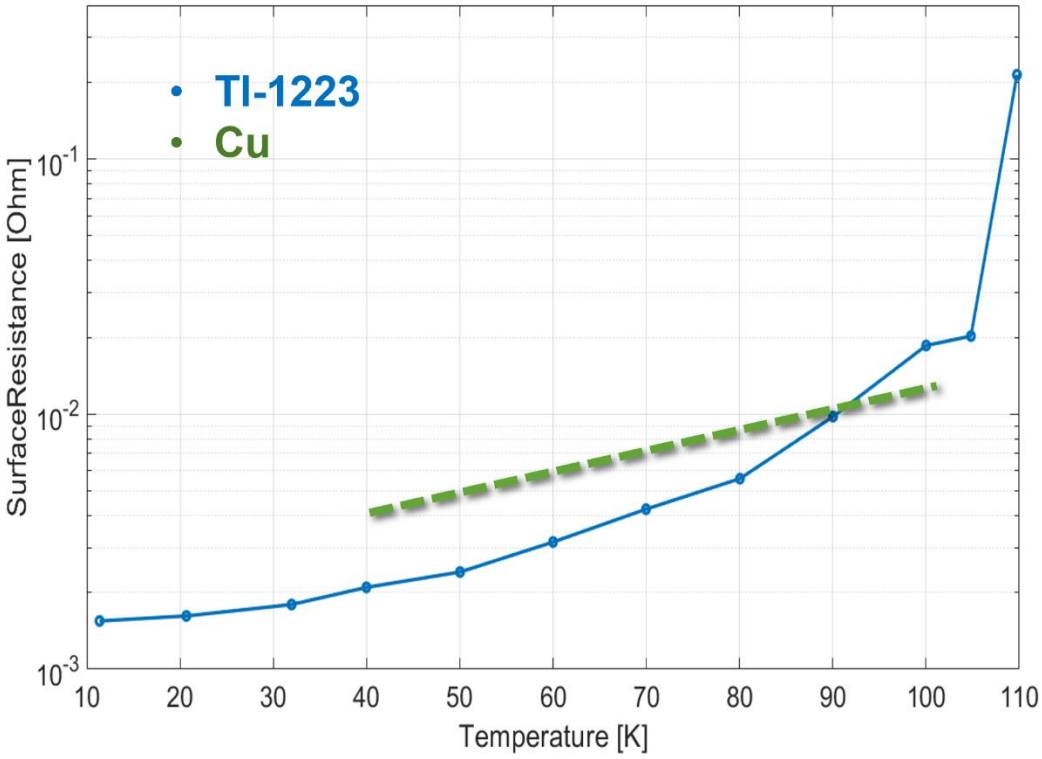

Figure 4.28. The surface resistance measured on thallium bulk pellet in high-frequency regime (8 GHz) and at different temperatures

4.7 Conclusions

This chapter includes structural analyses: Scanning electron microscopy (SEM) and transmission electron microscope (TEM) to understand the formation and composition of thallium based high-temperature superconductors. In addition, scanning Hall Probe Microscope (SHPM) was performed to map the current flow from the superconducting grains of bulk samples and thin-film superconductors. And an average value of J_c = 8 x 10^{10} Am^{-2} was calculated in the grain clusters of a thin film deposited on silver.

Since thallium is a volatile element, the thallium concentration at the sample surface decreased after treatment. X-ray photoemission was performed on the sample. It showed the electronic states of the core levels of Tl-4f, Cu-2p, O-1s, Bi-4f, Ba-3d, Sr-3d, and Ca-2p for the Tl-1223 sample. The XPS result shows some impurities as it is a very surface-sensitive technique. The result shows the composition:

Elements Tl Pb Bi Sr Ba Ca Cu C O

At. %	2.5	1.1	2.6	7.4	1.2	9	9.9	15.5	50.6

And finally, the primary surface resistance measure on a thallium bulk superconductor is lower than that of copper in an 8 GHz regime.

All the characterisations mentioned in this chapter show the progressive potential of thallium based high-temperature superconductors.

Chapter 5: Vacuum compatibility of thallium based high-temperature superconductors

5.1 Introduction

The research on thallium-based high-temperature superconductors, as already described, is also essential to understand their potential for the Future Circular Collider (FCC-hh) beam screen (BS) coatings[13]. The beam screen is the innermost part of a collider, so, besides the superconducting performances required, the choice of beam shielding material must be appropriate for ultrahigh vacuum (UHV) systems. Vacuum technology is a challenging field; it is critical from geometric design to material selection to the coating as a beam screen [16]. Therefore, proper selection of beam screen is a top priority to meet the best possible FCC-hh working parameters mentioned earlier in the first chapter.

Creating a UHV minimises the number of molecules and atoms to the smallest possible amount that would interfere with a process or experiment in an accelerator. Although reducing the overall pressure in vacuum systems is always a concern, various effects can be ascribed to the residual gas releases, such as bulk impurities, dissolved atoms, molecules that are at or diffuse to the surface, and further photoelectrons that cause outgassing and degassing of materials.

In the form of electron clouds, the accumulation of electrons from residual gases, photoemission of synchrotron radiation and secondary electron emission can lead to an increase in pressure and thus beam instability.
The number of secondary electrons emitted per incident particle is called secondary emission yield (SEY), which is preferred to be less than one for the correct operation of the accelerators. Generally, materials, especially metals, have SEY higher than one, so they need coating or other methods to reduce SEY. Coating with amorphous carbon, whose SEY is about 1[113], is considered one of the most effective ways to reduce the SEY and help any preferred material to become part of the vacuum system.

To understand the surface composition before and after SEY reduction coatings, X-ray photoelectron spectroscopy (XPS) is usually performed along with SEY measurement on the materials to be part of the vacuum system.
Thus, a material should have an acceptable outgassing rate and low SEY to fall within the vacuum acceptance criteria.

As part of the radiation shielding study, apart from being a decent superconducting material, thallium superconducting coatings must meet all the requirements to be part of a vacuum system. Since the family of thallium superconductors has never been tested for use in UHV, it is necessary to understand their vacuum behaviour.

This chapter presents the outgassing rate in the unbaked system, residual gas analysis, contamination level, SEY before and after the carbon-coated samples, and XPS measurements performed at CERN.

5.2 Vacuum acceptance analysis on thallium-based high-temperature superconductors

5.2.1 Outgassing rate

Analysis of the outgassing of materials is critical to maintaining the ultrahigh vacuum in particle accelerators. In addition, knowledge of the outgassing event is essential for the materials and treatments to achieve the required gas density in such a demanding collider [114].

Outgassing is a spontaneous discharge of gas from the materials in a vacuum, and the outgassing rate is calculated with the help of a pressure gauge and known pumping speed. The outgassing rate is defined as the quantity of gas leaving a material per unit time, denoted by Q, and the pressure P can be calculated at a point in a vacuum chamber[115] as in eq. 5.1:

$$P = Q/S_{eff} + P_0 \qquad (5.1)$$

P_0 is applied pressure, and S_{eff} is the effective pumping speed that usually varies from 1 to 1000 l s^{-1}.

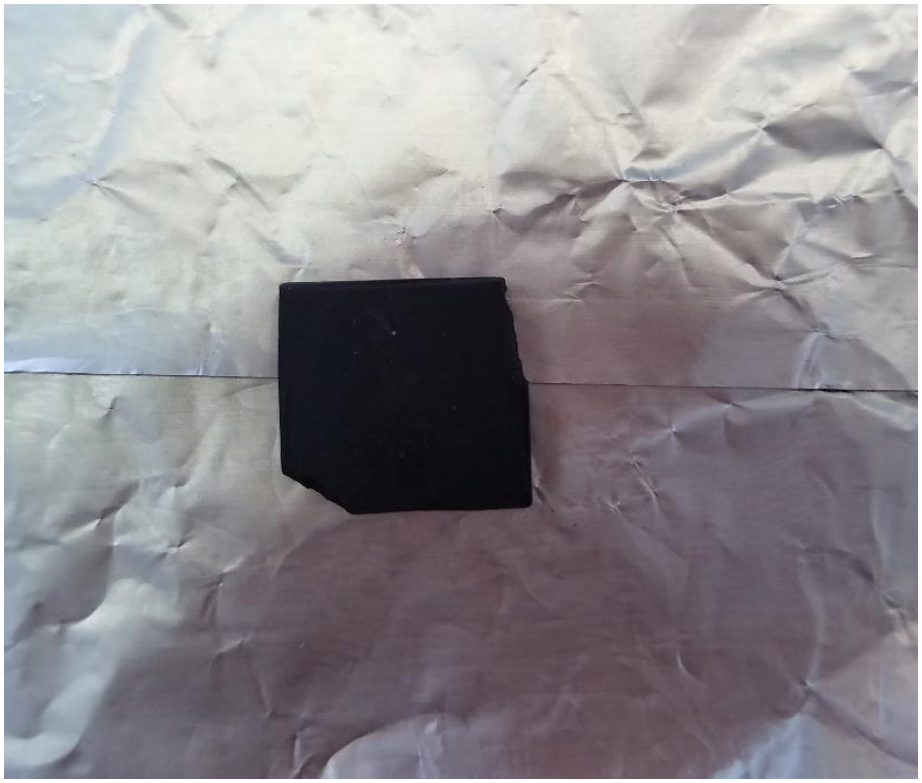

Figure 5.1. Tl-1223 bulk sample on aluminium foil before pumping down characterisations

First, to measure the outgassing rate of thallium-based superconducting bulk material (fig. 5.1), the system was evacuated for 24 h without a sample. A pressure of 10^{-9} mbar was achieved in the unbaked system. And the effective pumping speed was recorded as 9.6 l/s, 12 l/s, and 36 l/s for N_2, H_2O, and H_2, respectively. Second, after 24 h, residual gas analysis was performed to identify the gas species (Figure 5.2), where typically H_2O dominates for an unbaked system [116].

Later, a square thallium bulk sample (10×10×1.6 mm^3) with composition $Tl_{0.7}Bi_{0.4}Pb_{0.4}Sr_{1.6}Ba_{0.4}Ca_{1.9}Cu_3O_{9-\delta}$ was placed in a glass box with a piece of aluminium foil to avoid direct placement in a vacuum chamber. The chamber was pumped down with the thallium sample for one day, and later the Residual Gas Analysis (RGA) was performed to analyse any residual from the sample. Figures 5.2 and 5.3 show the pump down curve for thallium based bulk sample.

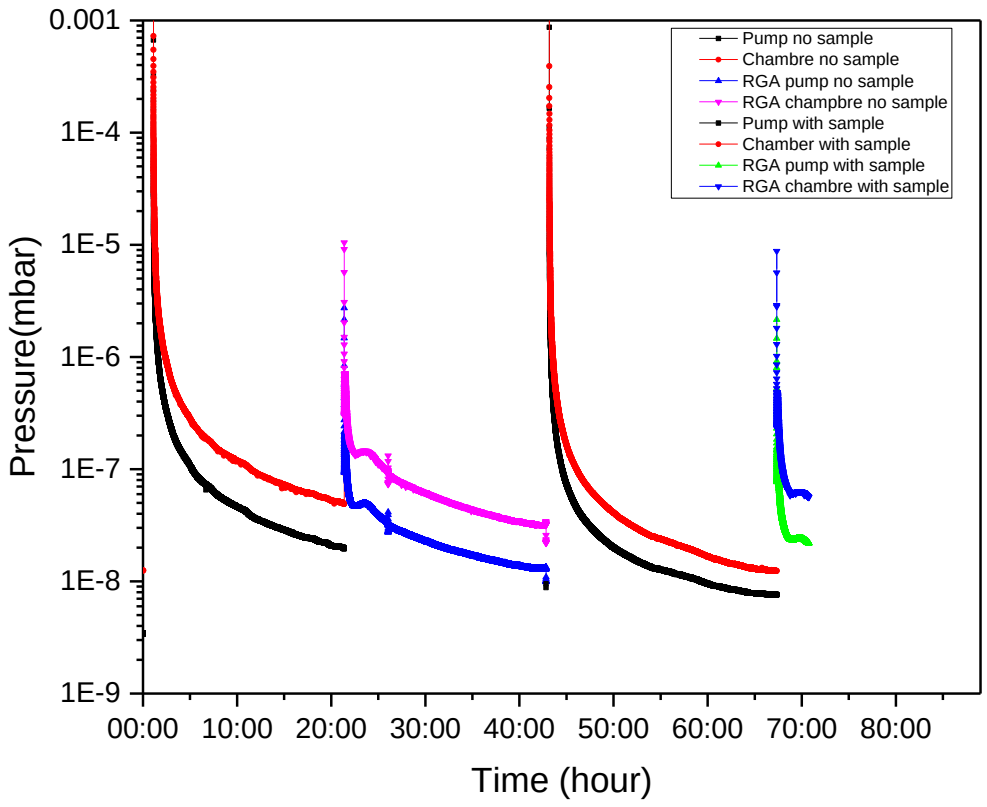

Figure 5.2. Pump down curves without and with thallium bulk sample

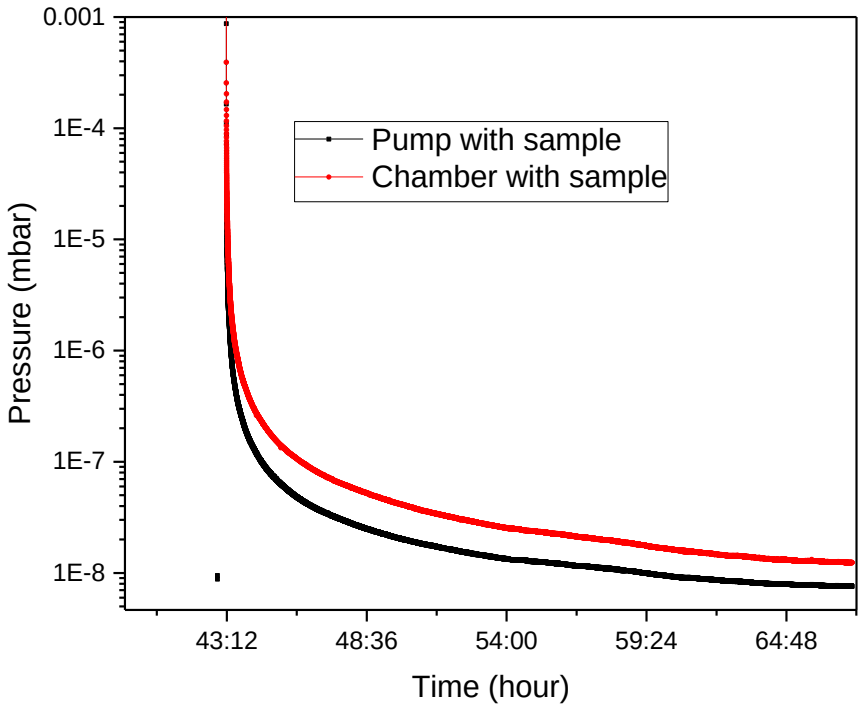

Figur3 5.3. Pumping with thallium bulk sample

The pump-down was done in an unbaked system, and water dominates the outgassing process for metals, so considering the effecting speed of H_2O

So,

S_{eff} = 12 l/s

P_1= 7.6×10^{-9} mbar

P_2= 1.2×10^{-8} mbar

P_1 is the pressure attained without the sample, and P_2 is the pressure in the presence of the sample after 10 hours, and

Hence the outgassing rate after 10 hours for the thallium sample is,

$$Q = (P_2\text{-}P_1) \times S_{eff}$$

$$\boldsymbol{Q}= (1.2\times10^{-8} - 7.6\times10^{-9}) \text{ mbar} \times 12 \text{ l/s}$$

$$Q10h = 5\times10^{-8} \text{ mbar. l/s}$$

Since the sample was 1 cm^2 in size, the outgassing rate for the thallium-based bulk sample is calculated as 5×10^{-8} mbar. l/s per cm^2 after 10 hours, whereas copper's current beam screen material has an outgassing rate of 3×10^{-10} mbar.l/s per cm^2.

5.2.2 Residual gas analysis (RGA)

The choice of material for vacuum systems involves many considerations, and pressure is not the only problem. In addition, the presence of various gases or their components in the vacuum must be analysed. RGA is a preferred technique to confirm the absence of impurities [117]. Usually, some gases and their components are always present: H, O and C, H_2, CO_2, or N_2. These gases can be detected by any means except by their mass. Electrons ionise the gas molecules, and these ions move differently in the magnetic field due to their masses [118].

For this purpose, a spectrometer called a residual gas analyser is used to measure the composition of a gas present in a vacuum system. The RGA usually consists of five components: (I) ioniser converts the gas molecules or atoms into positive ions, (II) electrostatic lens array is a series of lenses that focuses and accelerates the positive ions into a beam. (III) Then this beam is ordered by their *e*-masses using magnetic fields using mass filtering (quadrupole). Then, (IV) the ion detection philtre system detects and measures the mass-to-charge ratio of the filtered ions as an ion current using either a Faraday cup or an extended secondary electron multiplier. Finally, the (V) RGA spectrum between ion current and mass can be plotted in (amu – atomic mass unit). An RGA was also performed on the pellet and can be seen in Figure 5.4.

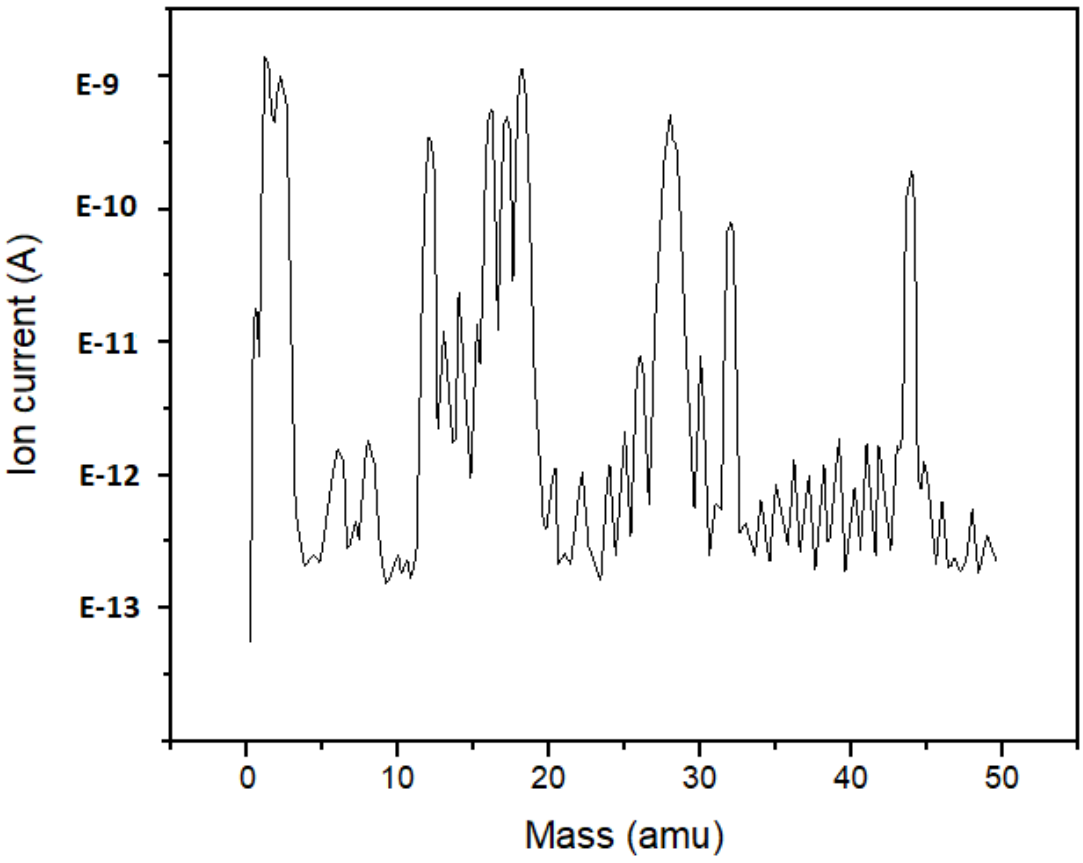

Figure 5.4. Residual gas scan on a thallium-based sample in an unbaked system

In general, any vacuum should contain a detectable amount of hydrogen (H_2) (2 amu), water (H_2O) (18 amu), carbon monoxide (CO) (28 amu) and carbon dioxide (CO_2) (44 amu). Moreover, these peaks are well seen in Fig. 4 for the thallium sample. The peak at 14 amu is from atomic N^+ and N_2^+, and the water peaks around 16-18 amu are caused by the ions O+, HO^+ and H_2O+. The peaks at 32 amu and 34 amu indicate molecular and isotopic oxygen, and 44 for carbon dioxide -the peaks for doubly ionised carbon dioxide CO_2^{++} and C^+ are at 22 amu and 12 amu. In addition, the peak increases at 19 and maybe fluorine.

5.2.3 Secondary electron yield (SEY)

As already described above, a secondary electron yield is a phenomenon in which high-energy electrons interact with the material to produce secondary electrons generating the electron cloud[119]. Moreover, in the vacuum of a particle accelerator, the e-cloud is formed with the secondary electrons, which leads to a disturbance of the vacuum and thus to the beam collision event [120]. Therefore, electron cloud growth can be a grave limitation in bunch currents and total beam currents if multipacting occurs. Multipacting can occur when the electron cloud dynamics can resonate with the accelerator beam's bunch spacing. This can cause instabilities along a bunch of beams and even instabilities within a single bunch, known as head-tail instabilities.

The secondary electron emission coefficient or yield measurements are usually performed in a UHV chamber consisting of a sample holder, an electron gun and a collector. The total SEY, δ, is thus defined as:

$$\delta = I_C / I_P$$

Where I_c is the collector current, I_P is is is is the primary electron current sent by the electron stream (ranges from 50-2000 eV) and is the current of the incident electron beam. The SEY (δ) depends solely on the emission and incident electron beam current and depends on the primary electrons, material, chemical and physical properties, and interaction in a vacuum. These electrons can interact with the beam and reduce the quality of the wave. Therefore, it is important to minimise electron production. In the LHC, the BS used is copper, which has an emission coefficient greater than two. A bake-out at 300 °C lowered this value to 1.8 [119]. The threshold value is 1.3 [121], and for the LHC upgrade, copper is deposited with amorphous carbon (a-carbon). For carbon-coated copper, the yield coefficient is about 0.8. Moreover, SEY is always greater than one for a metal and carbon films yield SEY less than one.

Three thallium-based bulk samples (pellets of 2 cm) were prepared using the solid-state method mentioned in Chapter 2 to calculate the SEY of thallium-based high-temperature superconductors. Then, each of them was formed into squares of 1 cm^2. These samples (labelled as pellet 1, 2 and 3) were placed in the vacuum chamber; an electron beam was applied from 50-2000 eV, and SEY was recorded simultaneously. The SEY curves for the thallium samples in Figures 5.5 and δ_{max} are 2.17, 2.04, and 2.24 at 500, 950, and 450 eV, respectively. Thus, the SEY is greater than 2 for all thallium bulk samples. It was mentioned earlier that the bare surfaces always give SEY greater than one due to the impurities.

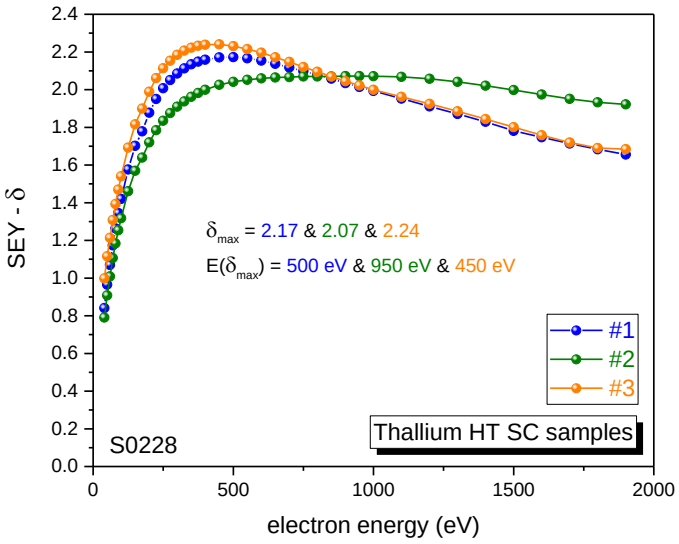

Figure 5.5. The Secondary electron yield curves three pellets

As already anticipated, some processes may also reduce it: Modifying surface layer composition with argon glow discharge and deposition of titanium nitride [122], Carbon deposition, baking out of the chamber and especially increased surface roughness can permanently reduce SEY [123]. These techniques have some limitations; for example, bake-out is not directly applicable to accelerators, so graphitic carbon deposition is considered one of the most effective alternatives to mitigate the *e*-cloud [124]. Moreover, graphitic carbon is vacuum compatible, a good electrical conductor, not susceptible to adsorption of atmospheric gases [125]and has an emission coefficient of δ_{max} around 1 [126]. Electrons impinging on a contaminated layer have been found to form thin carbon or hydrocarbon layers that increase the work function Φ and decrease the transmission coefficient of the potential surface barrier by additional inelastic scattering of secondary electrons [127], and carbon is suitable also for low outgassing, as it is believed to be more stable against residual gas in a vacuum chamber at low temperature[128]

Therefore, one of the pellets was deposited with 150 nm titanium (for adhesion) and 100 nm amorphous carbon to decrease the secondary electron yield. Amorphous carbon (a-C) was deposited on one pellet by DC magnetron sputtering with a graphite cathode. Figures 5.6 and 5.7 are SEM micrographs of the a-C deposited pellet sample,

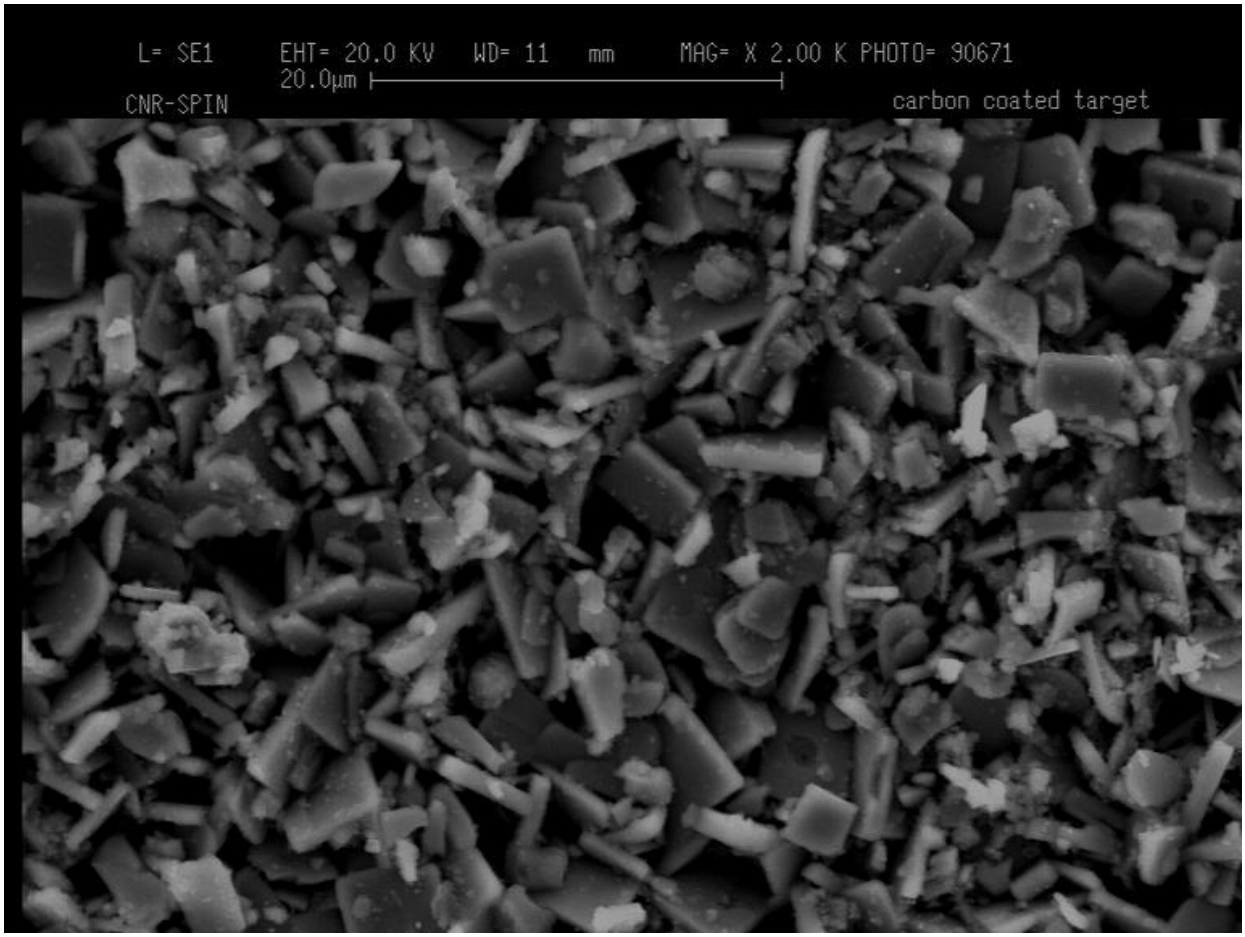

Figure 5.6. SEM image of 100nm amorphous carbon (a-C) coated pellet

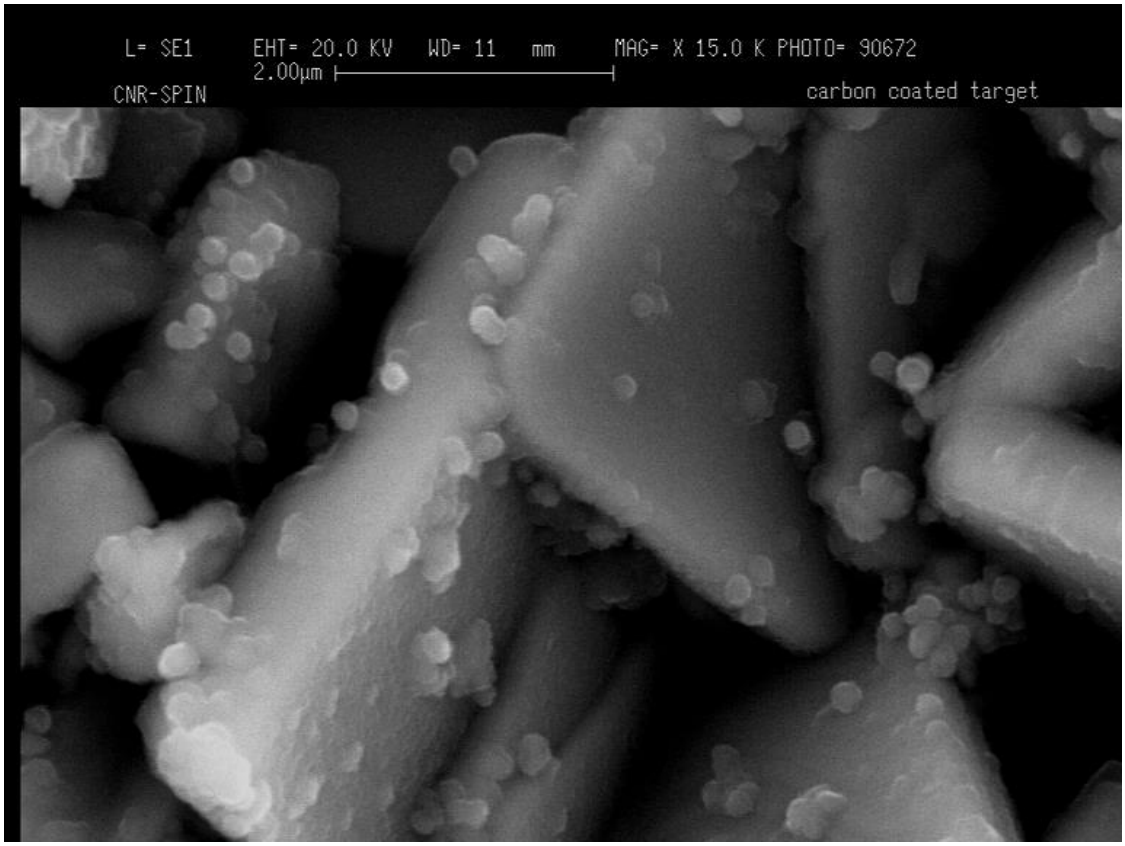

Figure 5.7. High-resolution SEM image of a-carbon coated pellet

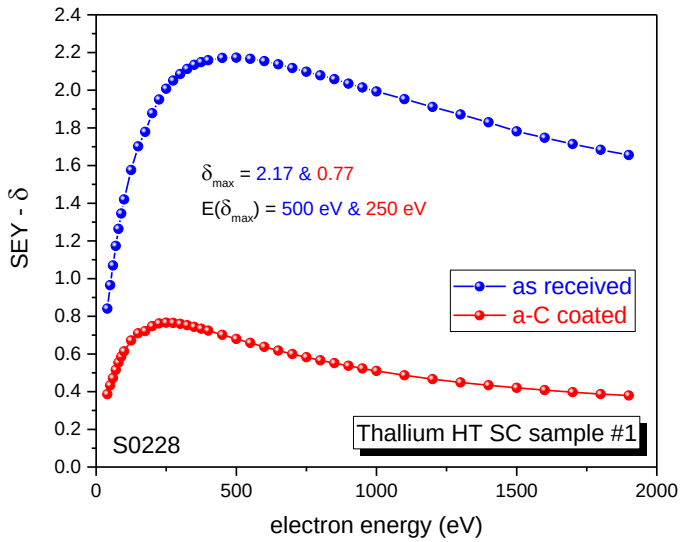

Figure 5.8. The Secondary electron yield curves of the pellet before and after a-Carbon coating

The SEY was performed on thallium bulk sample 1 in a vacuum. The δmax value was 2.17 at 500 eV, and after coating (150 nm Ti and 100 nm carbon), the δmax value surprisingly dropped to 0.77 at 250 eV.

As mentioned in the first chapter, good conducting properties are required to replace copper in FCC-hh, and high critical current (T_c) is the top requirement to reduce the power consumption. So, the resistivity measurement was also performed on the carbon-coated sample by the four-probe technique to realize the a-C influence on the superconducting properties. The critical temperature is estimated at around 121 K (Figure 5.9), so a-C coating does not appear to affect the superconducting properties of superconductors.

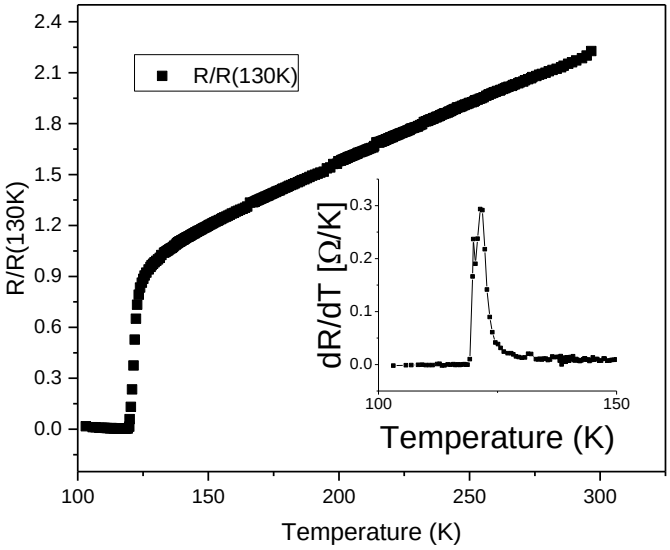

Figure 5.9. Resistivity measurement performed on a-C deposited bulk sample. The calculate T_c is 121 K

SEY measurements were also performed on two thallium-based thin (8 mm diameter each) films deposited on the silver substrates. These thin films designated STL-30-4 and STL-30-5 were deposited by electrodeposition and annealed under optimised conditions, i.e. These thin films designated STL-30-4 and STL-30-5 were deposited by electrodeposition and annealed under optimised conditions, i.e., conditions, i.e. conditions, i.e. conditions, i.e. at 885 ◦C for 40 minutes (mounted on a sample holder in Figure 5.9).

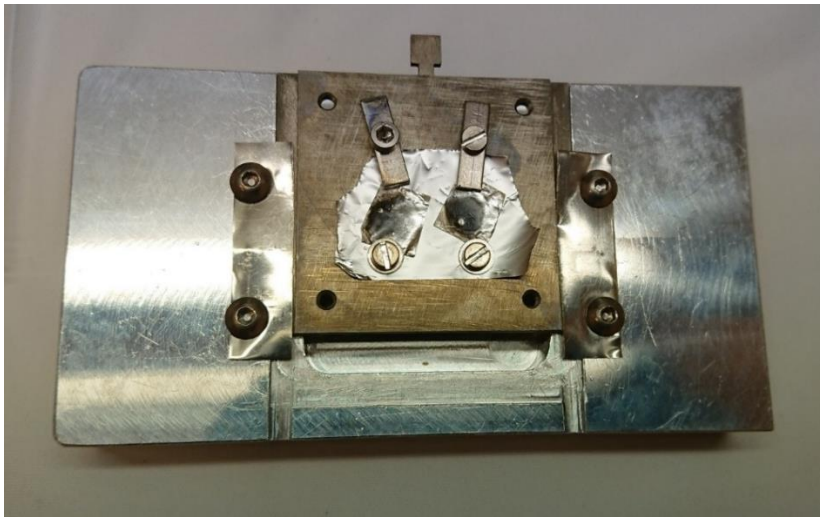

Figure 5.10. Two thallium based thin films deposited on silver are placed over a clamp to perform Secondary electron yield measurements before a-Carbon coating

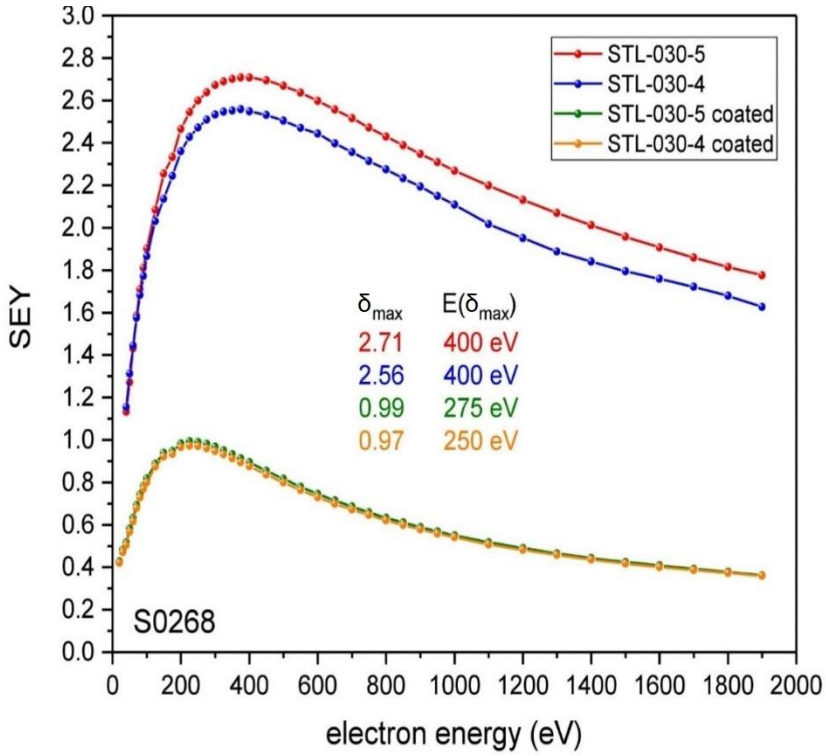

Figure 5.11. The Secondary electron yield curves of two thin films before and after a-carbon coating and shows a remarkable reduction in values

The SEY Vs electron binding energy curve in Figure 11 shows that δmax at 400 eV for STL-30-4 and STL-30-5 before a-coating was measured at 2.56 and 2.71, respectively. After a-coating, the δmax values decreased to 0.97 at 250 eV and 0.99 at 275 eV, respectively. This measurement shows that after the coating of amorphous carbon on thallium bulk and thin-film samples, the values of SEY decreased to a much lower level compatible with the accelerator environment.

5.2.4 X-ray Photoemission Spectroscopy (XPS)

X-ray photoemission spectroscopy is a well-known surface-sensitive technique for identifying the elements and surface of a material. XPS has also been performed on thallium-based superconductors in high vacuum using Al K_α radiation, mainly to understand the release of vapours of the heavy elements (Tl, Bi, Pb) in a vacuum. For example, figure 5.12 shows an XPS spectrum performed on an aluminium foil (mentioned in the section). No traces of heavy elements were found on the foil, only the presence of oxygen.

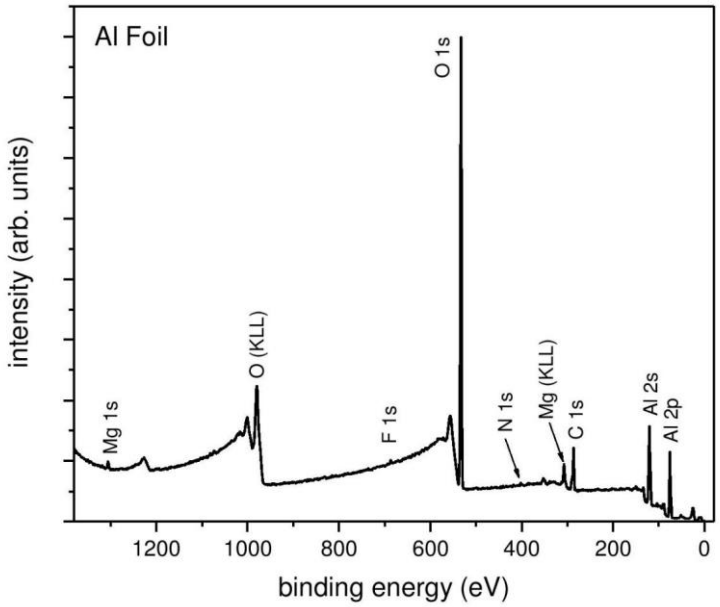

Figure 5.12. XPS spectra of aluminium foil touching the thallium superconducting pellet showing no detectable trace of thallium.

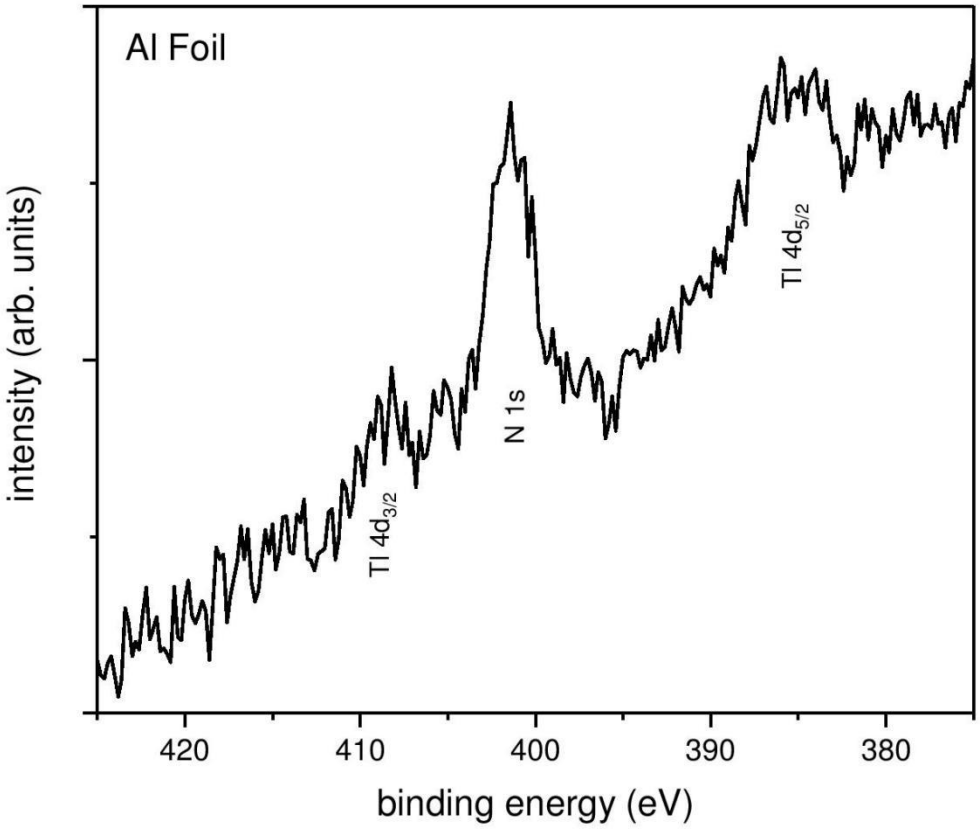

Figure 5.13. XPS result shows minor peaks of Tl-4d5/2 and Tl-4d3/2, and the estimated amount of Tl is negligibly low

Figure 13 shows a minor presence of thallium, but no other heavy metal (Bi or Pb) was detected. However, a high release of material in vapours makes it an incompatible choice. The estimated amount of Tl detected is 0.1 at%, and thus the vapour release from a bulk sample of 1 cm2 size pumped in a vacuum chamber for 24 hours is low to disturb a system severely.

Usually, both SEY and XPS are performed on deposited carbon samples to analyse SEY reduction and surface composition change.

In the previous section, it was found that the SEY coefficients decreased to acceptably low values. In addition, XPS was performed on a-carbon deposited bulk samples (Figure 14) and thin-film samples (Figure 15),

Moreover, mainly the C1s state of carbon was found to be around 285 eV and a low O-1s (Table 5.9).

Table 5.9: Atomic percentages of elements found by XPS on carbon deposited thallium based superconducting samples.

Sample	C	O	N	Ar
a-C/Ti coating on CVD -HT-SC Layer	96.4	3.4	0.2	<0.05
a-C/Ti coating on HT-SC Pellet	95.2	4.7	0.1	<0.05

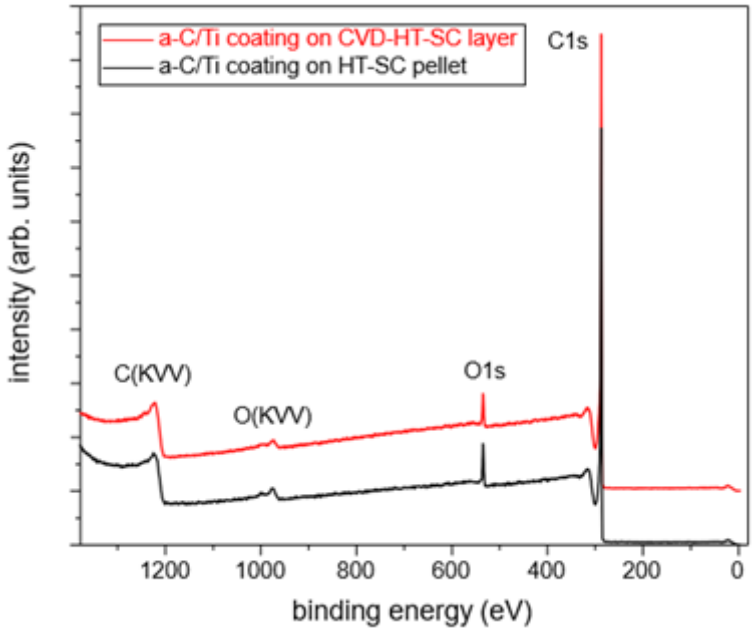

Figure 5.14. XPS spectra for the a-carbon deposited pellet (black) and thin film(red).

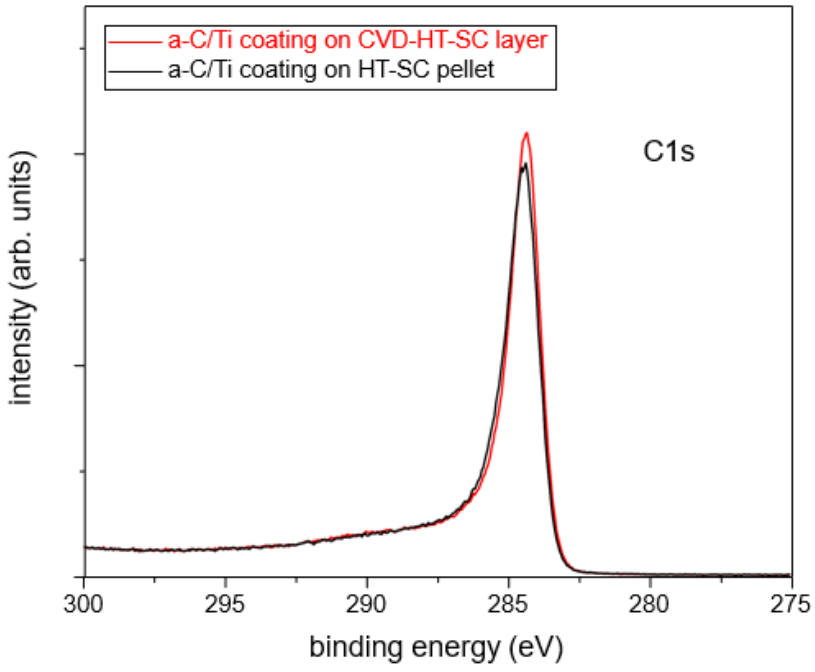

Figure 5.15. XPS spectra for the deposited carbon

5.3 Conclusions

The RGA, SEY, and XPS on the $Tl_{0.7}Bi_{0.4}Pb_{0.4}Sr_{1.6}Ba_{0.4}Ca_{1.9}Cu_3O_{9-\delta}$ pellets and thin films were performed to validate the vacuum compatibility.

A superconducting bulk sample was placed inside the vacuum chamber. Later, the aluminium foil was analysed with the XPS to check for the thallium contaminant. The XPS shows a minimal amount of thallium, and thallium vapours do not affect the vacuum. As thallium is volatile and after high temperature annealing of the sample, the thallium concentration on the sample's surface decreases. The outgassing rate for thallium based bulk sample is calculated after 10 hours of pumping.

The secondary electron yield was measured for the thallium-based superconductors, and the secondary electron yield for pellets 1, 2, and 3 are 2.17, 2.04, and 2.24, respectively. After the a-carbon coating on pellet one, the emission coefficient value decreased from 2.17 to 0.77.
The SEY was also measured for thin films labelled STL-30-4 and STL-30-5, and δ_{max} were measured to be 2.56 and 2.71 at 400 eV before a-carbon coating. However, after the a-C coating, the δmax values decreased to 0.97 and 0.99, respectively.

References

[1] G. Aad *et al.*, “Observation of a new particle in the search for the Standard Model Higgs boson with the ATLAS detector at the LHC,” *Phys. Lett. Sect. B Nucl. Elem. Part. High-Energy Phys.*, vol. 716, no. 1, pp. 1–29, 2012, doi: 10.1016/j.physletb.2012.08.020.

[2] M. Benedikt, A. Blondel, P. Janot, M. Mangano, and F. Zimmermann, “Future Circular Colliders succeeding the LHC,” *Nat. Phys.*, vol. 16, no. 4, pp. 402–407, 2020, doi: 10.1038/s41567-020-0856-2.

[3] M. Benedikt and F. Zimmermann, “Towards future circular colliders,” *J. Korean Phys. Soc.*, vol. 69, no. 6, pp. 893–902, 2016, doi: 10.3938/jkps.69.893.

[4] M. Bicer *et al.*, “First look at the physics case of TLEP,” *J. High Energy Phys.*, vol. 2014, no. 1, 2014, doi: 10.1007/JHEP01(2014)164.

[5] N. Armesto *et al.*, “Nuclear collisions at the Future Circular Collider,” *Nucl. Phys. A*, vol. 956, pp. 854–857, 2016, doi: 10.1016/j.nuclphysa.2016.02.051.

[6] A. Abada *et al.*, “FCC-hh: The Hadron Collider: Future Circular Collider Conceptual Design Report Volume 3,” *Eur. Phys. J. Spec. Top.*, vol. 228, no. 4, pp. 755–1107, 2019, doi: 10.1140/epjst/e2019-900087-0.

[7] O. Gröbner, “Overview of the LHC vacuum system,” *Vacuum*, vol. 60, no. 1–2, pp. 25–34, 2001, doi: 10.1016/s0042-207x(00)00240-2.

[8] M. Benedikt and F. Zimmermann, “Can we afford to wait? Designing the collider of the future,” *Europhys. News*, vol. 48, no. 4, pp. 12–16, 2017, doi: 10.1051/epn/2017401.

[9] V. Baglin, L. Tavian, P. Lebrun, and R. van Weelderen, “Cryogenic Beam Screens for High-Energy Particle Accelerators,” no. May 2012, 2013.

[10] P. Lebrun and L. Tavian, “Beyond the Large Hadron Collider : a first look at cryogenics for CERN future circular colliders,” *Phys. Procedia*, vol. 67, no. 2004, pp. 768–775, 2015, doi: 10.1016/j.phpro.2015.06.130.

[11] C. Libraries, “Theoretical aspects of the behaviour of beams in accelerators and storage rings.”

[12] F. Ruggiero, “Single-beam collective effects in the LHC,” *Part. Accel.*, vol. 50, no. CERN-SL-95-09-AP, pp. 83–104, 1995.

[13] S. Calatroni *et al.*, “Thallium-based high-temperature superconductors

for beam impedance mitigation in the Future Circular Collider," *Supercond. Sci. Technol.*, vol. 30, no. 7, 2017, doi: 10.1088/1361-6668/aa6bd0.

[14] L. Tavian, "Cryogenics," no. February, 2014.

[15] "2017-8." .

[16] I. Bellafont *et al.*, "Design of the future circular hadron collider beam vacuum chamber," *Phys. Rev. Accel. Beams*, vol. 23, no. 3, pp. 1–15, 2020, doi: 10.1103/PhysRevAccelBeams.23.033201.

[17] S. Calatroni, "HTS Coatings for Impedance Reduction in Particle Accelerators: Case Study for the FCC at CERN," *IEEE Trans. Appl. Supercond.*, vol. 26, no. 3, 2016, doi: 10.1109/TASC.2016.2520079.

[18] O. S. Brüning *et al.*, "LHC Design Report," *Cern. Geneva*, p. 548, 2004, [Online]. Available: https://cds.cern.ch/record/782076/export/hx?ln=en.

[19] A. Gurevich and G. Ciovati, "Effect of vortex hotspots on the radio-frequency surface resistance of superconductors," vol. 054502, 2013, doi: 10.1103/PhysRevB.87.054502.

[20] M. W. Coffey and J. R. Clem, "Letters 15," vol. 67, no. 3, pp. 15–18, 1991.

[21] I. Gittleman, "Physical review letters," vol. 16, no. 17, pp. 734–736, 1966.

[22] S. Calatroni and R. Vaglio, "Surface Resistance of Superconductors in the Presence of a DC Magnetic Field: Frequency and Field Intensity Limits," *IEEE Trans. Appl. Supercond.*, vol. 27, no. 5, 2017, doi: 10.1109/TASC.2017.2691604.

[23] M. Martinello *et al.*, "Effect of interstitial impurities on the field dependent microwave surface resistance of niobium," *Appl. Phys. Lett.*, vol. 109, no. 6, 2016, doi: 10.1063/1.4960801.

[24] F. Perez and B. Screen, "Design , Prototyping and Tests of the FCC-hh Vacuum Beam Screen Francis Perez (ALBA) and Paolo Chiggiato (CERN)," pp. 1–20, 2016.

[25] M. F. Chisholm, "Grain boundaries in high-Tc superconductors," *Proceedings, Annu. Meet. Electron Microsc. Soc. Am.*, vol. 46, no. April, pp. 1008–1009, 1988, doi: 10.1017/s0424820100107101.

[26] A. Romanov *et al.*, "High frequency response of thick REBCO coated conductors in the framework of the FCC study," *Sci. Rep.*, vol. 10, no. 1, pp. 1–12, 2020, doi: 10.1038/s41598-020-69004-z.

[27] P. Krkotić, U. Niedermayer, and O. Boine-frankenheim, “Nuclear Inst . and Methods in Physics Research , A High-temperature superconductor coating for coupling impedance reduction in the FCC-hh beam screen,” *Nucl. Inst. Methods Phys. Res. A*, vol. 895, no. October 2017, pp. 56–61, 2018, doi: 10.1016/j.nima.2018.03.049.

[28] X. Obradors and T. Puig, “Coated conductors for power applications : materials challenges,” 2014, doi: 10.1088/0953-2048/27/4/044003.

[29] S. Science, “Coated conductor technology for the beamscreen chamber of future high energy circular colliders Coated conductor technology for the beamscreen chamber of future high energy circular colliders,” 2019.

[30] R. Vaglio and S. Calatroni, “Advances in the study of HTS superconductors for the beam impedance mitigation in CERN-FCC: the thermal runaway problem,” *Eur. Phys. J. Spec. Top.*, vol. 228, no. 3, pp. 749–754, 2019, doi: 10.1140/epjst/e2019-800180-9.

[31] S. Science, “Synthesis and properties of fluorine-doped Tl (1223): bulk materials and Ag-sheathed tapes,” no. 1223, 1998.

[32] L. D. Chang *et al.*, “Microwave surface resistance in Tl-based superconducting thin films,” *Appl. Phys. Lett.*, vol. 55, no. 13, pp. 1357–1359, 1989, doi: 10.1063/1.102475.

[33] R. N. Bhattacharya *et al.*, “Improved electrodeposition process for the preparation of superconducting thallium oxide films,” *Phys. C Supercond. its Appl.*, vol. 333, no. 1–2, pp. 59–64, 2000, doi: 10.1016/S0921-4534(00)00020-4.

[34] H. C. Lai, K. D. Vernon-Parry, J. D. Chern, and C. R. M. Grovenor, “Deposition of thallium-based superconducting thin films by a simple thermal evaporation method,” *Supercond. Sci. Technol.*, vol. 4, no. 7, pp. 306–311, 1991, doi: 10.1088/0953-2048/4/7/007.

[35] T. Systems *et al.*, “Related content Superconductivity in Tl-Bi-Ca-Sr-Cu-O and Tl-Bi- Pb-Ca-Sr-Cu-O Systems,” 1989.

[36] M. A. Subramanian, “Mechanisms for hole doping in thallium cuprate superconductors having single copper-oxygen sheets,” *Mater. Chem. Phys.*, vol. 35, no. 3–4, pp. 240–243, 1993, doi: 10.1016/0254-0584(93)90138-C.

[37] H. Sudra and G. Gritzner, “Under- and over-doped bulk (TlaPb0.5)(Sr0.95Ba0.05)2(Ca0.8Gd0.2)Cu2Oz 1212 superconductors prepared via solution gel synthesis,” *Phys. C Supercond. its Appl.*, vol.

443, no. 1–2, pp. 57–60, 2006, doi: 10.1016/j.physc.2006.04.100.

[38] J. G. Bednorz, M. Takashige, and K. A. Müller, “Susceptibility measurements support high-Tcsuperconductivity in the Ba-La-Cu-O system,” *Prop. Perovskites Other Oxides*, vol. 193, pp. 555–565, 2010, doi: 10.1142/9789814293365_0011.

[39] M. K. Wu *et al.*, “Superconductivity at 93 K in a new mixed-phase Yb-Ba-Cu-O compound system at ambient pressure,” *Phys. Rev. Lett.*, vol. 58, no. 9, pp. 908–910, 1987, doi: 10.1103/PhysRevLett.58.908.

[40] “c1, 12 r.pdf.” .

[41] Y. Ohishi, S. Mitachi, H. Takahashi, I. Minato, and M. Yurddaskal, “Related content A New High-T c Oxide Superconductor without a Rare Earth Element,” 1988.

[42] A. W. Sleight, J. Gopalakrishnan, C. C. Torardi, and M. A. Subramanian, “High T c Copper-oxide superconductors of thallium , bismuth and lead,” vol. 1594, no. June, 2016, doi: 10.1080/01411598908244507.

[43] C. N. R. Rao and B. Raveau, “Structural Aspects of High-Temperature Cuprate Superconductors+,” vol. VII, no. 7, pp. 106–113, 1989.

[44] C. Structures, “A New Class of Crystal Structures,” vol. 61, no. 6, 1988.

[45] Y. Gao, P. Lee, J. Ye, P. Bush, V. Petricek, and P. Coppens, “THE INCOMMENSURATE MODULATION IN THE Bi2Sr2_,CaxCu06 SUPERCONDUCTOR, AND ITS RELATION TO THE MODULATION IN Bi2Srz_,CaxCuzOs Yan GAO, Peter LEE, James YE, Peter BUSH, Vaclav PETRICEK and Philip COPPENS,” *Phys. C*, vol. 160, pp. 431–438, 1989.

[46] C. C. Torardi *et al.*, “Crystal structure of Tl2Ba2Ca2Cu 3O10, a 125 K superconductor,” *Science (80-.).*, vol. 240, no. 4852, pp. 631–634, 1988, doi: 10.1126/science.240.4852.631.

[47] J. B. Parise and J. Gopalakrishnan, “Superconducting The Orthorhombic Form,” pp. 432–436, 1988.

[48] M. Greenblatt, “Tl2Ba2_xSrxCaCu20 s,” vol. 156, pp. 775–780, 1988.

[49] Z. F. Ren and J. H. Wang, “Uniform and flexible 24-meter superconducting tape of silver-sheathed Tl0.5Pb0.5Ba0.4Sr1.6Ca 2Cu3O8.2,” *Appl. Phys. Lett.*, vol. 61, no. 14, pp. 1715–1717, 1992, doi: 10.1063/1.108433.

[50] M. A. Subramanlan, P. L. Gai, A. W. Sleight, and E. Station, “(Tll-xBix)Sr2Ca2Cu309,” vol. 25, no. c, pp. 101–106, 1990.

[51] S. Li and M. Greenblatt, “Preparation and superconducting properties of (Tl,Bi)Sr2CaCu2Oy,” *Phys. C Supercond. its Appl.*, vol. 157, no. 2, pp. 365–369, 1989, doi: 10.1016/0921-4534(89)90029-4.

[52] I. K. Gopalakrishnan and J. V Yakhmi, “Stabilization enhancement of superconductivity in TlBa2Cu05 _ B at 9 . 5 K and its to 43 K in T1BaSrCu05 _ 6,” vol. 175, pp. 183–186, 1991.

[53] M. A. Subramanian, J. B. Parise, C. C. Torardi, J. Gopalakrishnan, J. C. Calabrese, and A. W. Sleight, “LElTERS Structure of TIBa2Ca2Cu309,” pp. 192–195, 1988.

[54] B. Morosin *et al.*, “Structural and compositional characterization of polycrystals and single crystals in the Bi- and Tl-superconductor systems: Crystal structure of TlCaBa2Cu2O7,” *Phys. C Supercond. its Appl.*, vol. 152, no. 5, pp. 413–423, 1988, doi: 10.1016/0921-4534(88)90046-9.

[55] N. N. W. Kolesnikov, “STRUCTURE OF SUPERCONDUCTING SINGLE CRYSTALS OF T1Ba2(Cao.OTTIo.13)Cu207, TC=80 K,” vol. 164, pp. 1663–1664, 1989.

[56] H. City, “Flux pinning in single TMayer 1223 superconductors,” vol. 183, pp. 67–72, 1991.

[57] D. N. Zheng *et al.*, “Magnetic and transport measurements of Tl-1223 superconductors,” *J. Appl. Phys.*, vol. 77, no. 10, pp. 5287–5292, 1995, doi: 10.1063/1.359282.

[58] S. Science, “powder and Ag-sheathed tape,” 1995.

[59] M. D. Marcos and J. P. Attfield, “Crystal structure of Tl0.5Pb0.5Sr2Ca2Cu3O 9 at 300 K and around Tc (118 K),” *Phys. C Supercond. its Appl.*, vol. 270, no. 3–4, pp. 267–273, 1996, doi: 10.1016/S0921-4534(96)00518-7.

[60] J. L. Jorda, “Thallium-based superconducting cuprates,” *Front. Supercond. Mater.*, pp. 833–868, 2005, doi: 10.1007/3-540-27294-1_22.

[61] R. S. Liu, S. F. Hu, D. A. Jefferson, and P. P. Edwards, “Superconductivity at 124 K in (Tl, Pb)Sr2Ca2Cu3O9,” *Phys. C Supercond. its Appl.*, vol. 198, no. 3–4, pp. 318–322, 1992, doi: 10.1016/0921-4534(92)90207-S.

[62] A. You, M. A. Y. Be, and I. In, “High critical-current densities in,” vol. 1019, no. December 1991, pp. 0–3, 2010.

[63] T. C. Rare and E. O. Transition, “The C Rare Earth Oxide-Corundum Transition and,” vol. 8, no. 9, 1985.

[64] “No Title,” vol. 6, pp. 381–394, 1971.

[65] T. L. Aselage, E. L. Venturini, and J. A. Voigt, “Stability of the Tl-1223 phases,” pp. 1635–1644, 1996.

[66] L. Brewer, “High-Temperature Vaporization Behavior of Oxides II . Oxides of Be , Mg , Ca , Sr , Ba , B , Al ,” vol. 419, no. December 1983, 2009.

[67] J. C. Phys and D. L. Myers, “Thermodynamics of the Tl – O system and Tl-superconductors,” vol. 10383, no. August, pp. 1996–1998, 1998.

[68] C. T. Cheung and E. Ruckenstein, “The formation and role of a phase with glassy appearance in the Tl-Ca-Ba-Cu system,” pp. 245–250, 1990.

[69] E. Ruckenstein and C. T. Cheung, “Reaction pathways in the formation of the Tl-Ca-Ba-Cu superconducting phases,” vol. 14260, no. June 1989, 2021.

[70] S. Adachi, H. Adachi, Y. Ichikawa, R. Sugise, and M. Hirabayashi, “Related content Preparation of Tl 2 Ba 2 Ca 2 Cu 3 O y Thick Films from Ba-Ca-Cu-O Films,” 1988.

[71] S. State, P. Division, and B. Atomic, “Structural aspects of high-T c superconductors from neutron profile refinement studies,” vol. 174, pp. 311–322, 1991.

[72] “TI2CaBa2Cu2Oa (the 2122,” vol. 161, pp. 302–312, 1989.

[73] N. Elgrishi, K. J. Rountree, B. D. McCarthy, E. S. Rountree, T. T. Eisenhart, and J. L. Dempsey, “A Practical Beginner’s Guide to Cyclic Voltammetry,” *J. Chem. Educ.*, vol. 95, no. 2, pp. 197–206, Feb. 2018, doi: 10.1021/acs.jchemed.7b00361.

[74] R. N. Bhattacharya *et al.*, “Improved electrodeposition process for the preparation of superconducting thallium oxide films,” *Phys. C Supercond. its Appl.*, vol. 333, no. 1–2, pp. 59–64, 2000, doi: 10.1016/S0921-4534(00)00020-4.

[75] R. N. Bhattacharya *et al.*, “Structural studies of electrodeposited and sprayed thallium-oxide films,” *Supercond. Sci. Technol.*, vol. 15, no. 9, pp. 1288–1294, 2002, doi: 10.1088/0953-2048/15/9/302.

[76] R. N. Bhattacharya *et al.*, “Superconducting thallium oxide and mercury oxide films,” *Mater. Res. Soc. Symp. - Proc.*, vol. 659, p. II11.2.1-II11.2.6, 2001, doi: 10.1557/proc-659-ii11.2.

[77] N. Furuno, H. Kawai, and Y. Oyabu, “Mechanism of film formation by the

electrodeposition coating," *J. Colloid Interface Sci.*, vol. 55, no. 2, pp. 297–304, 1976, doi: 10.1016/0021-9797(76)90037-0.

[78] X. Zhao, H. Ren, and L. Luo, "Gas Bubbles in Electrochemical Gas Evolution Reactions," *Langmuir*, vol. 35, no. 16, pp. 5392–5408, 2019, doi: 10.1021/acs.langmuir.9b00119.

[79] "Building on bubbles in metal electrodeposition," vol. 269, no. 1990, p. 2000, 2001.

[80] A. Substrates, ; "I !'," vol. I, no. 1, pp. 3122–3125, 2001.

[81] J. M. Phillips, "Substrate selection for high-temperature superconducting thin films," *J. Appl. Phys.*, vol. 79, no. 4, pp. 1829–1848, 1996, doi: 10.1063/1.362675.

[82] K. H. Young *et al.*, "Comparisons of high temperature superconductor thin films on various substrates for microwave applications," *Thin Solid Films*, vol. 206, no. 1–2, pp. 116–121, 1991, doi: 10.1016/0040-6090(91)90403-K.

[83] W. L. Holstein, L. A. Parisi, R. B. Flippen, and D. G. Swartzfager, "Effect of single crystal substrates on the growth and properties of superconducting Tl2 Ba2 CaCu2 O8 films," *J. Mater. Res.*, vol. 8, no. 5, pp. 962–972, 1993, doi: 10.1557/JMR.1993.0962.

[84] M. Giebułtowski, W. M. Woch, R. Zalecki, M. Kowalik, J. Niewolski, and Gondek, "Critical currents of Tl 2 Ba 2 Ca 2 Cu 3 O z bulk superconductors," *Acta Phys. Pol. A*, vol. 135, no. 1, pp. 24–27, 2019, doi: 10.12693/APhysPolA.135.24.

[85] D. S. Ginley and J. F. Kwak, "YBa2Cu306.9 [10].," vol. 156, pp. 592–598, 1988.

[86] T. F. Gelder and R. F. Soltis, "NASA TECHNICAL NOTE l I 1l l l I," vol. 39, no. December 1975, pp. 9–14, 1991.

[87] W. Tao *et al.*, "Rapid deposition of high temperature YBa2Cu3O 7-x superconducting thin films directly on silver substrates," *Appl. Phys. Lett.*, vol. 62, no. 8, pp. 894–895, 1993, doi: 10.1063/1.108558.

[88] A. You, M. A. Y. Be, and I. In, "superconducting Bi-Sr-Ca-Cu-O thin films on silver substrates by organometallic chemical vapor deposition," vol. 976, no. 1990, pp. 1–4, 1998.

[89] D. W. Hazelton, L. Chen, T. W. Piazza, A. Sweeney, and A. E. Kaloyeros, "High Tc conductors by MOCVD on silver substrates," vol. 214, no. June,

pp. 214–222, 2008, doi: 10.1063/1.42074.

[90] H. Nasu, A. Miyamoto, Y. Osaka, T. Shiono, and T. Nakamoto, “Preparation of superconducting Bi-Sr-Ca-Cu-O films on metal substrates using ZrO2 as a buffer layer by pryolysis of organic acid salts,” *Nippon Seramikkusu Kyokai Gakujutsu Ronbunshi/Journal Ceram. Soc. Japan*, vol. 97, no. 10, pp. 1015–1020, 1989, doi: 10.2109/jcersj.97.1015.

[91] D. J. Zurawski, P. J. Kulesza, and A. Wieckowski, “Towards the Electrochemical Synthesis of High Temperature Superconductors,” *J. Electrochem. Soc.*, vol. 135, no. 6, pp. 1607–1608, 1988, doi: 10.1149/1.2096066.

[92] D. Y. Jeong *et al.*, “Electro-deposition of Tl-1223 coated conductors using potential cycling and step methods,” *IEEE Trans. Appl. Supercond.*, vol. 13, no. 2 III, pp. 2614–2617, 2003, doi: 10.1109/TASC.2003.811909.

[93] P. M. Shirage, D. D. Shivagan, and S. H. Pawar, “Studies on room temperature electrochemical oxidation and its effect on the transport properties of TBCCO films,” *Supercond. Sci. Technol.*, vol. 17, no. 7, pp. 853–862, 2004, doi: 10.1088/0953-2048/17/7/006.

[94] D. Y. Jeong, Y. H. Kim, P. M. Shirage, S. Y. Kim, S. Horiuchi, and J. H. Lee, “A new process to prepare thick bufferless Tl-1223/Ag high temperature superconducting coated conductors using electrodeposition,” *Supercond. Sci. Technol.*, vol. 20, no. 12, pp. 1239–1252, 2007, doi: 10.1088/0953-2048/20/12/026.

[95] W. A. LUO *et al.*, “ HIGH-QUALITY Tl 2 Ba 2 Ca 2 Cu 3 O 10 THIN FILMS FABRICATED VIA LASER ABLATION ,” *Mod. Phys. Lett. B*, vol. 07, no. 01, pp. 19–23, 1993, doi: 10.1142/s0217984993000047.

[96] A. Sundaresan *et al.*, “Preparation of Tl-2212 and Tl-1223 superconductor thin films and their microwave surface resistance,” *IEEE Trans. Appl. Supercond.*, vol. 13, no. 2 III, pp. 2913–2916, 2003, doi: 10.1109/TASC.2003.812045.

[97] Z. F. Ren, W. Li, J. H. Wang, Y. T. Wang, and A. M. Hermann, “(T1Bi)o.9Srl.6Bao.4CazCu3Ag~.20x,” vol. 9, no. 2, pp. 1681–1683, 1999.

[98] R. N. Bhattacharya, P. A. Parilla, and R. D. Blaugher, “Processing of thick-film electrodeposited thallium oxide superconductors,” *Phys. C Supercond. its Appl.*, vol. 211, no. 3–4, pp. 475–485, 1993, doi: 10.1016/0921-4534(93)90154-I.

[99] L. Pérez-Arrieta, M. Aguilar-Frutis, J. L. Rosas-Mendoza, C. Falcony, and

M. Jergel, “Two step synthesis of TlBa2Ca2Cu3Ox films on Ag substrates by spray pyrolysis of metal-acetylacetonates,” *Rev. Mex. Fis.*, vol. 54, no. 6, pp. 446–450, 2008.

[100] A. Morales, J. L. Rosas, M. Jergel, and C. Falcony, “Two-zone furnace used to grow Tl-Ba-Ca Cu-O films,” *Superf. y vacío*, no. 9, pp. 154–155, 1999.

[101] Z. F. Ren, W. Li, D. Z. Wang, J. Y. Lao, J. H. Wang, and M. Paranthaman, “Films on Rolling Assisted Biaxially Textured Substrates,” pp. 241–245, 1999.

[102] A. Kaech, “An Introduction To Electron Microscopy Instrumentation, Imaging and Preparation,” *Cent. Microsc. Image Anal.*, pp. 1–26, 2013, [Online]. Available: http://www.zmb.uzh.ch/static/bio407/assets/Script_AK_2014.pdf.

[103] “Module Iv Transmission.”

[104] M. R. Koblischka and R. J. Wijngaarden, “Magneto-optical investigations of superconductors,” *Supercond. Sci. Technol.*, vol. 8, no. 4, pp. 199–213, 1995, doi: 10.1088/0953-2048/8/4/002.

[105] L. N. Vu, M. S. Wistrom, and D. J. Van Harlingen, “Scanning SQUID microscopy of vortex configurations in superconductor arrays,” *Phys. B Phys. Condens. Matter*, vol. 194–196, no. PART 2, pp. 1791–1792, 1994, doi: 10.1016/0921-4526(94)91395-1.

[106] Y. Martin, D. Rugar, and H. K. Wickramasinghe, “High-resolution magnetic imaging of domains in TbFe by force microscopy,” *Appl. Phys. Lett.*, vol. 52, no. 3, pp. 244–246, 1988, doi: 10.1063/1.99482.

[107] R. B. Dinner, “Scanning Hall Probe Microscopy of,” vol. 1974, no. December, pp. 1–4, 2006.

[108] G. K. Perkins, Y. V. Bugoslavsky, X. Qi, J. L. MacManus-Driscoll, and A. D. Caplin, “High field scanning Hall probe imaging of high temperature superconductors,” *IEEE Trans. Appl. Supercond.*, vol. 11, no. 1 III, pp. 3186–3189, 2001, doi: 10.1109/77.919740.

[109] R. B. Dinner, M. R. Beasley, and K. A. Moler, “Cryogenic scanning Hall-probe microscope with centimeter scan range and submicron resolution,” *Rev. Sci. Instrum.*, vol. 76, no. 10, pp. 1–11, 2005, doi: 10.1063/1.2072438.

[110] R. Fuger, F. Hengstberger, M. Eisterer, and H. W. Weber, “Scan techniques for coated conductors,” *IEEE Trans. Appl. Supercond.*, vol. 17,

no. 2, pp. 3753–3756, 2007, doi: 10.1109/TASC.2007.899646.

[111] F. Hengstberger, M. Eisterer, M. Zehetmayer, and H. W. Weber, “Assessing the spatial and field dependence of the critical current density in YBCO bulk superconductors by scanning Hall probes,” *Supercond. Sci. Technol.*, vol. 22, no. 2, 2009, doi: 10.1088/0953-2048/22/2/025011.

[112] M. Nagoshi, Y. Fukuda, N. Sanada, Y. Syono, A. Tokiwa-Yamamoto, and M. Tachiki, “O1s core levels of Bi-Sr-Ca-Cu-O superconductors studied by X-ray photoelectron spectroscopy,” *J. Electron Spectros. Relat. Phenomena*, vol. 61, no. 3–4, pp. 309–322, 1993, doi: 10.1016/0368-2048(93)80022-E.

[113] C. Yin Vallgren *et al.*, “Amorphous carbon coatings for the mitigation of electron cloud in the CERN Super Proton Synchrotron,” *Phys. Rev. Spec. Top. - Accel. Beams*, vol. 14, no. 7, pp. 1–11, 2011, doi: 10.1103/PhysRevSTAB.14.071001.

[114] P. Chiggiato, “Outgassing properties of vacuum materials for particle accelerators,” *arXiv*, pp. 1–47, 2020.

[115] P. Chiggiato, “Vacuum technology for ion sources,” *CAS-CERN Accel. Sch. Ion Sources - Proc.*, pp. 463–502, 2013, doi: 10.5170/CERN-2013-007.463.

[116] P. A. Redhead, “Hydrogen in Vacuum Systems: An Overview,” vol. 243, no. July 2003, pp. 243–254, 2003, doi: 10.1063/1.1597372.

[117] G. Bregliozzi, “Vacuum Acceptance Tests for Particle Accelerator Equipment,” *Cern Accel. Sch.*, pp. 1–11, 2017.

[118] P. E. Miller and M. B. Denton, “The quadrupole mass filter: Basic operating concepts,” *J. Chem. Educ.*, vol. 63, no. 7, pp. 617–622, 1986, doi: 10.1021/ed063p617.

[119] V. Baglin *et al.*, “The secondary electron yield of technical materials and its variations with surface treatment_Baglin_2000.pdf,” pp. 217–221, 2000.

[120] C. Yin Vallgren *et al.*, “Low secondary electron yield carbon coatings for electron cloud mitigation in modern particle accelerators,” *IPAC 2010 - 1st Int. Part. Accel. Conf.*, pp. 2375–2377, 2010.

[121] M. A. Furman and V. H. Chaplin, “Update on electron-cloud power deposition for the Large Hadron Collider arc dipoles,” *Phys. Rev. Spec. Top. - Accel. Beams*, vol. 9, no. 3, pp. 1–14, 2006, doi: 10.1103/PhysRevSTAB.9.034403.

[122] E. L. Garwin, F. K. King, R. E. Kirby, and O. Aita, “Surface properties of metal-nitride and metal-carbide films deposited on Nb for radio-frequency superconductivity,” *J. Appl. Phys.*, vol. 61, no. 3, pp. 1145–1154, 1987, doi: 10.1063/1.338159.

[123] N. Curren, A. Jensen, and F. Roman, “Secondary Emission Electron Characteristics of Molybdenum-Masked , OFHC Copper Ji _ ii,” 1990.

[124] A. Santos, N. Bundaleski, B. J. Shaw, A. G. Silva, and O. M. N. D. Teodoro, “Increase of secondary electron yield of amorphous carbon coatings under high vacuum conditions,” *Vacuum*, vol. 98, pp. 37–40, 2013, doi: 10.1016/j.vacuum.2012.11.005.

[125] S. Calatroni, P. Chiggiato, P. C. Pinto, D. Hynds, M. Taborelli, and C. Y. Vallgren, “Amorphous-Carbon Thin Films for the Mitigation of Electron Amorphous-Carbon Thin Films for the Mitigation of Electron Clouds in Particle Accelerators,” no. November 2014, pp. 128–132, 2008.

[126] N. R. Whetten, “Secondary electron emission of pyrolytic graphite cleaved in a high vacuum,” *J. Appl. Phys.*, vol. 34, no. 4, pp. 771–773, 1963, doi: 10.1063/1.1729532.

[127] J. Halbritter, “Enhanced electron emission and its reduction by electron and ion impact,” *IEEE Trans. Electr. Insul.*, vol. EI-18, no. 3, pp. 253–261, 1983, doi: 10.1109/TEI.1983.298609.

[128] S. Kato, H. Oyama, and H. Odagiri, “Surface modification of vacuum wall by carbon and its outgassing,” *Vacuum*, vol. 41, no. 7–9, pp. 1998–2000, 1990, doi: 10.1016/0042-207X(90)94156-K.

Summary

$Tl_{0.7}Pb_{0.2}Bi_{0.2}Sr_{1.6}Ba_{0.4}Ca_{1.9}Cu_3O_{9+\delta}$ (Tl-1223) have been fabricated and studied as a possible coating for the beam screen material of the Future Circular Collider (FCC-hh).

The thesis consists of five chapters. The **first chapter** introduces the motivation to fabricate and investigate the advantages of thallium superconducting materials as the specific application of beam screen coatings.

The **second** and **third chapters** of the thesis provide experimental set-ups and techniques for synthesising Tl-based bulk samples and thin films, respectively. The synthesis of pure bulk superconductors, presenting a high critical temperature of 120 K, has been obtained (after standard calcinations) by preparing the powder mixture in ball milling for 60 hours in a controlled atmosphere followed by a high-temperature reaction treatment 905 ˚C for 3 hours. The **third chapter** describes electrolyte formulation, cyclical voltammetry performed on the electrolyte to locate all seven elements in precursors, preparation of substrates, and deposition of precursors on substrates *via* electrodeposition superconducting phase formation thermal treatments. Many work approaches, namely pulse potential deposition, unreacted thallination source, time and temperature optimisation, have been applied to produce the thin film coatings with maximum coverage containing desirable phase to enhance the superconducting properties.

In these chapters also X-ray diffraction (XRD), Scanning Electron Microscopy (SEM), four-probe resistivity measurements performed on the thallium bulk and coating superconductors (i.e. the standard characterization analysis) are reported.

The **fourth chapter** is dedicated to microstructural and physical characterisations performed on, Tl-1223 bulk and thin films. The chapter covers detailed Scanning Electron Microscopy (SEM), Transmission electron microscopy (TEM), scanning quantum interference device (SQUID), and Scanning Hall Probe Microscopy (SHPM) measurements performed at USTEM and atominstitut in Vienna, Austria. These deep characterizations lead to understanding how crucial phase formation is, how it is important to control the competitive growth of the two main phases, Tl-1223 and Tl-1212, and the crucial role of the grain misalignment. As the main result, a current flowing in Tl-superconducting grain clusters achieving 8 10^{10} A/m2 at 4.2 K is presented. Furthermore, advanced structural, chemical (e.g. surface analysis was done by X-ray Photoelectron Spectroscopy (XPS) at CERN) and morphological analysis are presented

The **fifth** and the **last chapter** describes the vacuum and the particular particle-accelerator-environment compatibility of Tl-1223. In particular, the outgassing rate, the residual gas analysis (RGA), secondary electron yield (SEY) and X-ray Photoelectron Spectroscopy (XPS) before and after the deposition of an amorphous carbon coating were performed at CERN. The nominal outgassing rate after 10 hours, no detection of heavy metals in RGA and especially the desired SEY coefficient < 1 were measured, showing the full capability of the Tl(1223) phase with the FCC environments.

As a conclusion we showed that Tl(1223) has the necessary functional characteristic as critical temperrure, critical field and Jc (at least at millimetric scale) and also that it is vacuum compatible making it a potential solution for improving the beam stability in high-energy h-h particle accelerators or other suitable applications.

Annexe 1

European Advanced superconductivity Innovation and Training (EASITrain)

European Advanced superconductivity Innovation and Training (EASITrain) is Marie Sklodowska-Curie Action (MSCA) Innovative Training Networks (ITN) that received its funding from the European Union's H2020 Framework Programme under grant agreement number 764879. This EU funded four-year (1.10.2017 to 30.9.2021) project consists of 13 beneficiaries, ten partners, located in 5 different countries and managed by CERN. The project started with an aim to train the fifteen Early-Stage Researchers (ESRs) into a well-trained group of experts in the field of superconductivity, help them understand the behaviour of superconductors on a broader level, establishing innovative products (including thin films and wires), improving cryogenic systems for large scale systems, and creating a solid curriculum to be the qualified experts.

All 15 Early-Stage Researchers (ESRs) are enrolled in PhD programmes covering physics, engineering, and economics in European universities and are given equal opportunities for training, secondments, and participation in international conferences and workshops.

Well organised and managed project applies well strategy to train future experts and creates opportunities, somehow, to link them.

EASITrain has offered three EASISChools to arrange academic seminars for students for different scientific trainings and superconductivity during the four years.

Two-week EASISchool 1 (August 30 -14 September 2018) was organised at the Technical University of Vienna (TUW), Austria. The first week was open to almost 30 external PhD participants. It was dedicated to applied superconductivity, and it covered almost all the topics of superconductivity, from low-temperature superconductors to high-temperature superconductors and their applications. Furthermore, students were taken to Visit Reactor and Superconductivity Lab at Atominstitut, and another trip was arranged to particle therapy centre MedAustron where cancer patients are being treated.

The second week was mainly focused on training ESRs for Project management, a two-day innovating management training at WU, and media training at Terra Mater Factual Studios in Vienna.

The EASISchool 2 was organised in autumn 2019 (September 30 to October 4) for two days at CEA in Paris-Saclay and three days in Grenoble, France. The researchers had the opportunity to learn Cryogenic and its applications in medical, instrumentation, accelerators, magnets and space, superconducting systems, large-scale refrigeration. There were also visits to Neurospin CEA, Accelerator Lab, CEA Cryomagnetism Lab, National High Magnetic Field Laboratory, Air Liquide Advanced Technology, and CEA cryogenics Lab to visualise cryogenic systems on an application-level during the school.

The last school of the project, EASISchool 3, was held at CNR-SPIN in Ligurian city Genova, Italy. The school was arranged from September 28 to October 6. The school's main focus was to cover RF superconductive accelerating cavities, Superconducting magnets design modelling and manufacturing, Superconducting devices sensing, and quantum computation is around.

And the last two days, 8-9 October 2019, were dedicated to researchers organised workshop where external participants and ESRs presented their work.

EASITrain, being a broad research and training program for a prosperous career, besides the academic activities and training, ESRs were offered to train for project management, communication skills as a scientific speaker, enhancement of writing skills to be able to write reports, articles, and acceptable grants, understanding of Intellectual properties rights and submitting a patent.

Along with other projects in EASITrain, the production of thallium based high temperature superconducting thin films for the FCC is allotted to ESR 6 that belongs to WP 3. This research is dedicated to restarting the abandoned research on thallium-based cuprate superconductors with an innovative use as beam screen coatings to shield the magnets in the FCC.

Annexe 2

Formation of EASITrain

The project consists of 8 work packages (WP) (Table no. 2), and 15 early stage researchers (ESRs) and the ESRs belongs to a WP(s): from materials to manufacturing.

Table 10. List of work packages in EASITrain project

WP	Title
1	Management
2	Materials
3	Manufacturing
4	Cryogenics
5	Valorisation
6	Training
7	Communications
8	Ethics requirements

Table 11. A list of ESRs, their institutes and projects

ESR no.	**WP**	**Home institute & Supervisor**	**PhD institute & Supervisor**	**Project**
1.	2	CERN & J.Bremer	Uni. Siegen & J. Knobloch	The realisation of the quality and performance of NbN and Nb_3Sn superconductors from room to liquid helium temperature.
2.	2	Buker &	TUW &	Evaluation of superconductive tapes and wires at different temperatures

		A Usoskin	M Eisterer	
3.	4	CEA & B. Boudouy	U.Paris Saclay & B. Boudouy	Study of heat and mass transfer in superfluid helium in confined geometries
4.	4	CEA & F. Millet	U.Grenoble Alpes	Cooling systems to distribute Cryogens to SC magnets
5.	4	WUW & P. Keinz	WUW & P. Keinz	Evaluate innovation management methods and exchange in high tech systems
6.	3	CNR-SPIN & E. Bellingeri	Uni. of Genoa Marina Putti	Fabrication and improvement of thallium based thin films for the future applications
7.	3	Columbus & D. Magrassi		Advancement of MgB_2 wires for the production of high magnetic field
8.	2	HZB & J. Knobloch	Uni. Siegen & O. Kugeler	RF properties of superconducting Nb_3Sn and NbN thin films
9.	3	I-CUBE & E. Cantergiani	ENSTA-Bretagne N. Jacques	Determining the Electro-Hydraulic Forming limit of copper to use as a substrate
10.	3	INFN-LNL & C.Pira	U. Padova & C.Pira	Surface coating techniques for SRF cavities.
11.	4	TUD & C. Haberstroch	TUD & C.Haberstroch	Neon-Helium (Nelium) gas mixture to refrigeration cycle to aim at 20-70 K

12.	2	TUW & J. Bernardi	TUW & J. Bernardi	Microstructural characterisation of superconducting tapes, wires and thin films.
13.	2	TUW & M.Eisterer	TUW & M.Eisterer	Characterisation using SQUID, Scanning hall Probe Microscopy of superconducting wires and tapes
14.	3	USIEGEN & M. Vogel	USIEGEN & X. Jiang	Synthesation of NbN and Nb_3Sn superconductors
15.	4	USTUTT & D. Vogt	USTUTT & D. Vogt	Optimisation of efficient turbo compressors for Nelium

Annexe 3

Thallium safety: Preparation of controlled and safe workbench to prepare thallium superconductors

Thallium compounds are considered potentially toxic. Working with Tl-compounds can produce the thallium containing dust; preparing and heating the Tl-electrolyte to deposition superconducting thin-film precursors can produce Tl- Vapours. Moreover, airborne Tl can cause illness by ingestion, inhalation and skin contact. However, dealing with the toxic material in a controlled system can help with safe practices. A properly placed exhaust system can control the vapours by capturing them. For the safe synthesis of thallium superconductors, a new laboratory was established at Consiglio Nazionale Delle Ricerche (CNR- SPIN) to ensure the safe restart of toxic thallium-based HTS.

A ventilation system was fitted to increase air exchange rate, and a specifically designed vacuum cleaning system based on a Goretx® filter and external exhaustion was adjusted in the Tl-lab.

Figure 1. Thallium lab chemical counter with fume hood to draw air away from the lab to protect research from inhaling air with hazardous elements

A fume hood of an average velocity of 100 ft/min is usually used for highly toxic materials [59]. Since higher speed can interrupt the procedure, resulting in turbulence and

consequently the degradation of safety. The lab is also equipped with the chemical hood for usual product manipulation and a unique hood for a furnace.

Keeping toxic materials in a safe place is another vital consideration. Thallium poisoning can be reported due to poor housekeeping. All the handling, weighing, and mixing are done under the hood (fig.4). In contrast, the experiments are done on an aspiration table (fig.5) to collect any accidental thallium containing electrolyte (preparation method is given in chapter three) or other powders spills.

The materials are always stored in a dry place while tightly closed and labelling the danger signs to avoid unnecessary contact in the lab. Moreover, the thallium waste is dumped into airtight containers promptly.

Toxic thallium absorbed by the skin if it comes in contact with skin, so highly protective and waterproof tyvex® suits and facial masks with absolute filters are always worn while working and handling the materials. Moreover, high protective disposable gloves are essential to avoid the bare hand handling of things while working with thallium since hand contamination can cause ingestion unknowingly.

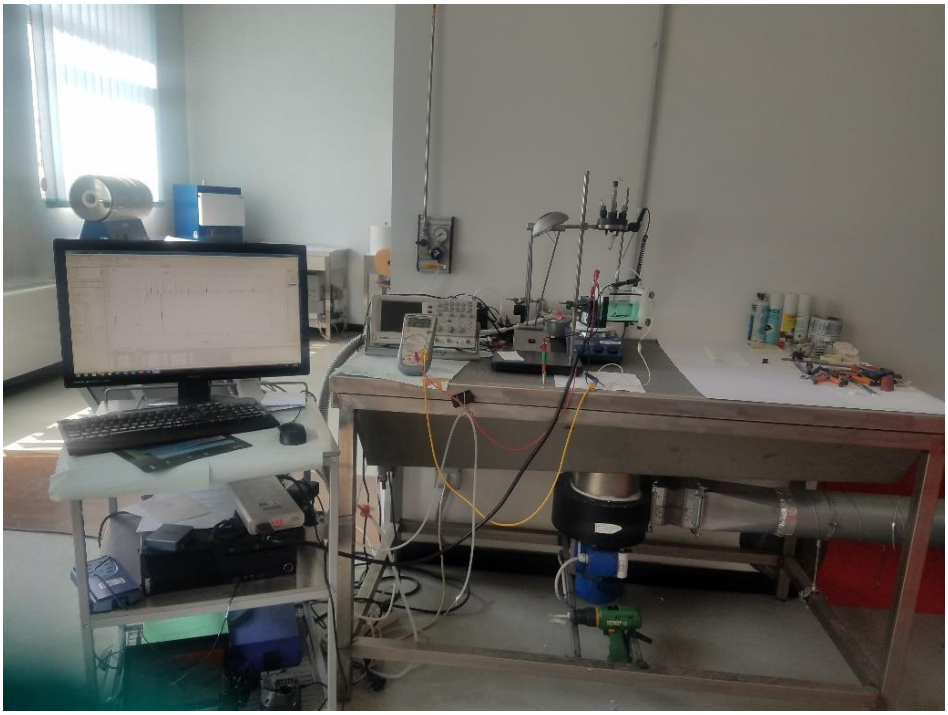

Figure 2. A 3-electrode cell is attached to the potentionstate and placed over the aspiration table

Figure 3. Furnace Hood directly hanging over three-zone furnace to collect vapours while thallium superconductors are under annealing process

This safety equipment is enough to prevent Tl pollution in routine work and protect the operator from accidents. However, the wearing of a is foreseen. In addition, the working procedure requires that, in case of hazardous manipulation, like furnace tube cleaning or vacuum cleaning system filter changing, the use of a facial mask with absolute filter.

Moreover, to prepare the superconductors, the lab is also equipped, technical gases lines, a Three-zone tubular furnace (Pure O_2) up 1200°C, a single-zone tubular furnace (controlled atmosphere or high vacuum) up 1200°C, Muffle furnace, Precision balance, Chemical glassware, Ph-meter, Oscilloscope and Glass dryer. Moreover, electrochemical cells, stirrer and heating plate deposit the precursors of thallium based superconducting thallium based thin film precursors.

Another adjacent room to the thallium lab was fully furnished with lab equipment to work in a non-toxic environment.

.

Figure 4. Adjacent lab to thallium lab to prepare and treat non-toxic material